INTERNATIONAL DOCTORAL SCHOOL OF THE USC

Jessica
Fraga Codesido

PhD Thesis

NEW THERAGNOSIS APPROACHES IN INFLAMMATORY DISEASES USING [89ZR]ZR-ANTI-TNF-a PET IMAGING

Santiago de Compostela, 2025

Doctoral Programme in Drug Research and Development

ESCOLA DE DOUTORAMENTO
INTERNACIONAL DA USC

DOCTORAL THESIS

NEW THERAGNOSIS APPROACHES IN INFLAMMATORY DISEASES USING [^{89}ZR]ZR-ANTI-TNF-α PET IMAGING

Author

Jessica Fraga Codesido

Supervisors: Pablo Aguiar Fernández

Anxo Fernández Ferreiro

Francisco Javier Otero Espinar

Tutor: Francisco Javier Otero Espinar

DOCTORAL PROGRAMME IN DRUG RESEARCH AND DEVELOPMENT

SANTIAGO DE COMPOSTELA - 2025

AGRADECEMENTOS

En primeiro lugar, quero agradecer ós meus directores de tese, ó Dr. Pablo Aguiar, o Dr. Anxo Fernández e o Dr. Francisco Otero, por darme a oportunidade de traballar ó seu lado e aprender deles ó longo destos anos. Pola súa confianza no meu traballo, a súa axuda constante, o seu apoio e bos consellos. Dr. Pablo Aguiar gracias tamén por axudarme a superar os meus límites e a afrontar novos retos, e por todos os bos momentos que vivín durante a tese, que foron a gran maioría. Demostras unha dedicación e entusiasmo pola investigación dun xeito que anima ó traballo ben feito e que proporciona unha gran satisfacción.

En segundo lugar, mención especial á Dra. Lara García e ó Dr. Xurxo García, pilares sobre os que sosterme estos anos. Lara, gracias pola acollida, por ensinarme dende o primeiro momento, por todas as horas no CEBEGA e pola paciencia infinita. Xurxo, gracias pola túa capacidade de escoita activa, polo teu trato cercano, pola túa dispoñibilidade constante. Considérome afortunada de formar parte do equipo tan excepcional que estades creando.

Tamén me gustaría agradecer a todas as persoas coas que me crucei durante a tese. O doctorado permitiume coñecer a persoas marabillosas e sen elas esta etapa non tería o mesmo significado. Quero agradecer especialmente ás miñas compañeiras do laboratorio de Imaxen Molecular, o seu apoio, a súa axuda e todos os momentos compartidos que fixeron que o doctorado fose unha das mellores experiencias que vivín. Agradecer a Alejandro Sánchez Crespo que con 6 meses, unha pizarra e moitas horas me transmitiu a súa paixón no traballo ben feito e seguridade en min mesma. E tamén gracias ós compañeiros dos outros laboratorios e persoal do CIMUS, quenes cun sorriso sempre estiveron dispoñibles para todo o que precisei.

Por último, pero non menos importante, quero agradecer á miña familia, en particular ós meus pais, MªCarmen e Serafín, polo seu amor incondicional e apoio constante ó longo de toda a vida; ós meus abuelos, Amelia e Maximino por inculcarnos a perseverancia polos nosos desexos e ós meus irmáns, Vanessa e Jose, quenes me acompañan sempre da man tendo confianza cega en min. Tamén quero agradecer ás miñas amigas por escoitarme sempre, axudarme en todo o que poden, e desconectar conmigo. Mención especial a Cris: amiga, investigadora e mentora na sombra, gracias pola túa axuda e por darme impulso nos momentos de baixón. Son moi afortunada de poder contar coas miñas amigas en cada etapa da vida e por seguir facéndonos maiores xuntas. E a Javi, gracias polo teu amor e cariño, por soportarme cando nin eu me soporto e sobretodo para recordarme a importancia de parar para poder desfrutar do camiño.

Gracias.

"Gracias especialmente a min, por ser tan traballadora, tan valiente, porque estiven a punto de tirar a toalla, e por ser tan maja, gracias." Ursula Corberó.

INDEX

LIST OF PUBLICATIONS

The results presented in **Chapter I** have already been published as:

Tittle: PET biodistribution study of subcutaneous and intravenous administration of adalimumab in an inflammatory bowel disease model.

Authors and affiliations: Jessica Codesido [a b l], Lara García-Varela [a c l], Xurxo García-Otero [a c d l], Sheila Bouzón-Barreiro [a], Noemí Gómez-Lado [a c], Francisco José Toja-Camba [b f], Cristina Mondelo-García [b f], Héctor Lazaré [e], Julia Baguña Torres [g], Jana Vidal-Otero [h], Santiago Medin-Aguerre [i], Alejandro Sanchez-Crespo [j], Francisco J. Otero-Espinar [d k l], José R. Herance [g], Anxo Fernández-Ferreiro [b f], Pablo Aguiar [a c].

[a] Molecular Imaging and Pharmacokinetic Modelling Group, CIMUS, University of Santiago de Compostela, Santiago de Compostela, Spain

[b] FarmaCHUSLab Group, University Clinical Hospital, Health Research Institute of Santiago de Compostela (IDIS), Santiago de Compostela, Spain

[c] Nuclear Medicine and Molecular Imaging Group, University Clinical Hospital, Health Research Institute of Santiago de Compostela (IDIS), Santiago de Compostela, Spain

[d] Pharmacology, Pharmacy and Pharmaceutical Technology Department, Faculty of Pharmacy, University of Santiago de Compostela, Santiago de Compostela, Spain

[e] Department of Pathology, University Clinical Hospital, Santiago de Compostela, Spain

[f] Pharmacy Department, University Clinical Hospital, Santiago de Compostela (SERGAS), Spain

[g] Medical Molecular Imaging Research Group and Nuclear Medicine Department, Vall d'Hebron University Hospital, Vall d'Hebron Research Institute (VHIR), Autonomous University Barcelona, CIBER-BBN, Barcelona, Spain

[h] Pharmacy Department, Vall d'Hebron University Hospital, E-08035 Barcelona, Spain

[i] Galician PET Radiopharmacy Unit, GALARIA, University Clinical Hospital, Santiago de Compostela 15706, Spain

[j] Department of Medical Radiation Physics and Nuclear Medicine, Karolinska University Hospital, Stockholm, Sweden

[k] Institute of Materials (iMATUS), University of Santiago de Compostela, Santiago de Compostela, Spain

[l] Paraquasil group, Health Research Institute of Santiago de Compostela (IDIS), Santiago de Compostela, Spain

Journal: International journal of pharmaceutics. 2025, 669, 125011. A first quartile journal, ranked 16t/171 in the category of *Pharmacology, Toxicology and Pharmaceutics – Pharmaceutical Science*, with an impact factor of 5.3. (DOI: https://doi.org/10.1016/j.ijpharm.2024.125011). PMID: 39617190. Editorial: Elsevier. ISNN: 0378-5173.

Author contribution: conceptualisation, research, methodology, data extraction, data analysis, validation, visualisation, writing, and editing (including the first draft and subsequent revisions).

LIST OF ABBREVIATIONS

[^{18}F]FDG: 2-deoxy-2-[^{18}F]fluoro-D-glucose / [^{18}F]-fluorodeoxyglucose
2D: two-dimensional
3D: three-dimensional
ARN: ribonucleic acid
AUC: area under the curve
BRB: blood-retinal barrier
BsAbs: Bispecific antibodies
CAR-T: Chimeric antigen receptor-T
CD: Crohn's disease
cDNA: complementary deoxyribonucleic acid
CT: Computed tomography
DFO: deferoxamine
DSS: dextran sulfate sodium
EDTA: ethylenediaminetetraacetic acid
ELISA: enzyme-linked immunosorbent assay
EMM: estimated marginal mean
EU: European Union
F-18: fluor-18
FDA: Food and Drug Administration
GC: Glucorticoids
GEE: generalized estimating equations
H&E: hematoxylin and eosin
HSCT: Hematopoietic stem cell transplantation
IBD: inflammatory bowel disease
ID: injected dose
IFN-γ: gamma interferon
IL: Interleukin
IMIDs: Immune-mediated inflammatory diseases
IV: intravenous
IVT: intravitreal
LPS: Lipopolysaccharide
mAb: monoclonal antibody
MHC: major histocompatibility complex

MIP image: maximum intensity projection image

MIP: macrophage inflammatory protein

MLEM : Maximum Likelihood Expectation Maximization

MRT: Mean residence time

Na_2CO_3: sodium carbonate

NK: natural killer

NSAIDs: Non-Steroidal Anti-Inflammatory Drugs

P.I. : post-injection

PBS: phosphate-buffered saline

PET: Positron Emission Tomography

PVE: partial volume effect

qPCR: quantitative real-time polymerase chain reaction

RA: rheumatoid arthritis

radio-iTLC: radio-instant thin layer chromatography

RCP: radiochemical purity

RMSE: lower root mean squared error

SC: subcutaneous

SD: standard deviation

siRNAs: Small interfering RNAs

SPECT: Single-Photon Emission Computed Tomography

SUV: Standardized uptake value

TACE: TNFα-converting enzyme

TCRs: antigen receptors

TFP-N-sucDf-Fe: tetrafluorophenyl-N-succinyldeferoxamine-B-Fe^{3+}

TNF-α: tumor necrosis factor-alpha

TNFR: tumor necrosis factor receptor

UC: ulcerative colitis

VH: heavy chain

VHH: heavy chain variable domain

VL: light chain

Zr-89: zirconium-89

SUMMARY

Immune-Mediated Inflammatory Diseases (IMID) constitute a diverse group of chronic conditions characterised by abnormal activation of the immune system, leading to persistent inflammation, tissue damage, and progressive functional impairment. Some of the IMIDs are inflammatory bowel disease (IBD), non-infectious uveitis, and rheumatoid arthritis (RA), all of which have a significant clinical, social, and economic burden. These diseases share common pathophysiological mechanisms, such as the overexpression of pro-inflammatory cytokines, dysfunction of effector immune cells, and loss of immune tolerance, which have prompted the development of targeted therapies against specific molecular targets. One of the most successful therapeutic strategies in recent decades has been the use of monoclonal antibodies targeting tumor necrosis factor alpha (TNF-α). Drugs such as adalimumab, infliximab, and etanercept have shown efficacy in reducing inflammatory activity and improving clinical symptoms in multiple IMID. However, between 20% and 40% of patients do not respond adequately to these therapies, raising questions about the factors that determine their efficacy and bioavailability in target tissues.

In this context, the present doctoral thesis aims to develop and validate a new methodology based on Positron Emission Tomography (PET) imaging to characterize the *in vivo* biodistribution and pharmacokinetics of anti-TNF-α therapies in murine models of IBD, uveitis, and RA. For this purpose, a self-developed radiopharmaceutical, [^{89}Zr]Zr-DFO-adalimumab, was employed, allowing real-time, non-invasive visualisation and quantification of antibody distribution.

The experimental design of the thesis is structured around the implementation of a unified methodological protocol based on anatomical imaging by computed tomography (CT) and molecular imaging by positron emission tomography (PET/CT) with [^{89}Zr]Zr-DFO-adalimumab. This approach was applied to three well-established animal models of inflammatory diseases: DSS-induced colitis, endotoxin-induced uveitis (EIU), and K/BxN serum-induced arthritis. In addition, complementary techniques such as qPCR, immunohistochemistry, histological analyses, and enzyme-linked immunosorbent assays (ELISA) were employed to validate the imaging findings and confirm the presence of TNF-α in the target tissues. The methodology used enables correlations to be established between radiopharmaceutical uptake, molecular target expression, and histological changes associated with inflammation. Furthermore, in both the IBD and uveitis models, different routes of administration (subcutaneous, intravenous, and intravitreal) of [^{89}Zr]Zr-DFO-adalimumab were evaluated.

First, in the IBD model, intravenous administration of [^{89}Zr]Zr-DFO-adalimumab resulted in earlier and more pronounced colon uptake compared to subcutaneous administration. Animals with IBD showed a faster systemic clearance of the radiotracer, suggesting preferential redistribution towards inflamed tissues. These results indicate that the intestinal inflammatory state significantly alters the antibody pharmacokinetics, and the administration route influences tissue uptake kinetics. Correlation with weight loss, [^{18}F]FDG uptake, and histology supports the validity of the model and the relevance of the findings.

Second, in the uveitis model, subcutaneous and intravitreal routes of [^{89}Zr]Zr-DFO-adalimumab were compared to assess the ocular bioavailability of the antibody. The results showed that subcutaneous administration failed to achieve therapeutic concentrations in the inflamed eyes, whereas intravitreal injection allowed prolonged and localised retention of the radiotracer. The expression of pro-inflammatory cytokines in ocular tissue and plasma antibody

levels suggest that systemic inflammation may divert the drug towards other organs, limiting its ocular availability. These findings could have important clinical implications, supporting the potential use of local delivery strategies in patients with refractory uveitis to systemic therapy.

Third, in the RA model, joint biodistribution of anti-TNF-α was characterized by PET/CT, revealing a progressive and specific accumulation in the inflamed joints, particularly the ankles. Uptake was both rapid and sustained, correlating with increased joint diameter, [^{18}F]FDG uptake, and TNF-α expression at the tissue and serum levels. Histological analysis confirmed the presence of leucocyte infiltration and structural damage to the cartilage, validating the model as a robust preclinical tool for studying TNF-α-targeted therapies.

In summary, the findings from the three animal models enable the identification of common patterns and relevant differences in the biodistribution of anti-TNF-α. One of the most consistent findings was the reduction of radiotracer blood levels in animal models with active disease compared to healthy controls. This observation suggests that the antibody preferentially redistributes to inflamed tissues, where it binds to its molecular target, thereby reducing its systemic availability. This phenomenon was particularly evident in the IBD and uveitis models, where systemic inflammation induced by DSS or LPS respectively, led to more intense tissue uptake and faster drug clearance. Another key aspect addressed in the thesis is the impact of the administration route on the pharmacokinetics and biodistribution of the antibody. In IBD, SC administration, although the most common in clinical practice due to its ease of use and lower invasiveness, showed significant limitations in terms of slower distribution compared with IV administration. In the case of uveitis, IVT administration was able to achieve sustained therapeutic concentrations in the inflamed eyes, something that did not occur with subcutaneous administration, highlighting the need to adapt the route of administration to the specific clinical context.

In conclusion, this thesis establishes a novel PET-based methodology to quantitatively characterise the *in vivo* biodistribution and pharmacokinetics of anti-TNF-α therapies in murine models of IMID. Our dynamic, non-invasive, and quantitative approach provides a powerful translational tool to optimise therapeutic strategies based on anti-TNF-α drugs and personalise treatment schemes, representing a significant advantage over traditional methods based on *ex vivo* analysis, reducing inter-individual variability and enhancing the statistical power of experiments. The implementation of an innovative PET imaging strategy with [^{89}Zr]Zr-DFO-adalimumab in three animal models of inflammation represents a relevant advance towards clinical application, opening new possibilities for both diagnosis and individualised therapeutic monitoring in inflammatory pathologies (theragnosis). The evidence that active inflammation modifies the pharmacokinetics of anti-TNF-α suggests that dosing regimens could benefit from greater personalisation, based on biomarkers of inflammatory activity and imaging tools capable of predicting therapeutic response. In this regard, PET-based methodology could play a key role in precision medicine.

RESUMO

As enfermidades inflamatorias inmunomediadas (IMID, polas súas siglas en inglés) constitúen un grupo amplo e heteroxéneo de patoloxías crónicas caracterizadas por unha activación anómala, persistente e desregulada do sistema inmunolóxico. Esta activación da lugar a procesos inflamatorios sostidos no tempo que non só provocan dano tisular progresivo, senón tamén un deterioro funcional acumulativo, con manifestacións clínicas variables segundo o órgano ou sistema afectado, que impactan de maneira significativa na calidade de vida das persoas afectadas. Ademais do impacto directo sobre os pacientes, as IMID supoñen unha elevada carga social, económica e asistencial, derivada do seu carácter crónico, da frecuente presenza de comorbilidades, da necesidade de tratamentos prolongados e, en moitos casos, dun seguimento clínico continuo e dun consumo sostido de recursos sanitarios. En conxunto, estas características converten ás enfermidades inflamatorias inmunomediadas nun importante reto sanitario, tanto desde o punto de vista clínico como socioeconómico.

Algunhas das enfermidades inflamatorias inmunomediadas son a enfermidade inflamatoria intestinal (EII), a uveíte non infecciosa e a artrite reumatoide (AR). A EII inclúe entidades como a enfermidade de Crohn e a colite ulcerosa que afectan principalmente a o tracto gastrointestinal caracterizándose por episodios recorrentes de inflamación intestinal que cursan con dor abdominal, diarrea, perda de peso e complicacións extraintestinais. A uveíte non infecciosa, pola súa banda, constitúe unha enfermidade inflamatoria ocular potencialmente grave, na que a inflamación da úvea e doutras estruturas oculares pode conducir, en ausencia dun tratamento axeitado, a dano estrutural irreversible e perda progresiva da visión. Pola súa banda, a AR é unha enfermidade autoinmune sistémica que afecta fundamentalmente ás articulacións, provocando dor, inflamación crónica, destrución da cartilaxe e do óso, así como unha perda funcional acumulativa que pode derivar en discapacidade e nun importante impacto na calidade de vida dos pacientes.

A pesar da diversidade clínica e anatómica destas patoloxías, todas elas comparten mecanismos fisiopatolóxicos comúns. Entre estes destacan a sobreexpresión de citocinas proinflamatorias, a activación aberrante de células inmunes efectoras, a alteración das vías de sinalización inflamatoria e a perda dos mecanismos de tolerancia inmunolóxica. Dentro deste contexto, o factor de necrose tumoral alfa (TNF-α, polas súas siglas en inglés) emerxe como unha citocina clave na cascada inflamatoria, exercendo un papel central na activación e mantemento da resposta inflamatoria en múltiples enfermidades inflamatorias inmunomediadas, entre elas a enfemidade inflamatoria intestinal, a uveiti non infecciosa e a artrite reumatoide.

O coñecemento destes mecanismos moleculares e celulares foi determinante para o desenvolvemento de terapias biolóxicas dirixidas contra dianas específicas do sistema inmunitario. Entre elas, os anticorpos monoclonais anti-TNF-α, como adalimumab, infliximab e etanercept, os cales supuxeron un avance terapéutico. Estes fármacos non so demostraron unha elevada eficacia na redución da actividade inflamatoria, senon tamén na mellora dos síntomas clínicos e na prevención do dano estrutural en diversas enfermidades inflamatorias inmunomediadas. Non obstante, a resposta terapéutica non é uniforme: estímase que entre un 20 % e un 40 % dos pacientes non responden de maneira axeitada ao tratamento con anti-TNF-α ou perden resposta ao longo do tempo debido á xeración de anticorpos en contra destos fármacos que os destruen antes de que poidan facer efecto. Esta variabilidade clínica pon de

manifesto a necesidade de comprender en profundidade os factores que condicionan a biodistribución, a farmacocinética e o acceso destes anticorpos aos tecidos diana.

Con este contexto, esta tese fundaméntase nunha hipótese xeral que postula que a terapia con anti-TNF-α pode caracterizarse de forma precisa estudando a súa biodistribución e farmacocinética a través da imaxe tomográfica de emisión de positróns (PET, polas súas siglas en inglés) con [^{89}Zr]Zr-DFO-adalimumab. Máis especificamente, propóñense tres hipóteses derivadas: primeiro, que a vía de administración (subcutánea fronte a intravenosa ou intravítrea) inflúe significativamente na distribución sistémica e tisular do anticorpo; segundo, que a localización da doenza (sistémica vs. órgano-específica) modula dita biodistribución, cunha maior acumulación agardada nos focos de actividade inflamatoria; e terceiro, que os niveis elevados de TNF-α actúan como un factor determinante na magnitude da retención do fármaco nos tecidos inflamados, condicionando o seu perfil farmacocinético global.

A presente tese de doutoramento ten como obxectivo principal caracterizar de maneira cuantitativa, dinámica e non invasiva a biodistribución e farmacocinética *in vivo* do anticorpo biolóxico radiomárcado anti-TNF-α en diferentes modelos murinos representativos de enfermidades inflamatorias inmunomediadas. Este obxectivo principal desagrégase en fitos específicos estruturados por capítulos: no Capítulo 1, avaliar o impacto da vía de administración e a inflamación intestinal; no Capítulo 2, analizar a capacidade do trazador para alcanzar o tecido ocular no modelo de uveíte comparando a vía sistémica coa intravítrea; e no Capítulo 3, investigar a captación articular a o longo do tempo nun modelo de artrite e a súa correlación coa expresión proteica da diana molecular (TNF-α). Para acadar este obxectivo, desenvolveuse e validouse unha metodoloxía baseada na imaxe molecular mediante tomografía por emisión de positróns (PET), combinada ca imaxen anatómica por tomografía computarizada (CT), as cales permiten a cuantificación e localización do fármaco ó longo de todo o corpo.

Deseñouse e produciuse o radiofármaco específico [^{89}Zr]Zr-DFO-adalimumab, mediante a conxugación do anticorpo monoclonal adalimumab (Imraldi 40 mg, Biogen S.L, Madrid, Spain) cun axente quelante (deferoxamina, DFO) e o seu posterior marcado co radioisótopo circonio-89. Este radioisótopo presenta unha vida media adecuada para o seguimento de anticorpos monoclonais, permitindo estudos de imaxe lonxitudinal durante varios días. Os protocolos de conxugación e radiomarcaxe do [^{89}Zr]Zr-DFO-adalimumab, elemento central desta tese, foron optimizados e avaliados mediante diferentes controis de calidade despois de cada modificación. Asi puido garantirse non so a integridade estrutural despois da conxugación a través do radio-HPLC, senon a conservación da afinidade do anticorpo pola súa diana molecular a través da técnica ELISA, e tamén a estabilidade en soro e unha elevada pureza radioquímica medida a través do radio-iTLC. Ademais, ao longo da tese empregouse [^{18}F]FDG como trazador metabólico de referencia, administrado por vía intravenosa tras a posta dos individuos en xaxún. As adquisicións de imaxe realizáronse cun sistema preclínico Albira PET/CT (Bruker), optimizado para modelos animais pequenos, que combina alta sensibilidade e resolución espacial en PET cunha caracterización anatómica detallada mediante CT.

O deseño experimental da tese baséase nun enfoque comparativo e transversal, aplicando unha metodoloxía homoxénea en tres modelos animais ben establecidos de enfermidades inflamatorias: a enfermidade inflamatoria intestinal inducida con sulfato de dextrano sódico (DSS) a través da vía oral, a uveíte inducida con endotoxina bacteriana (EIU) tras a administración intravitrea, e a AR inducida con soro K/BxN inxectado intraperitonal. En cada un destes modelos realizáronse estudos de imaxe PET/CT de maneira lonxitudinal, avaliáronse

distintas vías de administración do radiofármaco (subcutánea, intravítrea e intravenosa) e complementáronse os achados por imaxe con técnicas de bioloxía molecular como a inmunohistoquímica, a histopatoloxía e ensaios ELISA. Polo que a metodoloxía empregada permite establecer correlacións entre a captación do radiofármaco, a expresión molecular de TNF- α e os cambios histolóxicos asociados á inflamación.

No modelo de enfermidade inflamatoria intestinal inducida por DSS, comparouse a vía de administración subcutánea e a intravenosa. Os estudos de imaxe revelaron diferenzas significativas na cinética de distribución do [^{89}Zr]Zr-DFO-adalimumab en función da vía de administración. A administración intravenosa resultou nunha captación máis rápida e pronunciada no colon inflamado en comparación coa vía subcutánea. Ademais, os animais con EII mostraron unha eliminación sistémica máis rápida do radiotrazador, o que suxire unha redistribución preferente cara aos tecidos inflamados. Estes achados indican que o estado inflamatorio intestinal altera de maneira significativa a farmacocinética do anticorpo, afectando tanto a súa distribución como a súa dispoñibilidade sistémica. A validez destes resultados foi confirmada mediante a correlación de parámetros como a perda de peso, así como con marcadores de inflamación metabólica obtidos mediante PET con [^{18}F]FDG e análises inmunohistoquímicos e histolóxicas do tecido colónico. Ata o de agora este enfoque fora escasamente explorado en modelos preclínicos de enfermidades inflamatorias. No contexto da EII, só se identificou un estudo previo que utilizou imaxe PET para avaliar a biodistribución intravenosa do infliximab. Aínda que o estudo demostrou unha maior acumulación do radiofármaco no colon inflamado, non investigou a evolución temporal do sinal e limitouse a unha análise ate as 72 horas. Así mesmo, un estudo clínico que empregou infliximab marcado con Tecnecio-99m mediante imaxe SPECT pero este enfrontouse a limitacións derivadas da curta vida media do radioisótopo (6 horas), o que impediu a detección de acumulacións tardías nos tecidos inflamados. En contraste, o noso estudo estendeu o período de observación ata os 7 días tras a inxección utilizando un enfoque baseado en PET que permitiu unha avaliación moito máis sensible e prolongada da distribución do radiofármaco [^{89}Zr]Zr-DFO-adalimumab.

No modelo de uveíte inducida por endotoxina bacteriana, avaliáronse as vías de administración subcutánea e intravítrea e explorouse o impacto da vía de administración na biodispoñibilidade ocular do anticorpo. Os resultados demostraron que a administración subcutánea non permitiu alcanzar concentracións terapéuticas no ollo inflamado. Pola contra, a administración intravítrea do [^{89}Zr]Zr-DFO-adalimumab permitiu unha retención prolongada e localizada do radiotrazador no globo ocular. A análise da expresión de citocinas proinflamatorias no tecido ocular, xunto cos niveis plasmáticos do anticorpo, suxire que a inflamación sistémica pode desviar o fármaco cara outros órganos, limitando a súa dispoñibilidade ocular cando se administra por vía subcutanea. Estes resultados teñen importantes implicacións clínicas, xa que apoian o desenvolvemento e a utilización de estratexias de administración local en pacientes que non responden ao tratamento sistémico. No caso específico da uveíte, aínda que a vía de administración subcutánea segue a ser o estándar para o adalimumab, informes preliminares exploraron a inxección intravítrea con resultados terapéuticos prometedores. Estes achados reforzan a importancia de comprender a distribución do fármaco en relación coa localización anatómica da inflamación.

No modelo de AR inducida por inxección do soro K/BxN, a imaxe PET/CT permitiu caracterizar a distribución articular do adalimumab tras ser inxectado a través da vía intravenosa. Observouse unha acumulación progresiva e específica do radiotrazador nas articulacións inflamadas, especialmente nos nocellos, que son unha das localizacións máis

afectadas neste modelo. A captación foi rápida e sostida ao longo do tempo, e correlacionouse de maneira significativa co aumento do diámetro articular, coa captación de [^{18}F]FDG e cos niveis de expresión de TNF-α tanto no tecido articular como no soro. A análise histolóxica confirmou a presenza de infiltrado leucocitario e dano estrutural da cartilaxe, validando este modelo como unha ferramenta preclínica robusta para o estudo de terapias dirixidas contra a citocina TNF-α. Aínda que non existen estudos previos que analicen directamente esta aproximación, diversas estratexias baseadas en PET foron aplicadas previamente a este modelo de artrite. Previamente, un grupo de investigadores liderado por Puuvuori et al, usou un radiofármaco dirixido contra CD69, un marcador temperá de activación inmune, permitindo detectar actividade inflamatoria antes da aparición dos síntomas clínicos. Por outra banda, o equipo liderado por Gawne et al. tamén analizou a biodistribución de glucocorticoides liposomais marcados con cirnconio-89 en articulacións inflamadas, facilitando a predición da eficacia terapéutica, pero cun sinal non específico. Ademais, Bezière et al. introduciron un trazador GPVI-Fc marcado con cobre-64 que permite visualizar fibrose activa e procesos de remodelación tisular na artrite crónica, ampliando as posibilidades para o estudo da inflamación persistente.

A análise conxunta dos resultados obtidos nos tres modelos animais permitiu identificar tanto patróns comúns como diferenzas relevantes na biodistribución do adalimumab en distintos contextos inflamatorios. Un dos achados máis consistentes foi a diminución dos niveis sanguíneos do radiotrazador nos animais con enfermidade activa en comparación cos controis sans, o que suxire unha redistribución preferencial do anticorpo cara os tecidos inflamados, onde se une a súa diana molecular, reducindo consecuentemente a súa dispoñibilidade sistémica. Este fenómeno foi particularmente acusado nos modelos de enfermidade inflamatoria intestinal e uveíte, nos que a inflamación sistémica inducida por DSS ou LPS, respectivamente, favoreceu unha captación tisular máis intensa e unha eliminación máis rápida do fármaco da circulación. En contraste, a análise das cinéticas de captación revelou perfís específicos segundo o modelo: unha captación rápida seguida dun descenso tras 48 horas na EII, unha retención ocular prolongada tras a administración local no modelo de uveíte, e unha captación sostida ata as 72 horas no modelo de artrite reumatoide. Conxuntamente, estes resultados poñen de manifesto que o contexto patolóxico e as características do microambiente inflamatorio exercen unha influencia máis determinante sobre a biodistribución do adalimumab que a propia vía de administración, destacando a importancia de considerar a fisiopatoloxía específica de cada enfermidade na interpretación dos estudos de imaxe e na optimización das estratexias terapéuticas.

Outro aspecto clave abordado nesta tese é o impacto da vía de administración na farmacocinética e na biodistribución do adalimumab, factores determinantes para a súa eficacia terapéutica. A administración subcutánea, aínda que amplamente empregada na práctica clínica debido á súa comodidade e menor invasividade, mostrou limitacións relevantes en termos de velocidade de absorción, distribución sistémica e penetración nos tecidos inflamados, o que evitar o alcance de concentracións terapéuticas óptimas. Pola contra, a administración intravenosa permitiu unha distribución máis rápida e homoxénea do anticorpo, cunha captación tisular máis temperá. No modelo de uveíte, a administración intravítrea resultou ser a vía capaz de acadar e manter concentracións terapéuticas sostidas no ollo inflamado, superando as limitacións impostas polas barreiras anatómicas e fisiolóxicas oculares. Estes resultados poñen de manifesto a importancia de adaptar a vía de administración ao contexto clínico específico e á localización da enfermidade, subliñando que unha estratexia terapéutica personalizada pode

resultar clave para optimizar a eficacia dos tratamentos biolóxicos en enfermidades inflamatorias inmunomediadas.

Dende unha perspectiva metodolóxica, esta tese destaca pola aplicación sistemática da imaxe molecular como ferramenta de investigación. A combinación de PET/CT con radiotrazadores específicos, ademais de permitir un estudo cuantitativo, permite unha avaliación dinámica e non invasiva da distribución de fármacos biolóxicos, representando unha vantaxe significativa fronte aos métodos tradicionais baseados na análise *ex vivo*. A posibilidade de realizar estudos lonxitudinais nos mesmos animais reduce a variabilidade interindividual, ademais de incrementar a potencia estatística dos experimentos e diminuir o número de animais necesarios, en consonancia cos principios das 3R na experimentación animal (reemplazo, reducción e refinamento).

Ao longo deste traballo analizáronse máis de 550 estudos de imaxe PET, o que permitiu obter unha caracterización exhaustiva da distribución temporal e espacial do radiofármaco en múltiples órganos e tecidos ao longo da progresión da enfermidade. Os achados derivados da imaxe molecular foron validados mediante un conxunto de técnicas complementarias de bioloxía molecular e análise tisular. En particular, empregouse qPCR para a avaliación da expresión xénica, inmunohistoquímica para a análise da expresión tisular de TNF-α, e ensaios de inmunoabsorción ligado por enzimas (ELISA, polas súas siglas en inglés) para a cuantificación dos niveis séricos desta citocina. Así mesmo, realizouse unha validación histolóxica mediante análise morfolóxica convencional e distintas técnicas de tinción, como a hematoxilina-eosina para a avaliación do dano tisular e o azul de toluidina para o estudo da cantidade de proteoglicanos en mostras óseas. Este enfoque multidisciplinar reforza de maneira significativa a robustez e fiabilidade dos resultados obtidos, permitindo establecer correlacións sólidas entre a captación do radiotrazador, a expresión da diana molecular e os cambios histopatolóxicos asociados aos procesos inflamatorios.

Este traballo representa unha aplicación sistemáticas do [^{89}Zr]Zr-DFO-adalimumab en modelos murinos de IMID. A validación do seu comportamento *in vivo* en tres modelos inflamatorios distintos establece unha base sólida para a súa posible aplicación futura en estudos clínicos, tanto con fins diagnósticos como de monitorización terapéutica, no marco da teragnose. A capacidade de visualizar e cuantificar a distribución dun fármaco biolóxico en tempo real abre novas posibilidades para a selección de pacientes, a optimización de doses e a avaliación temperá da resposta terapéutica.

Dende unha perspectiva traslacional, os resultados desta tese teñen implicacións relevantes para a práctica clínica e para o desenvolvemento de novas estratexias terapéuticas. A evidencia de que a inflamación activa modifica a farmacocinética dos anti-TNF-α suxire que os réximes de dosificación poderían beneficiarse dunha maior personalización, baseada en biomarcadores de actividade inflamatoria e en ferramentas de imaxe que permitan predicir a resposta ao tratamento. Neste sentido, a imaxe molecular podería desempeñar un papel clave na medicina de precisión, facilitando a individualización dos tratamentos e mellorando os resultados clínicos. Ademais, a caracterización detallada da biodistribución do anticorpo en distintos contextos patolóxicos proporciona información útil para o deseño de novas formulacións e vías de administración. No caso da uveíte, os resultados apoian o desenvolvemento de sistemas de liberación local que permitan acadar concentracións terapéuticas no ollo sen comprometer a seguridade sistémica. No caso da EII, a evidencia dunha captación colónica máis eficiente tras

a administración intravenosa podería xustificar o uso desta vía en pacientes con inflamación activa e resposta subóptima á administración subcutánea.

Finalmente, esta tese abre novas liñas de investigación que poderían ser abordadas en estudos futuros co obxectivo de ampliar e consolidar os achados presentados. Entre elas destaca a avaliación da biodistribución doutros anticorpos monoclonais dirixidos contra diferentes dianas inflamatorias, o que permitiría comparar perfís farmacocinéticos e patróns de captación tisular en función do mecanismo de acción de cada fármaco. Así mesmo, a comparación entre distintos radioisótopos empregados en imaxe PET podería contribuír a optimizar a sensibilidade, resolución temporal e adecuación dos trazadores ás diferentes escalas temporais dos procesos inflamatorios. A aplicación destas metodoloxías en modelos animais máis complexos, así como a súa traslación a estudos clínicos piloto permitiría avanzar cara a unha validación translacional do enfoque proposto. Ademais, sería de especial interese explorar a relación entre a biodistribución dos fármacos e a expresión de receptores Fc en distintos tecidos, así como analizar o impacto de factores xenéticos e epixenéticos na resposta terapéutica.

En conclusión, esta tese de doutoramento supón unha contribución significativa a o campo da imaxe molecular aplicada ás enfermidades inflamatorias inmunomediadas. Os resultados obtidos non só teñen un elevado valor científico, senón que tamén establecen as bases para a optimización de estratexias terapéuticas personalizadas, co obxectivo último de mellorar a eficacia dos tratamentos, reducir os efectos adversos e incrementar a calidade de vida dos pacientes afectados por estas enfermidades. Neste sentido, a metodoloxía basada en PET podería desempeñar un papel clave na medicina de precisión.

1. INTRODUCTION

1.1 IMMUNE-MEDIATED INFLAMMATORY DISEASES

Immune-mediated inflammatory diseases are a collection of disorders characterized by an exaggerated and dysregulated immune response that causes chronic inflammation and tissue damage. These debilitating ailments significantly compromise the quality of life and cause substantial morbidity (1).

1.1.1 Inflammatory bowel diseases

IBD are chronic inflammatory disorders mainly affecting the gut. Common clinical symptoms include abdominal pain, chronic diarrhoea (sometimes bloody), rectal bleeding, weight loss, fatigue, and fever (2). It has an incidence of 16.2 cases per 100,000 inhabitant-years (3). The two main forms of IBD are Crohn's disease (CD) and ulcerative colitis (UC) that differ in several aspects, e.g. regarding the location and distribution of inflammation and in the mucosal cell populations involved in the immune reaction. CD is a segmental, transmural disorder that can affect the whole gastrointestinal tract and type 1 T helper cells have been associated with being involved in pathogenesis. In contrast, UC is characterized by continuous inflammation of the colon. Mucosal CD4+ T cells as key mediators in driving immune responses are critically involved in the pathogenesis of IBD and in accordance, a high number of infiltrating T lymphocytes can be found in both CD and UC in the gut.

The proinflammatory cytokine TNF-α is one of the major pathogenic cytokines involved in the pathogenesis of IBD as elevated levels of TNF-α are present in the serum of both UC and CD patients (4). In addition, an elevated number of TNF-secreting cells in the inflamed mucosa of IBD patients has been repeatedly reported. Herein, lamina propria mononuclear cells isolated from colonic biopsies from IBD patients spontaneously produced increased amounts of TNF-α which correlated with the degree of tissue involvement and mucosal inflammation, strengthening the importance of TNF-α in the inflamed gut. The exact cause of IBD remains indistinct, but it is generally accepted that its etiopathology is multifactorial, involving genetic predisposition, mucosal barrier dysfunction, disturbances in the gastrointestinal microbiota, dysregulated immune responses, environmental, and lifestyle factors (2,5).

The diagnosis of IBD typically involves a combination of endoscopic evaluation, including colonoscopy and biopsy, to assess intestinal inflammation and disease extent. Imaging techniques such as magnetic resonance imaging (MRI) and computed tomography (CT) are used to evaluate complications and small bowel involvement, particularly in Crohn's disease. Laboratory tests measuring inflammatory markers like C-reactive protein and erythrocyte sedimentation rate, along with fecal biomarkers such as calprotectin, assist in distinguishing IBD from other gastrointestinal disorders and in monitoring disease activity. This multimodal approach ensures accurate diagnosis and effective disease management (2).

1.1.2 No infectious uveitis

No infectious uveitis commonly presents with ocular pain, redness, photophobia, blurred vision, decreased visual acuity, tearing, and a sensation of a foreign body in the eye. The uvea, the middle layer among the three concentric layers of the eye, includes the iris, ciliary body, and choroid. It plays a vital role in supplying diffusible nutrients to the retina's outer layer and maintaining the eye's temperature homeostasis. However, due to its rich blood flow, the uvea is highly prone to inflammatory reactions, which can result in uveitis. Severe inflammation of the eye can cause irreversible damage to the retina and optic nerve (6). No infectious uveitis has an incidence of 20 cases per 100.000 inhabitant-years (7).

TNF-α has been clearly identified as a key factor in uveitis. Its levels are elevated in the eye and serum of patients with certain types of intermediate uveitis, non-infectious posterior uveitis, and panuveitis, while they decrease in patients with controlled disease.

The diagnosis of no infectious uveitis involves a comprehensive ophthalmic examination, including slit-lamp biomicroscopy to assess intraocular inflammation and characteristic signs. Visual acuity and intraocular pressure measurements are routinely performed. Imaging techniques such as optical coherence tomography (OCT) are employed to evaluate retinal and choroidal structures, while fluorescein and indocyanine green angiography help identify vascular abnormalities. Laboratory tests and additional investigations are also conducted to exclude infectious causes and systemic diseases associated with uveitis (6).

1.1.3 Rheumatoid arthritis

RA is an autoimmune disease marked by inflammation of the synovial joints caused by autoimmune dysfunction. It has an incidence of 8.3 cases per 100.000 inhabitants-years (8). It is characterised clinically by joint pain, swelling, and symmetrical joint inflammation. Patients commonly experience prolonged morning stiffness lasting more than one hour, fatigue, and general malaise. Over time, RA leads to progressive functional impairment and joint deformities, predominantly affecting the small joints of the hands and feet, although larger joints can also be involved.The induction and progress of RA require the participation of numerous factors such as osteoclasts, synovial fibroblasts, T cells, B cells, natural killer (NK) cells, as well as soluble mediators like IL-1, IL-6, IL-17, and TNF-α. The intricate interaction among these factors leads to pathological changes such as synovial hyperplasia, bone damage, and inflammation affecting multiple joints (9).

The diagnosis of RA is based on a combination of clinical evaluation and laboratory tests, following criteria established by the American College of Rheumatology (ACR) and the European League Against Rheumatism (EULAR) (10). Clinical assessment focuses on joint pain, swelling, symmetrical inflammation, and morning stiffness duration. Laboratory tests include rheumatoid factor, anti-cyclic citrullinated peptide antibodies, and inflammatory markers such as C-reactive protein and erythrocyte sedimentation rate. Imaging techniques, including X-rays, ultrasound, and magnetic resonance imaging (MRI), are used to detect joint erosions, inflammation, and early structural damage, aiding in accurate diagnosis and disease monitoring (9).

1.1.4 Epidemiology

IMIDs have been shown to affect 3–5% of the world population and become one of the most important public health problems (11). The observed socioeconomic, seasonal, and regional disparities among various autoimmune disorders suggest the involvement of environmental factors in disease pathogenesis.

A comprehensive study of a database comprising 22 million individuals in the United Kingdom, a representative developed country, revealed a prevalence rate of 10%, with the incidence of autoimmune diseases showing an upward trend. Furthermore, the interrelations among autoimmune diseases align with shared pathogenetic mechanisms or predisposing factors, particularly within connective tissue diseases and endocrine diseases (12).

The majority of autoimmune disorders are more prevalent in women compared to men. Thyroid disorders, Sjögren's syndrome, lupus, and systemic sclerosis exhibit the highest female-to-male ratios. Conversely, only three autoimmune diseases are more common in men than in women: ankylosing spondylitis, childhood-onset type 1 diabetes, and myasthenia gravis (12).

1.1.5 Etiology

Autoimmune diseases such as inflammatory bowel disease, arthritis and uveitis occur when autoreactive immune cells, especially T cells and B cells are overactivated and recruited to cause self-tissue damage (11).

During autoimmunity[1], autoreactive T cells infiltrate the target tissue and initiate an immune attack:

- **CD8+ cytotoxic T cells** directly interact with and kill the targeted cells.
- **CD4+ helper T cells** can release large amounts of proinflammatory factors, which amplify the immune response. These proinflammatory factors attract myeloid inflammatory cells, including macrophages which release cytokines[2] such as tumor necrosis factor-alpha (TNF-α), which exacerbate inflammation and contribute to tissue damage. On the other hand, **CD4+ helper T cells** provide activation signals to B cells, differentiating into plasma cells that produce large amounts of autoantibodies targeting the body's own antigens.

This cascade leads to sustained inflammation and damage to the targeted tissue.

1.2 TUMOR NECROSIS FACTOR (TNF) AND TUMOR NECROSIS FACTOR RECEPTOR (TNFR)

Tumor necrosis factor (TNF) proteins and their receptors (TNFR) play critical roles in mammalian biology, including cell growth, survival, and apoptosis, immune responses, and organogenesis of the immune, ectodermal, and nervous systems. It has been known that there are more than 35 specific ligand-receptor pairs between TNF and TNFR. Among them, TNFα is a major inflammatory cytokine that exerts antagonist effects on various cell types by activating intracellular signaling through interactions with its receptors. Therefore, TNFα plays

[1] **Autoimmunity:** A state of reactivity of the adaptive immune system to self-antigens, occurring when mechanisms of self-tolerance fail (120).

[2] **Cytokines:** Proteins produced by many different cell types that mediate inflammatory and immune reactions. Cytokines are the main mediators of communication between cells of the immune system.

a crucial role in the pathogenesis of inflammatory autoimmune diseases. TNFα is mainly expressed in activated macrophages and natural killer cells as a 26 kDa transmembrane precursor, which is cleaved by a metalloproteinase, TNFα-converting enzyme (TACE), into a soluble form (Figure 1). Both soluble and transmembrane TNFα bind to type 1 and 2 TNF receptors (TNFR1 and TNFR2). TNFR 1 is located in every tissues and TNFR2 is in immune cells, neurons and endothelial cells. Upon binding, TNFR mediates the signaling processes involved in apoptosis, inflammation, survival and cytokine production (13).

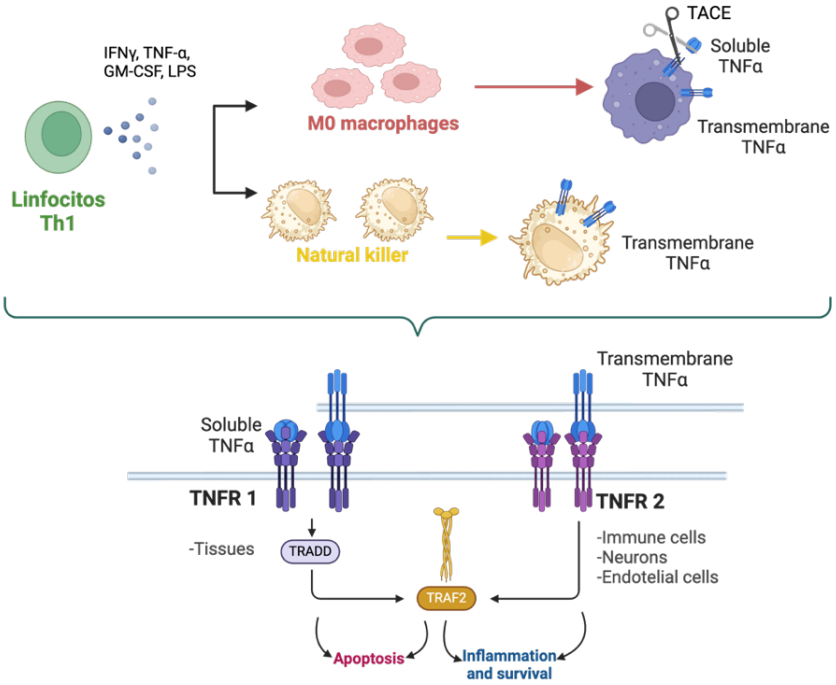

Figure 1: TNF syntesis (above) and TNF activation (below). Created with BioRender.com

Dysregulated signaling from TNF and TNFR proteins is implicated in several immune-mediated inflammatory diseases. Several TNF superfamily ligands and receptors are upregulated in immune cells in the presence of proinflammatory cues. TNF superfamily ligands binding to their respective receptors on target cells initiate intracellular signaling cascades that activate pivotal transcription factors. In normal conditions, signaling from the various TNF/TNFR interactions facilitates immune homeostasis and attenuates autoimmune responses by modulating the intensity and duration of T cell responses. However, constant T cell activation mediated by costimulatory signals, such as TNF-a, promotes their expansion, survival, and differentiation into memory cells (1).

1.3 THERAPEUTIC STRATEGIES

Autoimmune disorders are complex conditions characterized by an aberrant immune response against the body's own tissues, leading to chronic inflammation and tissue damage. Over the years, advancements in understanding the underlying mechanisms of autoimmunity have paved the way for diverse therapeutic strategies. These range from conventional immunosuppressive agents to highly targeted biological therapies, each aimed at modulating the immune system and controlling disease progression.

In the case of IBD, the ECCO therapeutic guidelines recommend initiating treatment with a combination of an immunosuppressant and a glucocorticoid (14). Although in many cases, a top-down strategy with early use of biologics is increasingly employed in patients with severe disease or poor prognostic indicators. A similar approach is outlined in the EULAR guidelines for RA, where initial therapy typically includes immunosuppressants in combination or not with glucocorticoids (15). However not for long time, an early and aggressive intervention within a defined window of opportunity is considered critical to optimise long-term outcomes (14). International recommendations for the treatment of non-infectious uveitis also follow a comparable stepwise strategy; however, in this context, glucocorticoids therapy may be delivered topically depending on the anatomical classification and severity of the disease. It is important to note that the initiation of biological therapies in uveitis is less systematic than in RA or IBD, and is more often reserved for cases where patients are refractory to or dependent on glucocorticoids or conventional immunosuppressants(16,17). This section explores the key therapeutic approaches currently used to manage autoimmune disorders and other therapies that are still being studied.

1.3.1 Non-Steroidal Anti-Inflammatory Drugs (NSAIDs)

NSAIDs are commonly employed for the short- to medium-term management of pain and inflammation. While NSAIDs may provide symptomatic relief in certain autoimmune diseases by mitigating pain and inflammation, their application necessitates careful evaluation due to potential adverse effects and the imperative to address the underlying pathological mechanisms of the disease process. Common examples of NSAIDs include acetylsalicylic acid, diclofenac, ibuprofen, meclofenamate, and celecoxib (18).

1.3.2 Glucocorticoids (GC)

GC have a strong anti-inflammatory and immunosuppressive effect through various actions on immune system cells. They inhibit leukocyte trafficking and their access to the site of inflammation. They interfere with the function of leukocytes, fibroblasts, and endothelial cells, and suppress the production and actions of humoral factors.

They also inhibit the production of various pro-inflammatory cytokines such as tumor necrosis factor (TNF-α), gamma interferon (IFN-γ), or interleukins IL-1, IL-3, IL-4, and IL-6.

However, the line between the powerful anti-inflammatory effects of GCs and their adverse effects is very thin. Whether the beneficial effects of their use are observed or their frequent adverse effects arise depends on factors such as concentration, duration of exposure, or route of administration (18).

1.3.3 Immunosuppressants

Immunosuppressing agents exert their immunomodulatory action through several mechanisms. On one hand, they inhibit the activity and proliferation of T and B lymphocytes[3], key cells of the immune system, which helps reduce inflammation and the autoimmune

[3] **Lymphocyte B:** The only type of cell capable of producing antibodies, thus mediating humoral immune responses. B lymphocytes develop in the bone marrow and are primarily found in lymphatic follicles in secondary lymphoid tissues, in the bone marrow, and in small numbers in the circulation.

Lymphocyte T: A key component of cellular immune responses in the adaptive immune system. T lymphocytes mature in the thymus, circulate in the blood, populate secondary lymphoid tissues, and are recruited to peripheral sites of antigen exposure. They express antigen receptors (TCRs) that recognize peptide fragments of foreign proteins bound to self-major histocompatibility complex (MHC) molecules. Functional subgroups include CD4+ helper T cells and CD8+ cytotoxic T cells.

response. Additionally, they stimulate the accumulation of extracellular adenosine in inflamed tissues, a mediator with potent anti-inflammatory effects that decreases the activation of neutrophils and other pro-inflammatory components. Finally, they also inhibits the production of pro-inflammatory cytokines such as TNF-α, IL-6, and IL-1, further supporting its role in controlling chronic inflammatory processes. Some examples include cyclophosphamide, methotrexate, azathioprine, cyclosporine, tacrolimus, and mycophenolate mofetil.

1.3.4 Immunotherapies

Biological therapies are highly specific drugs that modulate the immune system through the selective inhibition of key molecules involved in the pathogenic process of the disease. The first biological drugs became available in 1998, targeting TNF. Since then, new biological drugs have been developed and incorporated for the treatment of various chronic inflammatory diseases, such as rheumatoid arthritis, inflammatory bowel disease, and non-infectious uveitis. Their development represents a revolution in the treatment of autoimmune diseases.

The first to be used were TNF-α inhibitors, followed by the development of other biological drugs targeting different therapeutic pathways (18).

1.3.5 Therapies under development

1.3.5.1 RNA interference therapy

Small interfering RNAs (siRNAs), efficiently silence genes by inhibiting mRNA translation and promoting its degradation. In the treatment of autoimmune diseases, particularly rheumatoid arthritis (RA), siRNAs have been used to silence inflammatory genes such as TNF-α, Notch1, and NF-κB, effectively reducing inflammation and protecting damaged tissues. Various delivery systems, including hybrid nanoparticles, degradable cationic polymers, and conjugated liposomes, have proven effective in the targeted administration of siRNA.

Although research has primarily focused on RA, it is anticipated that with the advancement of drug delivery technologies, siRNA-based therapies will be applied to other autoimmune diseases and inflammatory conditions in the future (11).

1.3.5.2 Hematopoietic stem cell transplantation

Hematopoietic stem cell transplantation (HSCT) acts as a "reset" for the immune system in the treatment of autoimmune diseases. These diseases are characterized by an erroneous attack of the immune system against the body's own tissues due to the loss of immune tolerance[4], meaning the body's ability to recognize and not attack its own cells.

HSCT eliminates the defective immune cells responsible for this attack through a combination of chemotherapy and immunosuppressants, replacing them with new stem cells that help restore immune tolerance and rebalance the immune system.

HSCT, initially used in rheumatoid arthritis and multiple sclerosis, has proven effective in patients who do not respond to conventional treatments. However, risks such as infertility, heart damage, and increased susceptibility to infections and cancer must be carefully considered.

[4] **Tolerance**: Lack of responsiveness of the adaptive immune system to antigens as a result of antigen-specific lymphocyte inactivation or death induced by antigen exposure. Tolerance to self antigens is a normal feature of the adaptive immune system, but tolerance to foreign antigens can be induced under certain conditions of antigen exposure.

Despite the adverse effects, HSCT remains a viable option for autoimmune diseases due to its ability to rebalance the immune system and restore immune tolerance (11,19).

1.3.5.3 Chimeric antigen receptor-T cells (CAR-T cells)

CAR-T cells are specially engineered immune cells that combine the ability of B cells to recognize antigens with the killing power of T cells. Developed in the late 1980s, CAR-T cells can identify targets on the surface of cells without depending on the major histocompatibility complex (MHC)[5]. To create them, T cells are taken from a patient's blood, modified with CAR genes, multiplied in the lab, and then returned to the patient. CAR-T therapy targets specific tumor antigens, destroying tumor cells, and has proven very effective in treating B cell cancers.

In immune-mediated inflammatory diseases, CD8+ CD19 CAR-T cells have shown potential by successfully reducing B cell populations. Compared to monoclonal antibodies, CAR-T cells offer advantages such as longevity, ability to multiply, trafficking to target tissues, and development into memory cells that prevent the recurrence of pathogenic lymphocytes. As a result, CAR-T therapy may provide long-lasting therapeutic effects with a single dose.

Other chimeric modifications of T cells are also under investigation in autoimmune diseases:

CAAR-T cells: They destroy cells that express harmful autoantibodies, helping to manage antibody-mediated autoimmune diseases.

CAR-Tregs: They regulate immune activity, suppress inflammation, and promote immune tolerance toward specific antigens without destroying the target cells.

Both strategies represent innovative approaches to treating autoimmune diseases by reprogramming the immune system (19).

1.3.5.4 Therapeutic vaccination

Another promising therapeutic approach targeting pro-inflammatory cytokines is the use of vaccines to create a natural endogenous immune response against these cytokines. The most developed strategy is peptide-based active vaccination, aimed at directly neutralizing pathogenic cytokines. The Kinoid system involves creating a complex using the target cytokine linked to a highly immunogenic protein. This approach has the advantage of inducing a short-lived B cell memory response, resulting in an endogenous anti-cytokine effect that gradually diminishes if treatment is discontinued (19).

Another key proinflammatory cytokine involved in the pathogenesis of rheumatic diseases is TNFα, and vaccination against it has been proposed as an alternative approach to directly target TNFα in preclinical studies (20).

[5] **Major Histocompatibility Complex (MHC):** A membrane protein that presents peptides for recognition by T lymphocytes. Two structural types of MHC molecules exist: Class I MHC molecules, found on most nucleated cells, bind peptides derived from cytosolic proteins and are recognized by CD8+ T lymphocytes. Class II MHC molecules are mostly restricted to dendritic cells, macrophages, and B lymphocytes, binding peptides derived from endocytosed proteins and recognized by CD4+ T lymphocytes.

1.4 IMMUNOTHERAPIES

The advent of immunotherapies has revolutionized the treatment landscape for immune-mediated inflammatory diseases, offering targeted approaches that modulate specific components of the immune system. Unlike conventional immunosuppressive drugs, which broadly dampen immune responses, modern immunotherapeutics aim to interfere with key molecular and cellular pathways driving chronic inflammation. In this section, several major classes of immunotherapies will be discussed, including **TNF inhibitors**, **T cell costimulation blockers**, **interleukin (IL) inhibitors**, **anti-B cell therapies, combination of antibodies, combination of antibodies with other therapeutic drugs, bispecific antibody therapies and nanobodies**. Each of these strategies reflects a distinct mechanism of action, targeting cytokines, immune cell activation, or lymphocyte subsets involved in the pathogenesis of diseases such as rheumatoid arthritis, inflammatory bowel disease, and non-infectious uveitis. This section focuses on explaining these therapies.

1.4.1 Anti-TNF-α

TNF-α inhibitors block the inflammatory cascade by preventing the activation of TNF receptors (TNFR1 and TNFR2), thereby inhibiting the activation of immune cells such as macrophages and natural killer cells, as well as the production of other pro-inflammatory cytokines. This targeted inhibition reduces inflammation and helps prevent structural damage in affected tissues, including the intestinal mucosa, joints, and retina.

There are five TNF-α inhibitors: infliximab, adalimumab, etanercept, certolizumab pegol, and golimumab, which are biologic agents approved by both the FDA and EMA for the treatment of various autoimmune diseases. Several off-label indications have also been described (21).

Adalimumab is a monoclonal human antibody that is administered subcutaneously and can be injected by the patient himself (5). Adalimumab is an agent indicated for the treatment of 15 conditions, including adult and pediatric plaque psoriasis, hidradenitis suppurativa, RA, psoriatic arthritis, ankylosing spondylitis, non-radiographic axial spondyloarthritis, polyarticular juvenile idiopathic arthritis, enthesitis-related arthritis, adult and pediatric Crohn's disease (CD), ulcerative colitis (UC), adult and pediatric uveitis, and Behçet's disease (22,23). However, as other antiTNF-α, adalimumab contains an Fc fragment, which can be recognized by the immune system, especially when the molecule includes non-human components, as is the case with infliximab, a chimeric antibody (see Table 1). The presence of the Fc region enables interactions with immune cell receptors, potentially enhancing immunogenic responses and leading to the formation of anti-drug antibodies. This can directly impact the clinical efficacy and durability of response to TNF inhibitors.

Due to its wide range of clinical applications, its nature as a fully human monoclonal antibody with an Fc fragment, adalimumab is the anti-TNF selected in this thesis for the study of its *in vivo* biodistribution in three autoinflammatory pathologies: inflammatory bowel disease, rheumatoid arthritis, and non-infectious uveitis.

Table 1: **Comparative Anti-TNF-α agents**

Drug	Molecule Type	Approval Year (FDA/ EMA)	Route & Frequency	Structure / Fc Presence	Main Approved Indications
Infliximab	Chimeric mAb (25% mouse/ 75% human)	1998/ 1999	IV, every 6–8 weeks	Contains Fc region; full IgG1 antibody	RA, IBD
Adalimumab	Fully human mAb	2002/ 2003	SC, every 1–2 weeks	Contains Fc region; full IgG1 antibody	RA, IBD, uveitis
Etanercept	Fusion protein (TNF receptor linked to Fc of human IgG1)	1998/ 2000	SC, once or twice weekly	Contains Fc region; binds TNF-α and TNF-β	RA
Certolizumab pegol	PEGylated Fab fragment of humanized mAb	2008/ 2009	SC, every 2–4 weeks	Lacks Fc region; PEGylated to prolong half-life	RA, IBD
Golimumab	Fully human mAb	2009/ 2009	SC monthly or IV every 8 weeks	Contains Fc region; full IgG1 antibody	RA, IBD

1.4.2 T cell costimulation inhibitor

T-cell-targeted therapies represent a promising strategy for the treatment of multiple autoimmune diseases. The blockade of costimulation as an immunosuppressive strategy is based on the "two-signal rule" of T-cell activation (Figure 2). This rule posits that antigen recognition via the T-cell receptor alone is insufficient to trigger a T-cell response; an additional "costimulatory" signal is required, which is delivered after the binding of CD28 expressed on T cells to its ligands, CD80 (B7.1) or CD86 (B7.2). Consequently, inhibition of this second signal would impair T-cell immunity. In line with this, inhibition of the CD28 pathway, either through genetic deficiency or blockade, has been shown to improve autoimmunity (24). An example of co-stimulation inhibitor drugs is abatacept (CD80/CD86 blocker).

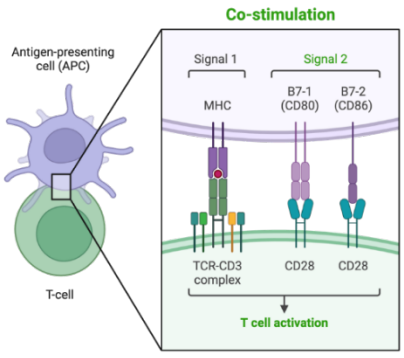

Figure 2: T-cell co-stimulation. Obtain from BioRender.com

1.4.3 Interleukin inhibitors

Interleukin blocking agents are a class of immunosuppressive drugs that inhibit the action of specific interleukins, which are cytokines crucial in regulating immune responses. These cytokines are synthesized by lymphocytes, monocytes, macrophages, and certain other cells. These agents are used to treat various inflammatory and autoimmune diseases. Some examples are Ustekinumab (IL-23/IL-12), secukinumab (IL-17), anakinra (IL-1) or dupilumab (IL-4/ IL-13).

1.4.4 Anti-B cells

B cells are key players in adaptive immunity[6] and immune memory but are also implicated in autoimmune diseases such as rheumatoid arthritis, lupus, and multiple sclerosis. They contribute to tissue damage through autoantibodies, pro-inflammatory cytokines like IL-6 and TNF-alpha, and T-cell activation. Additionally, B cells have regulatory functions via IL-10. Due to their central role, B cells are therapeutic targets in autoimmune diseases, with treatments being developed to selectively deplete them. Monoclonal antibodies have been developed to eliminate malignant B cells through antibody-dependent cellular cytotoxicity and complement-dependent cytotoxicity. Their effectiveness relies on effector cells and polymorphisms in their receptors, which influence antibody binding and therapeutic response. These antibodies target specific stages of B cell maturation based on their specificity. An example is the rituximab (antiCD20) (25).

1.4.5 Bispecific antibody therapies

Bispecific antibodies (BsAbs) are a new class of antibodies that can recognize two different antigens or two different epitopes of the same antigen. The successful generation of more than 100 BsAb formats has benefited from significant advancements in antibody engineering and antibody biology. Thanks to their strong multidirectional action capabilities, high binding potency, cell-binding action, and cascade amplification effects, they have been applied to the treatment of complex tumors and autoimmune diseases. Bimekizumab is the first BsAb approved by the FDA in 2021 and can selectively inhibit IL-17A and IL-17F simultaneously for the treatment of autoimmune diseases (11).

1.4.6 Nanobodies

Nanobodies originate from heavy-chain antibodies. The primary structural difference between nanobodies and conventional antibodies lies in their variable domains. Conventional antibodies possess two variable domains—VH (heavy chain) and VL (light chain)—which provide mutual stability and binding specificity. In contrast, nanobodies contain only a single variable domain, known as VHH (heavy chain variable domain), lacking VL domains. Despite this, nanobodies exhibit remarkable stability (19).

[6] **Adaptive Immune System:** Adaptive immunity, also called specific or acquired immunity, requires the proliferation and differentiation of lymphocytes before providing effective defense. Its potency arises from a massive expansion of antigen-specific lymphocytes, the highly specialized functions of different lymphocyte classes, and improved responses observed with repeated exposure to the same antigen (immune memory). Adaptive immune responses take days to develop, while innate immunity offers protection during the critical early window following infection.

To date, ten nanobodies have undergone evaluation in clinical trials. The first nanobody approved in Europe (September 2018) was caplacizumab, a fragment targeting von Willebrand factor. It inhibits the interaction between von Willebrand factor and platelets, offering a treatment for acquired thrombotic thrombocytopenic purpura. Ozoralizumab is a trivalent, bispecific nanobody that effectively neutralizes TNF-α while also binding to human serum albumin, thereby extending its *in vivo* half-life. This nanobody consists of two anti-TNFα domains and one albumin-binding domain. (19).

1.4.7 Therapeutic limitations of monoclonal antibodies

Despite the proven efficacy of mAbs, such as adalimumab, in the treatment of chronic inflammatory diseases, their therapeutic effect is not uniform in all patients. Clinical experience has shown that there are patients who do not respond initially, who do not achieve significant clinical improvement despite adequate dosing, and patients who do not respond secondarily, who initially respond but subsequently lose efficacy over time. One of the main factors underlying these differences is the development of anti-drug antibodies, which can neutralise the biological agent or accelerate its elimination, leading to subtherapeutic drug levels and treatment failure (11,26).

These phenomena highlight the intrinsic limitations and therapeutic ceiling of mAbs treatments. Several factors contribute to this ceiling, including: limited tissue penetration, especially in inflamed or fibrotic environments, pharmacokinetic variability between individuals and the influences of the route of administration in drug absorption, systemic exposure, and ultimately the amount of drug that reaches the site of action. To address these limitations, a number of strategies have been proposed. One major area of focus is therapeutic drug monitoring, which involves measuring serum drug levels and anti-drug antibodies to optimize dosing. This approach supports personalized treatment regimens that can be adjusted based on individual pharmacokinetic and pharmacodynamic profiles (26). However, an important caveat remains: while serum drug concentrations are routinely used as proxies for therapeutic activity, they do not always reflect the actual concentration of the drug at the target site. The lack of correlation between blood levels and drug levels in inflamed tissues complicates dose optimization and efficacy prediction. In this context, studying the *in vivo* biodistribution of biologic agents like adalimumab becomes essential to better understand therapeutic variability.

1.5 MOLECULAR IMAGING

Molecular imaging is a rapidly advancing field that enables the visualization, characterization, and quantification of biological processes at the molecular and cellular levels within living organisms. Unlike conventional imaging modalities that primarily provide anatomical information, molecular imaging focuses on functional and biochemical changes, offering powerful insights into disease mechanisms, progression, and response to therapy. This approach plays a crucial role in preclinical research, where it supports the noninvasive investigation of complex biological systems in animal models. Molecular imaging represents a effective tool because of its exceptional sensitivity and quantitative capabilities, making it an indispensable in early-stage biomedical research, particularly in drug development, disease modeling, and translational studies. As a result, imaging is regarded as a crucial link between preclinical research and clinical application (27,28).

1.5.1 Current technology

Several techniques are used in molecular imaging:

- Planar Scintigraphy: Produces two-dimensional (2D) images.
- Single-Photon Emission Computed Tomography (SPECT): A three-dimensional (3D) version of planar scintigraphy.
- Positron Emission Tomography (PET): Provides high-resolution metabolic imaging.

Additionally, miniaturized versions such as micro-SPECT and micro-PET are widely used in preclinical research, allowing detailed studies of disease mechanisms and the evaluation of new therapeutic approaches.

These imaging techniques continue to contribute to advancements in medical diagnostics and research, improving the understanding of physiological and pathological processes.

1.5.1.1 Positron Emission Tomography (PET)

Positron Emission Tomography (PET) is a non-invasive diagnostic imaging technique used to visualize and monitor physiological and metabolic processes. It relies on radioactive tracers molecules or radiopharmaceuticals that bind to specific target receptors within the body labeled with positron-emitting isotopes (Table 2). Each PET radioisotope has a specific physical half-life, which refers to the time it takes for half of the radioactive nuclei in a sample to decay. This value determines how quickly the isotope transforms into a more stable form by emitting radiation. The half-life directly influences the duration of usable radioactivity, which is critical for imaging protocols. For example, fluorine-18 has a half-life of about 110 minutes, making it ideal for short imaging procedures. In contrast, zirconium-89 (Zr-89) has a longer half-life of approximately 78 hours, allowing for delayed imaging and longer biological processes to be studied

Table 2: PET radioisotopes and their respective half life.

PET radioisotopes	Half life
Oxygen-15	2.04 minutes
Nitrogen-13	9.97 minutes
Carbon-11	20.33 minutes
Gallium-68	68 minutes
Fluorine-18	109.8 minutes
Copper-64	12.7 hours
Zirconium-89	78.4 hours
Iodine-124	4.18 days

Positron decay occurs in neutron-poor radionuclides and involves the conversion of a proton into a neutron, accompanied by the simultaneous emission of a positron (e+) and a neutrino (Figure 3). Since the positron has a very short lifetime, it quickly annihilates upon

interacting with an electron, generating two high-energy photons (E = 511 keV) that travel in approximately opposite directions (29).

These photons are detected by scintillating crystals and converted into electrical signals, which are then reconstructed to create detailed images of the tracer's distribution within the organ of interest. This enables functional assessment of various physiological processes.

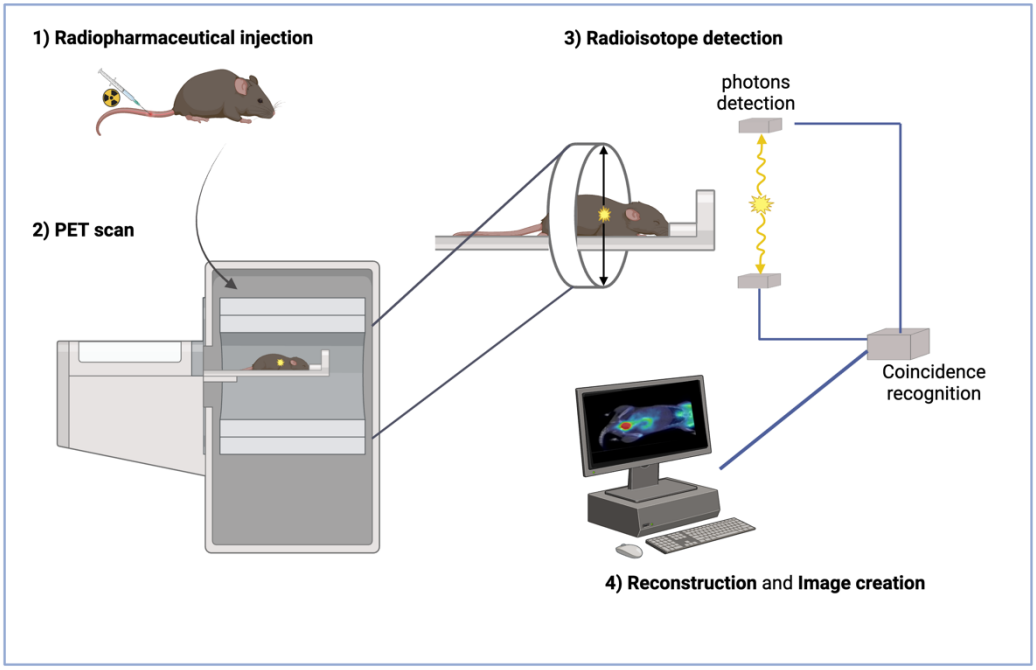

Figure 3: Principle of positron emission tomography (PET) imaging. 1) Intravenous radiopharmaceutical injection. 2) PET scan. 3) Positron annihilation and coincidence detection. 4) Image reconstruction and creation. Created with BioRender.com

1.5.1.1.1 Preclinical and PET scanners

Preclinical and clinical PET imaging systems share a common physical basis, but the characteristics of each component of the imaging process must differ between these groups due to large differences in body size and mass. Rodents such as mice and rats differ significantly in body weight from adult humans, by several thousand-fold in the case of mice, and several hundred-fold for rats. Moreover, the dimensions of key organs of interest, such as the liver and brain, are typically on the scale of centimetres or less, with many critical anatomical structures being even smaller. Therefore**, spatial resolution** must be significantly higher in small animal studies (1-1.5 mm) than in human studies (3-6 mm) to accurately quantify the radioactivity within these small anatomical structures.

The **partial volume effect** (PVE) arises when anatomical structures are smaller than approximately two to three times the spatial resolution of the scanner, leading to underestimation of tracer uptake due to signal 'spillover' into surrounding tissues. In microPET imaging, this effect is particularly pronounced, as most rodent organs and lesions fall within or below this resolution threshold. As a result, PVE poses a major challenge for accurate quantification in preclinical studies, necessitating advanced correction techniques and high-resolution anatomical references (e.g., CT or MRI) to obtain reliable data (30).

In contrast, clinical PET imaging is less affected by PVE in many cases, since human organs and pathological lesions are generally much larger than the scanner's resolution. While PVE still impacts the quantification of small tumors or thin structures (e.g., cortical brain regions), its overall influence is less severe compared to microPET. Consequently, although PVE correction is used in clinical practice, it is often optional or reserved for specific applications, whereas in preclinical PET it is essential for meaningful interpretation of most imaging data (30).

1.5.1.2 Computed tomography (CT)

CT provides detailed anatomical cross-sectional images by calculating the attenuation of X-rays in individual tissue volume elements (voxels). This data is used to create three-dimensional (3D) matrix images, from which sectional or spatial representations can be reconstructed. A typical CT device consists of an X-ray tube and a 2D X-ray detector positioned opposite each other within a structure that rotates around the examined object.

X-ray attenuation primarily depends on tissue density and the atomic number of the elements within the voxels. Tissues with higher atomic numbers and greater densities, such as bone, produce high-contrast images with sharp detail. In contrast, soft tissues, which have lower atomic numbers and densities, exhibit poor contrast. As a result, contrast agents are often used to enhance their visibility in CT imaging (31).

1.5.1.3 Hybrid Scanners: PET/CT

Given the problem of the anatomical localization of the metabolic and physiological processes obtained with PET, it is proposed to add a CT scanner to the PET scanner, in order to make the 2 examinations continuous. CT is frequently used in conjunction with other imaging modalities as an anatomical reference. In this way it is possible to compare the location of a lesion before and after treatment or the pharmacokinetics of a drug over time. To this end, efforts are made to coregister two sets of digital images. In co-registration, the matrix size, voxel intensity, and the rotation are adjusted to establish a one-to-one spatial correspondence between the two images. This process is called the alignment of images (32).

1.5.2 PET in clinical immune-mediated inflammatory diseases

Clinically, PET is most commonly performed using [^{18}F]FDG (2-deoxy-2-[^{18}F]fluoro-D-glucose) as a radiotracer. The primary areas of application include oncology, neurology, and cardiology. However, recent clinical trials have begun to explore its potential utility in immune-mediated inflammatory diseases such as rheumatoid arthritis (RA) and inflammatory bowel disease (IBD). The standard clinical practice typically involves comparing FDG-PET scans before and after therapeutic interventions to assess treatment response (33–35). Nevertheless, ongoing research is investigating strategies to incorporate PET into routine clinical evaluation. In the context of IBD, for instance, some studies have compared [^{18}F]FDG PET findings not only with conventional blood biomarkers but also with fecal biomarkers used during the diagnostic process (36–38). PET imaging offers the advantage of localizing inflamed or damaged tissue throughout the entire bowel, providing valuable spatial and functional information that complements traditional diagnostic tools.

1.5.3 PET role in preclinical research

PET plays a pivotal role in preclinical research by offering noninvasive, quantitative, and highly sensitive imaging of molecular and cellular processes in living animal models. Its applications span several key areas, including the investigation of disease mechanisms, drug development, translational research, and imaging biomarkers (39,40). In the investigation of disease mechanisms, PET enables *in vivo* visualization and quantification of radiolabeled biomolecules, providing critical insights into the pathophysiology of diseases. This capability supports research across a range of fields, such as oncology, neurology, cardiology, and metabolic disorders. In drug development, PET is widely utilized to evaluate the pharmacokinetics, biodistribution, and therapeutic efficacy of novel drug candidates during early-stage research. It facilitates the monitoring of drug–target interactions, the assessment of early biological responses, and the optimization of dosing regimens prior to clinical trials. Regarding translational research, findings from preclinical PET studies in small animal models contribute significantly by bridging the gap between laboratory discoveries and clinical application, thereby enhancing the predictive value of preclinical data and supporting a more efficient progression to human studies. Finally, as a tool for imaging biomarkers, PET offers a noninvasive means of detecting and quantifying disease-specific biomarkers, which is essential for early diagnosis, disease staging, and monitoring of treatment response.

1.5.3.1 Immuno-PET

Immuno-PET represents a significant advancement in molecular imaging, synergistically combining the high target specificity of monoclonal antibodies (mAbs) with the inherent sensitivity of PET. Immuno-PET allows for the longitudinal and non-invasive visualization and quantification of target biomarker expression *in vivo*, providing whole-body biodistribution data. The development of diverse immunoPET probes has been facilitated by extensive research and optimization of radiochemistry and conjugation techniques, incorporating a variety of radionuclides and mAbs (41,42).

Effective immunoPET imaging requires fast and specific radiolabeling of antibody vectors. Achieving optimal results requires high target-specific uptake with minimal background retention. This necessitates the rapid saturation of target sites by the tracer, followed by swift clearance of unbound tracer from circulation. Consequently, the successful design of immunoPET probes critically relies on careful selection of targeting vectors, radioisotopes, bifunctional chelators, conjugation and radiolabeling methods. In other words, a good radiopharmaceutical.

1.5.3.2 Radiopharmaceuticals

The radiopharmaceutical is a compound made up of different parts (targeting vector, radioisotope and not always a bifunctional chelator) that must be in sync. Depending on the type of targeting vector, a radioisotope with a similar half-life must be selected. For example, if the vector is a small molecule with fast kinetics, it is best radiolabelled with a short half-life radioisotope, as F-18. However, if the vector has slower kinetics, such as in the case of monoclonal antibodies, it is best to select a radioisotope with a half-life that matches the half-life of the vector, for example Zr-89.

Radiopharmaceuticals comprise a class of radioactive compounds utilized in both diagnostic and therapeutic applications. These agents demonstrate selective tissue localization as a result of their biomolecular properties, a characteristic that accounts for the areas of hyperintensity observed in PET imaging, which correspond to regions of increased metabolic

activity. Unlike structural and anatomical imaging, molecular imaging provides functional insights by capturing the dynamic interaction between a targeted probe (radiopharmaceutical) and the biological system. Due to its exceptional sensitivity and recent advancements in quantitative imaging PET has become a widely utilized tool for disease staging and drug development. Notably, only minimal amounts of radiopharmaceutical are required to generate high-quality images. This high sensitivity allows PET radioligands to investigate biological processes without inducing pharmacological effects. However, radiopharmaceuticals continuously emit radiation, necessitating more stringent storage requirements compared to non-radioactive pharmaceuticals (43,44).

In this doctoral thesis we have worked with 2 different radiopharmaceuticals, [^{18}F]FDG and [^{89}Zr]Zr-DFO-adalimumab.

1.5.3.2.1 Conjugation

Conjugation is the covalent attachment of a bifunctional chelator to the monoclonal antibody, to enable stable radiolabeling with a radioactive isotope. This process ensures that the Zr-89 remains securely bound to the adalimumab without altering its biological properties. The chelator used is the acyclic chelator deferoxamine (DFO) that has been developed and recognized as a gold standard chelator for Zr^{4+} (43).

1.5.3.2.2 Radiolabeling

The amount of radioactivity required for an experiment is influenced by multiple factors, including the species of rodent used. For instance, rats, due to their larger size compared to mice, necessitate a higher quantity of radioactivity. Additionally, the duration of the study plays a critical role; longer study periods demand increased radioactivity. The required radioactivity is typically calculated based on the **specific activity**, which is defined as the radioactivity per gram of the antibody administered. This value must remain consistent across all individuals within the experiment to ensure uniformity.

1.5.3.2.3 [^{18}F]FDG (2-deoxy-2-[^{18}F]fluoro-D-glucose)

[^{18}F]FDG, [^{18}F]-fluorodeoxyglucose, approved by FDA (1990) and EMA (2001) is an analogue of glucose whereby the 2´ hydroxyl group has been substituted with ^{18}F (Figure 4). It has been extensively employed in patient diagnosis, disease staging, and therapy monitoring across a range of multiple conditions. Cells that are more metabolically active, such as inflammatory, infected or cancer cells, will take up more [^{18}F]FDG than normal cells. This allows to see areas of increased metabolic activity on PET scans. However, [^{18}F]FDG PET scans have some important limitations to the test. For example, [^{18}F]FDG can be taken up by different types of cells, which can lead to false positives, without distinguishing a high metabolic intake from a tumor, localised inflammation or normal tissues with a high glucose turnover (45). It should be clear that what it provides is just information on a higher metabolic uptake.

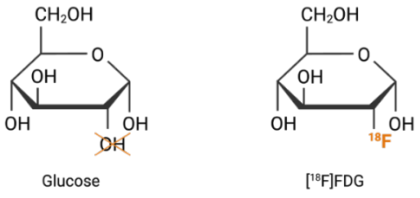

Figure 4: Glucose and [^{18}F]FDG differentiation.

1.5.3.3 Animal models

Research with preclinical models has allowed us to advance the knowledge of different pathologies, such as inflammatory bowel disease, non-infectious uveitis and rheumatoid arthritis, as well as the development of new methodologies, such as immuno-PET based on the study of adalimumab, which has provided extensive knowledge in the field of autoimmune diseases and pharmacology.

Mammals share biological and immunological similarities, which is why rodent models are crucial for reducing risks to humans. However, animal experimentation must be strictly regulated and guided by the 3Rs principle: Replacement, Reduction, and Refinement. This means replacing animal use with alternatives such as *in vitro* models whenever possible, reducing the number of animals used, and refining procedures to ensure animal welfare while minimizing pain and distress (46,47).

1.5.3.3.1 Monitoring and control of animal care in imaging

The use of preclinical imaging systems, in addition to **reducing** the number of animals due to the study of the same animal over time, offers a solution for physiological monitoring and control of small animals during imaging procedures, leading to a **refinement** of the research. It features fully integrated anesthesia compatible with most commercial gas anesthesia systems, such as in our case isofluorane, and a reliable and easy-to-use animal handling system with rat and mouse beds. It also includes monitoring of physiological signals such as respiration. In short, these systems ensures animal welfare and accurate data acquisition during imaging procedures. This has provided us with high quality images to study the biodistribution of radiolabelled adalimumab.

1.6 PET AND IMMUNE-MEDIATED INFLAMMATORY DISEASES

Immune-mediated inflammatory diseases (IMIDs) represent a heterogeneous group of disorders marked by chronic inflammation resulting from dysregulated immune responses. Among the most clinically significant IMIDs are inflammatory bowel disease, non-infectious uveitis, and rheumatoid arthritis, due to their high prevalence, systemic manifestations, and substantial impact on patient quality of life. A major challenge in the management of these conditions is the accurate assessment of disease activity and treatment response. In this thesis, particular emphasis is placed on the use of PET as a non-invasive imaging modality to monitor and evaluate inflammatory processes in IMIDs. Specifically, PET imaging with the radiolabelled biologic antibody anti-TNF-α [^{89}Zr]Zr-DFO-adalimumab is investigated for its potential to provide spatial and functional information about TNF-α mediated inflammation. This approach is examined as a means to complement, and potentially enhance, traditional diagnostic and monitoring strategies in the context of immune-driven diseases.

2. JUSTIFICATION AND HYPOTHESES

Immune-mediated inflammatory diseases, such as IBD, non-infectious uveitis, and RA, represent a group of chronic and debilitating disorders with rising incidence in developed countries. Despite manifesting in different organ systems, these diseases share overlapping molecular pathways, notably the overexpression of pro-inflammatory cytokines like TNF-α. Anti-TNF-α biologic agents, such as adalimumab, have significantly improved the treatment of this type of disease. However, its variable efficacy, dependent on factors that remain poorly understood, poses a major clinical challenge.

Current clinical strategies, including therapeutic drug monitoring to adjust dosing based on serum drug concentrations, have partially addressed the issue of non-response. This highlights a critical gap in our understanding of how these drugs behave *in vivo*, specifically, their biodistribution under different pathological and physiological conditions. Understanding how factors such as route of administration and disease location influence this could improve the personalization and efficacy of therapy.

PET imaging presents a powerful, non-invasive tool for tracking the *in vivo* dynamics of biologics such as adalimumab. By employing PET to visualize and quantify the distribution of radiolabelled adalimumab in various murine models of immune-mediated inflammatory diseases, this project aims to elucidate the key factors that govern therapeutic targeting and availability. These findings may contribute to the rational design of improved therapeutic strategies and foster a deeper mechanistic understanding of adalimumab therapy.

Hypotheses:

General hypothesis

We hypothesize that PET imaging with [^{89}Zr]Zr-DFO-adalimumab enables accurate characterization of the *in vivo* biodistribution and pharmacokinetics of anti-TNF-α therapy across different immune-mediated inflammatory disease models (IBD, uveitis, and arthritis). We further propose that biodistribution patterns are modulated by the route of administration, the location of the inflammatory lesions, and the local expression levels of TNF-α, and that these parameters can inform therapeutic decision-making and personalized treatment strategies. In particular, we propose several specific hypothesis:

- **Specific hypothesis 1:** Adalimumab biodistribution is affected by the administration route. The route of administration (subcutaneous vs intravenous or intravitreal) significantly influences the systemic and tissue-specific distribution of adalimumab antibodies, potentially impacting therapeutic efficacy.
- **Specific hypothesis 2:** Adalimumab biodistribution is affected by disease localization. The localization of disease (systemic versus organ-specific) modulates adalimumab biodistribution, with greater accumulation expected in tissues where inflammatory activity and TNF-α expression are concentrated.
- **Specific hypothesis 3:** Adalimumab biodistribution is affected by the effect of TNF-α expression levels. Elevated TNF-α levels, whether systemic or localized, affect the extent and pattern of adalimumab accumulation and retention in inflamed tissues, shaping its biodistribution profile.

3. OBJECTIVES

To develop and apply a PET-based methodology using [^{89}Zr]Zr-DFO-adalimumab to characterize and compare the *in vivo* biodistribution of anti-TNF-α therapy in preclinical models of immune-mediated inflammatory diseases, providing translational insights for optimizing biologic treatment strategies.

In order to achieve this purpose, specific objectives were set in each chapter, including:

Chapter 1: **Adalimumab PET in IBD model**

To assess how the route of administration and intestinal inflammation affect the biodistribution and pharmacokinetics of [^{89}Zr]Zr-DFO-adalimumab in a murine model of colitis, and to correlate these findings with intestinal TNF-α expression.

1.1 Validate the dextran sulfate sodium (DSS) IBD model in mice.

1.2 Compare the biodistribution of [^{89}Zr]Zr-DFO-adalimumab following subcutaneous (SC) and intravenous (IV) administration in both healthy and IBD model animals.

Chapter 2: **Adalimumab PET in uveitis model**

To evaluate the capacity of [^{89}Zr]Zr-DFO-adalimumab to reach ocular tissues in a systemic model of uveitis, analyzing the impact of administration route and local TNF-α expression on ocular targeting and retention.

2.1 Compare the ocular accumulation of [^{89}Zr]Zr-DFO-adalimumab between subcutaneous (SC) and intravitreal (IVT) administration.

2.2 Evaluate the *in vivo* biodistribution of [^{89}Zr]Zr-DFO-adalimumabfollowing SC and IVT administration in both healthy and non-infectious model animals.

Chapter 3: **Adalimumab PET in arthritis models**

To investigate the systemic biodistribution of [^{89}Zr]Zr-DFO-adalimumab in a murine model of arthritis, focusing on joint-specific accumulation.

3.1 Investigate the longitudinal uptake of [^{89}Zr]Zr-DFO-adalimumab in different joints in the K/BxN arthritis model.

3.2 Correlate [^{89}Zr]Zr-DFO-adalimumab with TNF-α expression in both blood and joint tissues in arthritic and healthy animals.

4. General methods

The core methodologies employed throughout this doctoral thesis are outlined below. These include radiopharmaceutical production and quality control, the design of acquisition protocols for Bruker PET/CT imaging scanner, including image reconstruction and image quantification, and finally blood sample analysis and *ex vivo* studies. While these methods are applied across the presented in this thesis, they have been adapted as necessary to meet the specific requirements and objectives of each individual chapter.

4.1 Production of [^{89}Zr]Zr-DFO-Adalimumab

This thesis is grounded on the generation and production of new compound ([^{89}Zr]Zr-DFO-adalimumab), which is a radiopharmaceutical essential for developing the novel PET-based methodology proposed in this work. [^{89}Zr]Zr-DFO-adalimumab is produced with Zr-89 PET radioisotope, and a monoclonal antibody targeting tumor necrosis factor-alpha (antiTNF-α) adalimumab (Imraldi® 40 mg, Biogen S.L, Madrid, Spain).

The [^{89}Zr]Zr-DFO-adalimumab creation process consists of two main steps: conjugation, where a bifunctional chelator is added to the antibody and acts as a link between the antibody and the radioactive isotope. And radiolabeling process, where the radioactive isotope is binding to the mAb (Figure 5).

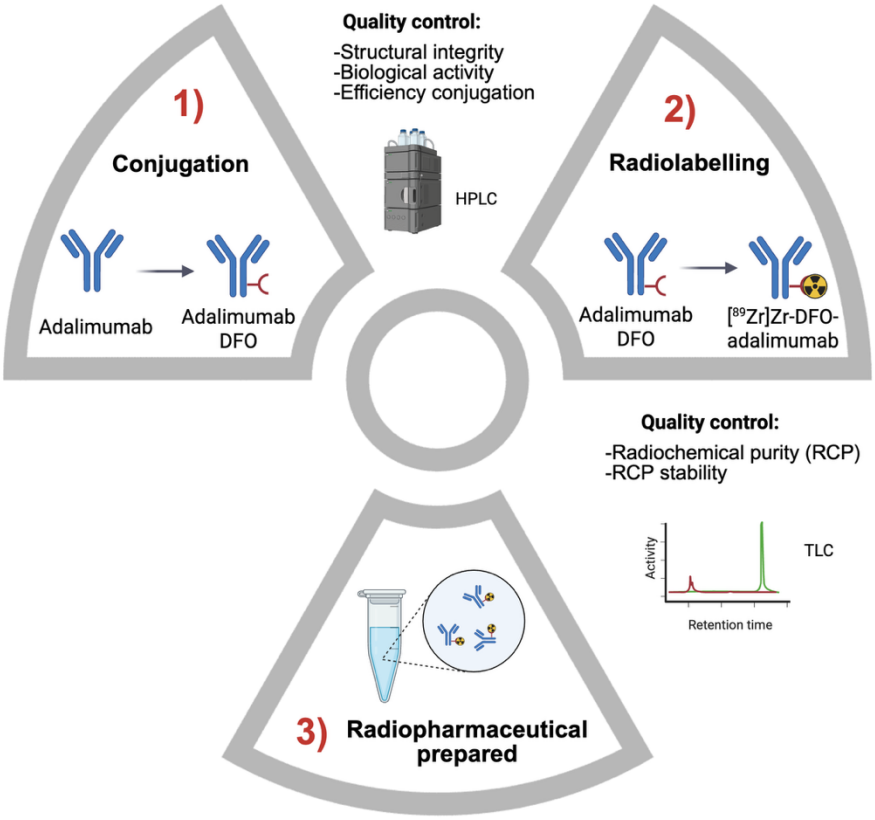

Figure 5: Radiopharmaceutical preparation for injection. 1) Conjugation process followed its quality control. 2) Radiolabelling process followed by its quality control. 3) Once the radiopharmaceutical passes all quality control tests, it is deemed ready for injection. Created with BioRender.com

4.1.1 Conjugation

First, adalimumab (anti-TNF-α) is purified using Amicon Ultra-2 mL centrifugal filters (30 kDa NMWL, Merck Millipore, Burlington, MA, USA) with Milli-Q water to remove excipients present in the commercial formulation. Following purification, a two-fold molar excess of tetrafluorophenyl-N-succinyldeferoxamine-B-Fe^{3+} (TFP-N-sucDf-Fe) (ABX, Radeberg, Germany) is added to facilitate conjugation. The conjugation reaction is conducted at 25 °C for 30 minutes under continuous agitation, with the solution adjusted to a pH range of 9.0–9.5 using 0.1 M Na_2CO_3. Upon completion of the reaction, the pH is lowered to 4.0–4.5 using 0.25 M H_2SO_4, followed by the addition of a 50-fold excess of 25 mg/mL ethylenediaminetetraacetic acid (EDTA) to chelate the iron from the TFP-N-sucDf-Fe complex. The mixture is then incubated at 30 °C for an additional 30 minutes.

The conjugated adalimumab is further purified. Finally, the N-sucDf-adalimumab conjugate is stored at -80 °C to preserve its stability under optimal conditions.

4.1.1.1 Conjugation Quality Control

The biological activity of conjugated adalimumab is evaluated using a commercial enzyme-linked immunosorbent assay (ELISA). Specifically, a sandwich ELISA is employed, utilizing wells pre-coated with anti-adalimumab monoclonal antibodies. The assay is performed using the Promonitor kit (Proteomika S.L., a subsidiary of Progenika Biopharma S.A., Spain) and analyzed with the Triturus ELISA Instrument (Grifols®, Barcelona, Spain).

The structural integrity of the monoclonal antibody and the efficiency of the conjugation process are further assessed by radio-high performance liquid chromatography (radio-HPLC) (Agilent 1260 Infinity II, Santa Clara, CA, United States). The analysis is conducted using a size exclusion chromatography column (Agilent Bio SEC-5, 5 µm, 300 Å, 7.8 × 150 mm) with phosphate-buffered saline (PBS) as the mobile phase, operating at a flow rate of 0.7 mL/min.

4.1.2 Radiolabelling

Depending on required radioactivity, the volume of the [^{89}Zr]oxalate solution (BV Cyclotron VU, PerkinElmer, Inc., The Netherlands) is measured for further processing. Then, the pH is adjusted to 4.0–4.5 using 2 M sodium carbonate (Na_2CO_3). Subsequently, the pH is further increased to 7.0 with 0.5 M HEPES buffer, after which the previously conjugated adalimumab mAb is added. The reaction mixture is incubated at 24 °C with continuous agitation at 550 RPM for 1.5 hours (48). After quality control confirms that the radiolabelling process has been correct, the radiolabelled antibody is injected.

Following radiolabeling, the radiochemical purity (RCP) of the radiolabeled mAb is determined using a radio-instant thin layer chromatography (radio-iTLC) system. The mobile phase consists of a 25 mg/mL ethylenediaminetetraacetic acid (EDTA) solution, while the solid phase is a silica gel-impregnated chromatography paper (Agilent Technologies, Santa Clara, CA, USA). A 1.5 µL sample is applied to the solid phase and analyze using the RITA TLC radioactivity detector system (RITA, Elysia-Raytest, Angleur, Belgium). The RCP percentage is subsequently calculated using Gina Star Software (RITA, Elysia-Raytest, Angleur, Belgium).

Additionally, an RCP stability study is conducted in human serum over 168 hours to assess the long-term stability of the radiolabeled mAb throughout the study period.

4.2 [^{18}F]FDG

[^{18}F]FDG, [^{18}F]-fluorodeoxyglucose, is a glucose analogue widely used in patient diagnosis, disease staging, and therapy monitoring across various medical conditions. Before this test, it is important to fast so that dietary glucose does not compete with [^{18}F]FDG in the body. [^{18}F]FDG works by being taken up by cells in the body.

All over this thesis [^{18}F]FDG was suministered by the Galician PET Radiopharmacy Unit (GALARIA) of the University Clinical Hospital in Santiago de Compostela (Spain) and administered intravenously.

4.3 ALBIRA PET/CT (BRUKER)

4.3.1 Technical Specifications

The Albira PET/CT system is a state-of-the-art preclinical imaging platform that integrates PET and CT into a single cohesive unit. Designed specifically for research in small animal models, such as mice and rats, this system is widely used in various fields of biomedical investigation. ().

- **PET Module:**
  - Continuous crystal detectors.
  - 80 mm field of view.
  - Up to 1.5 mm resolution.
- **CT Module:**
  - 50 kV X-ray tuve.
  - 65 mm field of view.
  - Micron-level resolution.

4.3.2 Key features and capabilities

- **Multimodal imaging:** The Albira PET/CT system provides the capability to acquire both PET and CT images sequentially. This multimodal approach allows for the acquisition of both functional (PET) and anatomical (CT) data, providing a more comprehensive understanding of biological processes and disease states.
- **High resolution imaging:** The system is engineered to deliver high-quality images with exceptional spatial resolution. This level of detail enables researchers to visualize and analyze small structures and subtle changes within tissues and organs, facilitating the study of intricate biological processes.
- **Rapid acquisition:** The Albira PET/CT system is designed for rapid image acquisition, minimizing scan times and improving animal throughput. This feature is particularly valuable in longitudinal studies and when working with animal models that require anesthesia. In this thesis each scan lasted between 20 and 35 minutes.
- **Integrated software platform:** The system is equipped with a user-friendly software suite that streamlines the entire imaging workflow, from data acquisition and

reconstruction to image visualization. This integrated approach enhances efficiency and facilitates data interpretation.

4.3.3 Adquisition protocols

In this thesis, PET/CT studies are performed using the Albira PET/CT hybrid system (Figure 6) (Bruker Biospin Corp., Billerica, MA). The protocol consisted of a 10-minute whole-body PET scan, followed by two 10-minutes CT scans (35 kV, 200 µA tube current, with 250 projections per bed).

- **Figure 6: Albira PET/CT scan. Obtain from https://www.bruker.com/es/products-and-solutions/preclinical-imaging/nmi/albirasi.html**

4.4 PET TOMOGRAPHIC RECONSTRUCTION

4.4.1 PET Tomographic reconstruction

PET tomographic reconstruction is the process by which the original distribution of the radiotracer is estimated from the sinograms or projection data obtained during the PET acquisition. The most common reconstruction methods are two: analytical and iterative.

Analytical methods are mathematically direct techniques that apply a formula to transform the projection data into an image. Filtered back-projection is the most common analytical reconstruction algorithm for 2D-PET image reconstruction due to its low computational requirements and to its simplicity(49).

In contrast, iterative methods rely on statistical modelling and apply a repetitive algorithmic process to iteratively refine the image. These methods improve the agreement between estimated and measured projection data by updating the image through successive approximations. Unlike analytical techniques, iterative methods significantly reduce reconstruction artifacts and yield improved signal-to-noise ratios, resulting in higher-quality images.

4.4.2 Tomographic reconstruction protocols

For the purposes of this thesis, image reconstruction was performed using an iterative protocols, specifically the Maximum Likelihood Expectation Maximization (MLEM) algorithm. MLEM is a statistical reconstruction technique that estimates the most probable radiotracer distribution that could have produced the observed projection data. A total of 12 iterations were performed using a voxel size of 0.5 x 0.5 x 0.5 mm³ were used. Corrections for scattering and random coincidences were applied to the PET images, while attenuation correction was not performed. CT images were reconstructed using the same voxel dimensions of 0.5 x 0.5 x 0.5 mm³.

4.5 IMAGE ANALYSIS

PET image analysis was performed using PMOD v4.2 software (PMOD Technologies, Zürich, Switzerland). Initially, PET and CT images were accurately fused to ensure precise localization and consistency across all measurements. The mean radioactivity concentration was determined for different manual volumes-of-interest (VOIs) located in the area under analysis, as colon, eyes or joints. It was corrected for decay and expressed in terms of SUV in the chapters where [^{18}F]FDG was used (Chapters 1 and 3), or as percentage of injected dose per millilitre (%ID/mL) in the chapter where it was not used (Chapter 2), as follows:

$$SUV = \frac{Mean\ radioactivity\ concentration\ in\ VOI\ (kBq/ml)}{Injected\ dose\ (kBq)} * body\ weight\ (g)$$

$$\%ID/ml = \frac{Mean\ radioactivity\ concentration\ in\ VOI\ \left(\frac{kBq}{ml}\right) * Volume\ of\ VOI\ (ml)}{Injected\ dose\ (kBq)} * 100$$

4.6 BLOOD ANALYSIS

Blood samples were collected with a micropipette from the tail vein of each animal before each PET scan while maintaining the anesthesia. It was analyzed using a well counter (Atomlab® Wipe Test Counter, Biodex®, New York, USA) to determine the radioactivity concentration at various time points. The radioactivity concentration in the blood was corrected for radioactive decay and branching of Zr-89, blood volume, and the dose injected as %ID/ml, using the expression:

$$\%ID/ml = \left(\frac{Blood\ radioactivity\ (kBq) * decay\ (kBq)}{Blood\ volume\ (ml)}\right)/ID\ (kBq) * 100$$

4.7 EX VIVO STUDY

At the end of every experiment, animals were perfused with phosphate-buffered saline (PBS) and 10 % formalin solution and euthanized under deep anesthesia by heart removal. This was done in order to eliminate the blood fraction and measure only the antibody bound in each organ.

4.7.1 *Ex vivo* binding per organ

Organs of interest were harvested following thorough perfusion to eliminate residual blood, and their radioactivity was measured using a well counter (Atomlab® Wipe Test Counter, Biodex®, New York, USA). The radioactivity concentration in the organ was corrected for radioactive decay and branching of Zr-89, organ weight, and the dose injected as %ID/g, using the expression:

$$\%ID/g = \left(\frac{organ\ radioactivity\ (kBq) * decay\ (kBq)}{organ\ weight\ (g)}\right) \Big/ ID\ \left(\frac{kBq}{ml}\right) * 100$$

4.7.2 Histopathological analysis

After the animals were perfused, their organs were extracted and stored first in formalin for 24 h and then transferred to PBS to eventually carry out the histological evaluation. Organs were dehydrated, embedded in paraffin, and sectioned into 4 μm thick slices. Subsequently, tissue sections from each animal were stained with hematoxylin and eosin (H&E). Tissues were first deparaffinised by incubating them in an oven at 60°C for 1 hour, allowing for the removal of paraffin. Following this, the sections were immersed in xylene for three consecutive washes, each lasting 10 minutes. Next, the tissues were rehydrated through a graded series of alcohol solutions, beginning with absolute ethanol for 5 minutes, followed by 96% ethanol for 5 minutes, 70% ethanol for 5 minutes, and 50% ethanol for 5 minutes. To stain the samples, they were then immersed in alcoholic eosin for 5 minutes. After eosin staining, the sections were rinsed in distilled water for 10 minutes to remove any excess dye. Following this, the tissue was dehydrated in a graded series of alcohol solutions, starting with 70% ethanol, then 96% ethanol, followed by absolute ethanol, and finally xylene. The tissue sections were then stained with hematoxylin for 10 minutes to enhance cellular structure visualization. Finally, the sections were mounted using a suitable mounting medium and prepared for microscopy análisis to identify differences with controls, areas of damage and/or leukocyte infiltration.

4.8 STATISTICAL ANALYSIS

Statistical analysis was performed using IBM SPSS Statistics 27 software (Armonk, New York, USA). Descriptive data are presented as the mean ± standard deviation (SD), while inferential data are expressed as the estimated marginal mean (EMM) ± standard error (SE). Correlated data were analyzed using generalized estimating equations (GEE) with an independent correlation matrix. Data at specific time points were analyzed using an unpaired t-test. Statistical significance was set at $p < 0.05$, without correction for multiple comparisons.

CHAPTER I

PET BIODISTRIBUTION STUDY OF SUBCUTANEOUS AND INTRAVENOUS ADMINISTRATION OF ADALIMUMAB IN AN INFLAMMATORY BOWEL DISEASE MODEL

ABSTRACT

Monoclonal antibodies targeting tumor necrosis factor-alpha (anti-TNF-α), such as adalimumab, are commonly employed in the treatment of immune mediated disorders including inflammatory bowel disease (IBD). Nonetheless, 20–40% of IBD patients exhibit non-responsiveness to anti-TNF-α therapies. A deeper understanding of their pharmacokinetic behavior could facilitate optimization of therapeutic efficacy. This study aims to compare the biodistribution and pharmacokinetics of adalimumab administered intravenously (IV) versus subcutaneously (SC) in a murine model of IBD using positron emission tomography (PET) imaging.

IBD was induced in mice via oral administration of dextran sulfate sodium (DSS), with disease confirmation achieved through [^{18}F]FDG PET/CT imaging, body weight monitoring, and histopathological evaluation of colonic tissue. Adalimumab was radiolabelled with zirconium-89 (Zr-89) and administered via IV or SC routes. Biodistribution was assessed using a dedicated small-animal PET/CT scanner over a 7-day period. Standardized uptake values (SUVs) were quantified in the colon, liver, and blood.

Results indicated a more rapid clearance of [^{89}Zr]Zr-Adalimumab in IBD mice compared to controls, and following IV administration compared to SC (SUV at 168 h post-injection: SC-IBD = 0.06 ± 0.02, SC-Control = 1.08 ± 0.11, IV-IBD = 0.02 ± 0.01, IV-Control = 0.26 ± 0.13). IBD mice exhibited accelerated systemic clearance and an earlier, more pronounced colonic uptake following IV administration (SUV at 6 h: IV-IBD = 2.11 ± 0.18) compared to SC (SUV at 24 h: SC-IBD = 1.49 ± 0.27).

These findings underscore the critical influence of both the administration route and TNF-α expression levels on the biodistribution and tissue targeting of anti-TNF-α , with potential implications for enhancing therapeutic strategies in IBD.

Keywords: *antiTNF-α, adalimumab, immunoPET, inflammatory bowel disease, intravenous administration, subcutaneous administration.*

GRAPHICAL ABSTRACT

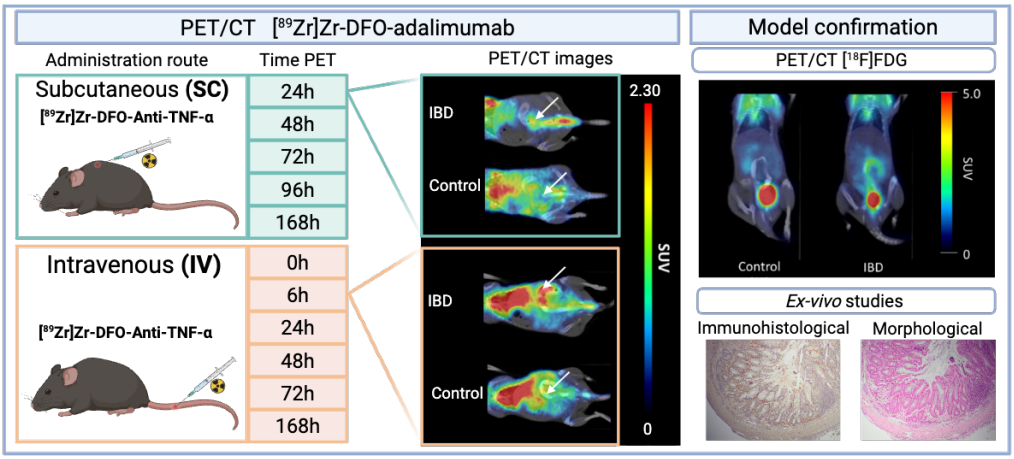

Figure 7: The graphical abstract illustrates the PET time points for both subcutaneous and intravenous groups, along with the key findings from the [^{89}Zr]Zr-DFO-Anti-TNF-α, [^{18}F]FDG, and histopathological analyses. Created with BioRender.com

1.INTRODUCTION

Inflammatory bowel disease (IBD) encompasses a group of chronic, immune-mediated inflammatory disorders primarily affecting the gastrointestinal tract, with Crohn's disease and ulcerative colitis being the most prevalent forms (50). Although the ethology of IBD remains incompletely understood, it is widely accepted that a complex interplay between genetic susceptibility, gut microbiota, environmental triggers, and immune dysregulation underpins disease onset and progression (26,51,52). A key feature of IBD pathogenesis is the imbalance between pro- and anti-inflammatory cytokines, particularly the overexpression of tumor necrosis factor-alpha (TNF-α), which drives mucosal inflammation and tissue damage (52–55).

High levels of TNF-α have been detected both locally in intestinal tissues and systemically in the serum of patients with Crohn's disease and ulcerative colitis (52,55). This cytokine regulates multiple signaling pathways involved in immune activation and chronic inflammation (5,56), making it a central therapeutic target. As a result, biological therapies using monoclonal antibodies (mAbs) directed against TNF-α have been developed to modulate the immune response and promote mucosal healing (26,57). These anti-TNF-α agents, including infliximab (a chimeric mAb) and adalimumab (a fully human mAb), are approved for clinical use, with infliximab administered intravenously and adalimumab subcutaneously (58).

Treatment selection is influenced by patient-specific factors such as disease severity, pharmacoeconomic considerations, and administration route preferences (58,59). Despite their proven efficacy, approximately 20–40% of patients exhibit primary non-response or lose responsiveness over time (4,26). Therefore, identifying reliable biomarkers to predict and monitor therapeutic outcomes remains a clinical priority (60,61). While serum levels of anti-TNF-α agents correlate with clinical outcomes and are currently used to guide dosing, they do not fully account for interpatient variability in treatment response (57). Indeed, 10–20% of patients with therapeutic drug levels still fail to respond (56,61), highlighting the need to better understand drug distribution at the site of action.

The extent of monoclonal antibody accumulation in the intestinal mucosa, particularly the colon, remains poorly characterized. Although it is influenced by local TNF-α expression (54,60) other factors such as drug bioavailability, molecular diffusion across tissue barriers, and route of administration also play critical roles (62). Notably, pharmacokinetics differs substantially between intravenous and subcutaneous delivery, especially in patients with altered physiology such as obesity.

In this context, non-invasive molecular imaging techniques, notably positron emission tomography (PET), offer valuable insights into drug pharmacokinetics and tissue distribution. ImmunoPET, which utilizes radiolabeled antibodies, enables real-time, whole-body tracking of therapeutic mAbs and has shown substantial promise in oncology for both preclinical and clinical applications (63). However, its use in inflammatory diseases is still emerging, with recent studies exploring its utility in uveitis (64), arthritis (65), and colitis (66).

The objective of this study was to evaluate and compare the *in vivo* biodistribution and pharmacokinetics of Adalimumab following subcutaneous and intravenous administration in a murine model of IBD using [^{89}Zr]Zr-DFO- Adalimumab ImmunoPET. This approach enables visualization and quantification of antibody delivery to the colon, offering novel insights into the relationship between administration route, systemic pharmacokinetics, and target site engagement.

2.SPECIFIC METHODS

2.1 ANIMALS

A total of 22 female C57BL/6 mice, aged 8 weeks, were obtained from the animal facility of the Centre for Experimental Biomedicine of Galicia (CEBEGA), University of Santiago de Compostela (Spain). Animals were housed in groups of 3 to 4 per cage under standardized environmental conditions, including controlled temperature (22 ± 1 °C), relative humidity (60 ± 5%), and a 12-hour light/dark cycle. Mice had unrestricted access to food and water (ad libitum) throughout the study period.

All experimental procedures were carried out in compliance with European and national regulations for the ethical use of animals in research (86/609/CEE, 2003/65/CE, 2010/63/EU and RD53/2013), as well as the ARRIVE guidelines. The study protocol was reviewed and approved by the Animal Ethics Committee of the University of Santiago de Compostela (code 15012/2022/013).

2.2 INFLAMMATORY BOWEL DISEASE MODEL

The animals were randomly assigned to two experimental groups: IBD group (n = 13) and a healthy control group (n = 9). Experimental colitis was induced in the IBD group by administering 2.5% dextran sulfate sodium (DSS; Batch: DB001-44, Tdb Labs, Uppsala, Sweden) in the drinking water for five consecutive days. Fresh DSS solutions were prepared daily to prevent aggregate formation, and bottles were wrapped in aluminium foil to minimize light-induced degradation. Following DSS administration, animals were provided with regular drinking water for an additional five days. Body weight was monitored daily throughout the induction period to track disease progression, following established protocols (67,68).

2.3 [^{18}F]FDG PET/CT IMAGING

To confirm IBD model induction, in addition to weight, all animals underwent [^{18}F]FDG PET/CT imaging. Mice were fasted overnight prior to scanning and housed on grid floors to prevent coprophagia. Anesthesia was induced in a chamber with 3% isoflurane in oxygen and maintained via face mask using 2–2.5% isoflurane during the procedure. Each animal received an intravenous injection of [^{18}F]FDG (5.24 ± 1.15 MBq) via the tail vein. Following injection, mice were allowed to recover briefly under resting conditions. Twenty minutes post-injection, 0.2 mL of CT contrast agent (Iopromide Ultravist® 300 mg/mL; Barcelona, Spain) was administered rectally using a polyethylene catheter (PE10; 0.28 mm ID, 0.61 mm OD), inserted approximately 3 cm into the rectum and connected to an insulin syringe.

Subsequently, static PET/CT imaging was performed using an Albira PET/CT preclinical scanner (Bruker Biospin Corp., Billerica, MA). PET scans were acquired over 10 minutes to capture whole-body distribution, followed by a 10-minute CT acquisition (35 kV, 200 µA, 250 projections per bed, focused on the abdominal region). Upon completion of imaging, animals were returned to their home cages with ad libitum access to food and water.

2.4 [^{89}Zr] Zr-DFO-Adalimumab PET/CT imaging

Our cohort (n = 22) was divided into four subgroups: subcutaneous (SC) control (n = 6), SC IBD (n = 8), intravenous (IV) control (n = 3), and IV IBD (n = 5). Mice were anesthetized in a chamber with 3% isoflurane in oxygen until unconscious and maintained under 2% isoflurane for radiotracer administration. SC groups received [^{89}Zr]Zr-DFO-adalimumab (2.93 ± 0.92 MBq, 60 µg) subcutaneously in the loose neck skin, while IV groups were injected intravenously via the tail vein with [^{89}Zr]Zr-DFO-adalimumab (3.6 ± 0.4 MBq, 60 µg). Before each scan, a 10 µL blood sample was collected from the tail vein of each animal, and 0.2 mL of CT contrast agent was administered rectally as previously described.

Static PET/CT imaging (following the protocol detailed in general methods, section 2.3) was performed at 24, 48, 72, 96, and 168 hours post-injection (p.i.) for the SC groups, and at 0, 6, 24, 48, 72, and 168 hours p.i. for the IV groups. At the end of the imaging schedule, mice were deeply anesthetized and perfused transcardially with phosphate-buffered saline (PBS) followed by 10% formalin, then euthanized by cardiac excision. Colon and liver tissues were harvested from a subset of 13 animals (6 controls: 3 SC and 3 IV; 7 IBD: 3 SC and 4 IV) for *ex vivo* radioactivity quantification using a gamma counter. Colonic tissues were subsequently fixed in formalin for 24 hours, transferred to PBS, and stored for later histological and immunohistochemical analyses.

2.5 Image analysis

PET image analysis was performed using PMOD v4.2 software (PMOD Technologies, Zürich, Switzerland). Initially, PET and CT images were accurately fused to ensure precise localization and consistency across all measurements. The mean radioactivity concentration was determined for different manual volumes-of-interest (VOIs) located in the area under analysis: colon (7 x 4 x 5 mm) and liver (6 x 6 x 6 mm). The mean radioactivity concentration was calculated for different manually volumes-of-interest (VOIs), corrected for decay and expressed in terms of SUV as follows:

$$SUV = \frac{Mean\ radioactivity\ concentration\ in\ VOI\ (kBq/ml)}{Injected\ dose\ (kBq)} * body\ weight\ (g)$$

2.6 Blood pharmacokinetic analysis

Pharmacokinetic analyses of blood concentration data were conducted using both noncompartmental and compartmental approaches. Noncompartmental parameters included the area under the concentration-time curve from time zero to infinity ($AUC_{0–\infty}$) and the mean residence time (MRT) (69). Compartmental modeling was performed using nonlinear regression analysis in GraphPad Prism 8 (version 8.2.1; GraphPad Software, San Diego, CA, USA). Concentration–time data (Figure 8) were fitted to both one- and two-compartment models. The standard error of the regression (Sy.x) and the root mean square error (RMSE) were calculated to evaluate the goodness of fit.

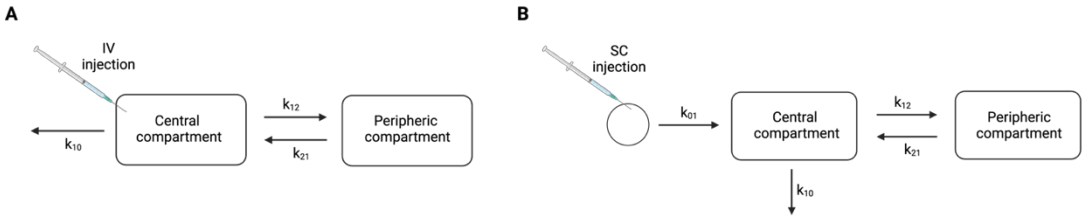

Figure 8: Compartmental analysis of [^{89}Zr]Zr-DFO-adalimumab in blood. (A) Intravenous two-compartment model. (B) Subcutaneous two-compartment model (k_{01} represent the first-order fractional rate constant for absorption, k_{12} and k_{21} the first-order fractional rate constants of distribution between plasma and tissues (k_{12}) and the redistribution between tissues and plasma (k_{21}). k_{10} the first-order fractional rate constant for elimination from plasma compartment. α and ß are called "hybrid constants" that represent the first-order constant process in the distribution phase or alfa (α) phase, and the elimination phase or the beta (ß) phase). Created with BioRender.com

2.7 IMMUNOHISTOCHEMISTRY

Immunohistochemistry was conducted using a mouse monoclonal anti-TNF-α antibody (NeoBiotechnologies®, Union City, USA) to assess TNF-α expression levels in colon tissue samples. All samples were evaluated blindly by a gastrointestinal pathologist using a Leica® microscope (Leica DM2000 LED, Barcelona, Spain). Histological disease activity was graded according to the Nancy histological index, which classifies inflammation into five levels: grade 4 indicates ulceration with inflamed granulation tissue; grade 3 is defined by the absence of ulceration but the presence of multiple clusters of neutrophils in the lamina propria and/or epithelium, clearly visible under the microscope; grade 2 is characterized by a few or rare neutrophils that are difficult to detect; grade 1 denotes an absence of neutrophils but the presence of lymphocytes and/or eosinophils in the lamina propria; and grade 0 indicates no increase in chronic inflammatory cells or any histologically significant disease (70). Additionally, TNF-α expression levels in the colon were semi-quantitatively assessed based on staining intensity and categorized as weak (*), *intermediate (**), or strong (***).

3.RESULTS

3.1 CONJUGATION AND RADIOLABELING OF [^{89}ZR]ZR-DFO-ADALIMUMAB

The anti-TNF-α monoclonal antibody (mAb) was successfully conjugated with DFO as confirmed by radio-HPLC analysis. No dimer formation was detected in the chromatogram following conjugation. ELISA results showed that 74.9% of the conjugated Anti-TNF-α retained its binding specificity to the TNF-α receptor, indicating preserved biological activity. The theoretical specific activity was 74 MBq/mg, consistent across all mice. Following radiolabelling, the radiochemical purity (RCP) was 90.72%, which increased to 97.74% after ultrafiltration.

3.2 INFLAMMATORY BOWEL DISEASE MODEL

3.2.1. Weight evolution

Relative changes in body weight were calculated as percentages of the initial weight (Figure 9). From day 0 to day 5, no significant differences were observed between the IBD and control groups. However, from day 6 to day 12, IBD animals exhibited a significant reduction

in body weight compared to controls, confirming successful model induction. Notably, both IBD and control groups showed a temporary weight decrease on day 10, attributed to fasting prior to the [^{18}F]FDG PET/CT scan.

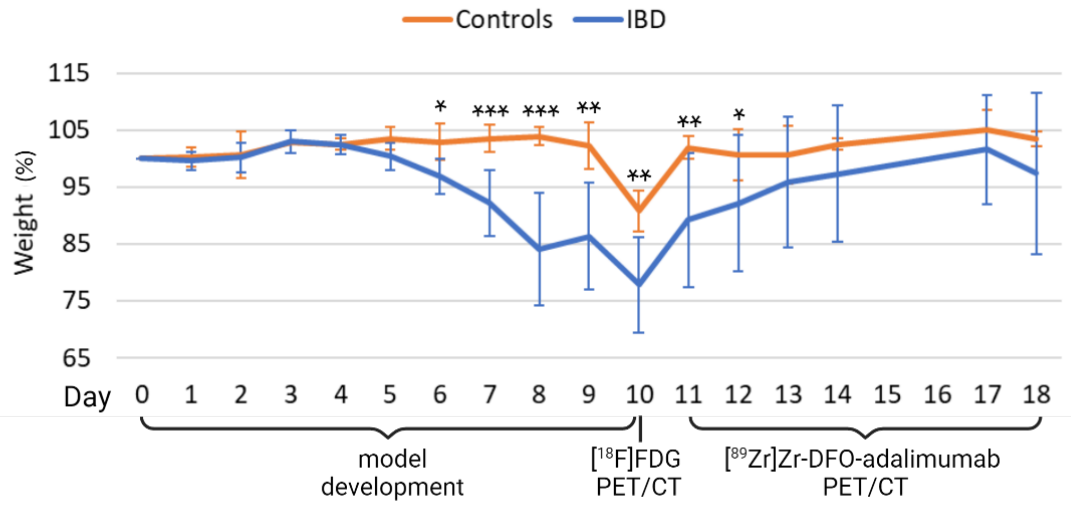

Figure 9: Percentage of relative weight changes (%) from day 0 to 18 of animals in control group (orange line) and in IBD group (blue line). Values are expressed as mean ± SE. *, p < 0.05; **, p < 0.01 ***, p < 0.001.

3.2.2 [^{18}F]FDG PET/CT

Average SUV from the control group was 0.60 ± 0.09, establishing a threshold for model induction at 0.78 (mean SUV plus two standard deviations). One animal from the IBD group (IBD13) exhibited an SUV below this threshold (SUV = 0.71) and was therefore excluded from further analysis. As shown in Figure 10A, the remaining IBD animals displayed SUV values exceeding the threshold. Representative SUV images from each group are presented in Figure 10B.

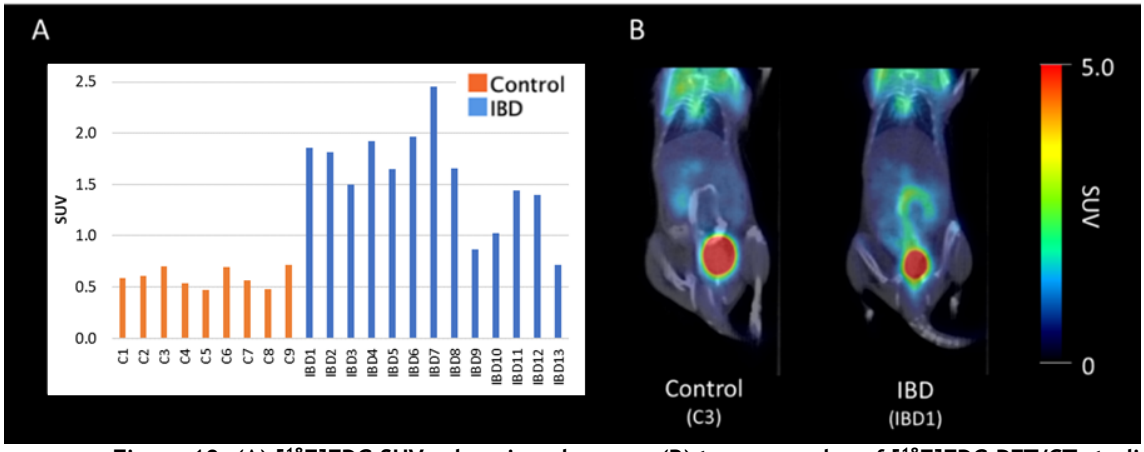

Figure 10: (A) [^{18}F]FDG SUV values in colon area (B) two examples of [^{18}F]FDG PET/CT studies expressed as SUV, control (C3) and IBD (IBD1).

3.2.3 Histopathological and immunohistochemistry evaluation

All IBD animals exhibited a Nancy histological grade of 4, while control mice showed a grade of 0, thereby confirming successful induction of the IBD model (Figure 11B).

Representative histological images are presented in Figure 11A, with the right panel depicting a normal colonic wall (grade 0) and the left panel showing mucosal ulceration (grade 4). Immunohistochemical analysis of TNF-α expression revealed intermediate staining in three IBD animals, while the remainder displayed weak staining, comparable to that observed in the control group.

A

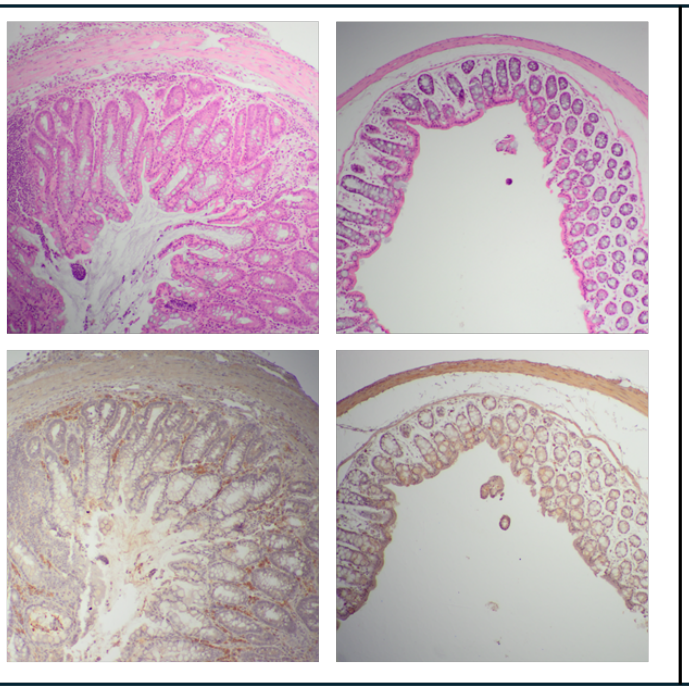

B

IV		
ID	Nancy Grade	TNF
C1	0	*
C2	0	*
C3	0	*
IBD1	4	**
IBD2	4	**
IBD3	4	*
SC		
ID	Nancy Grade	TNF
C7	0	*
C8	0	*
C9	0	*
IBD10	4	**
IBD11	4	*
IBD12	4	*

Figure 11: (A) Nancy grade and immunohistochemistry values. Above from SC injection and below from IV injection. (B) Representative hematoxylin-eosin staining of colons wall tissue (up). Immunohistochemistry TNF staining of colons wall tissue (bottom). Left, normal colon tissue with Nancy grade 0 and TNF staining * (C7), right, IBD colon tissue with Nancy grade 4 and TNF staining * (IBD12).

3.3 ADALIMUMAB BLOOD PHARMACOKINETICS

[^{89}Zr]Zr-DFO-adalimumab exhibited significantly faster blood clearance in IBD mice compared to controls, irrespective of the administration route (Figure 12). Additionally, IV administration resulted in a more rapid decline in blood radioactivity levels compared to SC administration in both experimental groups. Following IV administration, the blood standardized uptake value (SUV_{blood}) in the control group decreased from 6.35 ± 0.41 at 0 hours post-injection (p.i.) to 0.26 ± 0.13 at 168 hours p.i., while in the IBD group, it dropped from 5.73 ± 0.34 to 0.02 ± 0.01 over the same period. Statistically significant differences ($p \leq 0.001$) in SUV_{blood} between control and IBD groups were observed at 6, 24, 48, and 72 hours, but not at 0 or 168 hours p.i.

In the SC-administered cohorts, the SUV_{blood} decreased from 3.56 ± 0.30 at 24 hours to 1.08 ± 0.11 at 168 hours in controls, and from 2.11 ± 0.17 to 0.06 ± 0.02 in IBD mice. SUV_{blood} values in the control group remained significantly higher than those in the IBD group at all measured time points (24, 48, 72, 96, and 168 hours; $p < 0.001$).

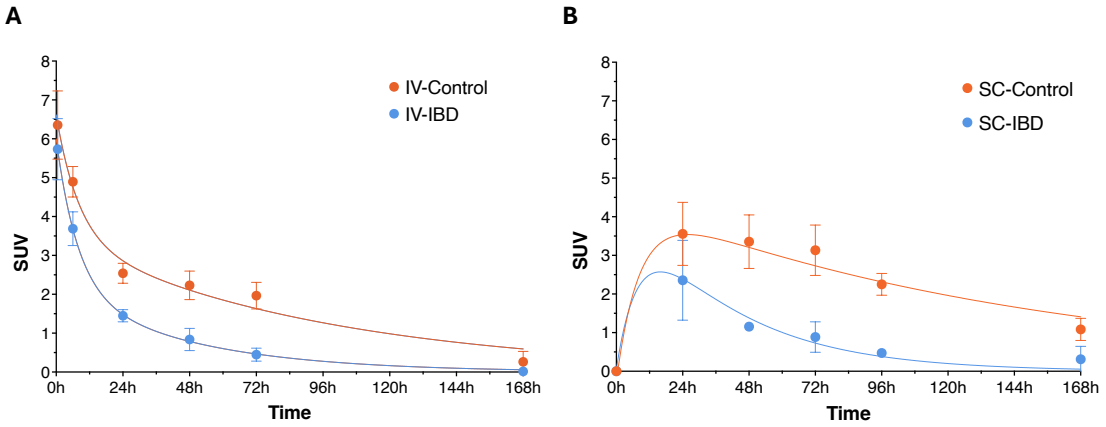

Figure 12: Blood pharmacokinetic profiles (blood SUV versus time) after injection of [^{89}Zr]Zr-DFO-Anti-TNF-α in (A) IV group and (B) SC group. Control group is shown in orange and the IBD group in blue. Values are expressed as means ± SD. Lines correspond to the fitted to the two-compartment model equations.

Table 3 presents the results from both noncompartmental (area under the curve: AUC_0^∞; and mean residence time: MRT) and compartmental pharmacokinetic analyses. The blood pharmacokinetic profiles were best described by a two-compartment model for both IV and SC administration routes, as indicated by lower root mean squared error (RMSE) and standard error of the estimate (Sy.x). The AUC_0^∞ values in IBD animals were approximately 50% lower than those in control animals for both administration routes, suggesting a significantly faster systemic clearance of [^{89}Zr]Zr-DFO-adalimumab in the IBD condition. Additionally, within the IBD group, SC administration resulted in significantly higher AUC_0^∞ values compared to IV administration, reflecting slower absorption kinetics.

MRT was also markedly reduced in the IBD group compared to controls, further supporting an increased clearance rate. For IV administration, pharmacokinetic profiles demonstrated a rapid alpha distribution phase within the first 24 hours, followed by a slower beta elimination phase, consistent across both groups. In SC administration, an initial absorption phase was evident, characterized by k_{01} values of 0.09 ± 0.0443 h^{-1} in SC-IBD animals and 0.02 ± 0.0006 h^{-1} in SC-controls, indicating the rate of systemic diffusion of adalimumab from the injection site.

Table 3: Non-compartmental and two-compartmental pharmacokinetic parameters obtained from the evolution of blood [^{89}Zr]Zr-DFO-adalimumab concentration versus time following intravenous (IV) and subcutaneous (SC) administration in the IBD and control groups.

	IV-IBD		IV-Control		SC-IBD		SC-Control	
	Mean	SE	Mean	SE	Mean	SE	Mean	SE
α (h^{-1})	0.13	0.0398	0.12	0.0084	0.13	0.0655	0.12	0.0084
β (h^{-1})	0.02	0.0027	0.01	0.0011	0.02	0.0105	0.02	0.0005
k_{12} (h^{-1})	0.05	0.0192	0.04	0.0052	0.05	0.0232	0.04	0.0052
k_{21} (h^{-1})	0.06	0.0238	0.07	0.0052	0.06	0.0290	0.07	0.0052
k_{10} (h^{-1})	0.04	0.0032	0.02	0.0011	0.04	0.0217	0.02	0.0011
k_{01} (h^{-1})	-	-	-	-	0.09	0.0443	0.02	0.0006
$T_{1/2\alpha}$ (h)	7.23	2.2085	5.98	0.4450	5.98	2.9907	5.80	0.5196
$T_{1/2\beta}$ (h)	44.56	6.5788	69.97	8.4824	36.56	18.2817	40.46	1.2405
R^2	0.9981	0.0010	0.9782	0.0097	0.99	0.4957	0.99	0.0128
Sy.x	0.1328	0.0303	0.9455	0.0242	0.16	0.0796	0.24	0.1572
RMSE	0.0840	0.0192	0.4638	0.1906	0.07	0.0356	0.11	0.0005
AUC_0^∞ (mg ml^{-1} h^{-1})	139.96	7.64	332.16	13.28	213.56	106.78	585.90	120.94
MRT (h)	29.01	1.68	52.96	5.87	77.35	38.68	88.77	6.97

3.4 ADALIMUMAB PET TISSUE DISTRIBUTION

Anti-TNF-α PET images in terms of SUV was employed to evaluate the whole-body biodistribution of [^{89}Zr]Zr-DFO-adalimumab (Figure 13). At early time points (6 h and 24 h post-injection), both IBD and control animals, regardless of administration route (IV or SC), exhibited high, diffuse tracer uptake throughout the body, indicative of elevated radiotracer concentrations within the vascular compartment. This widespread signal markedly declined by 72 h in IBD animals across both administration routes, consistent with the previously described accelerated blood clearance.

Colon localization is highlighted with white arrows in the images, where the highest signal intensity was observed at 6 h post-injection for IV administration and at 24 h for SC administration in IBD mice. By 168 h, residual uptake seen in the region indicated by the arrow predominantly corresponds to hepatic accumulation. Notably, IBD animals demonstrated

minimal to no remaining systemic activity at this time point, while low residual uptake persisted in control animals.

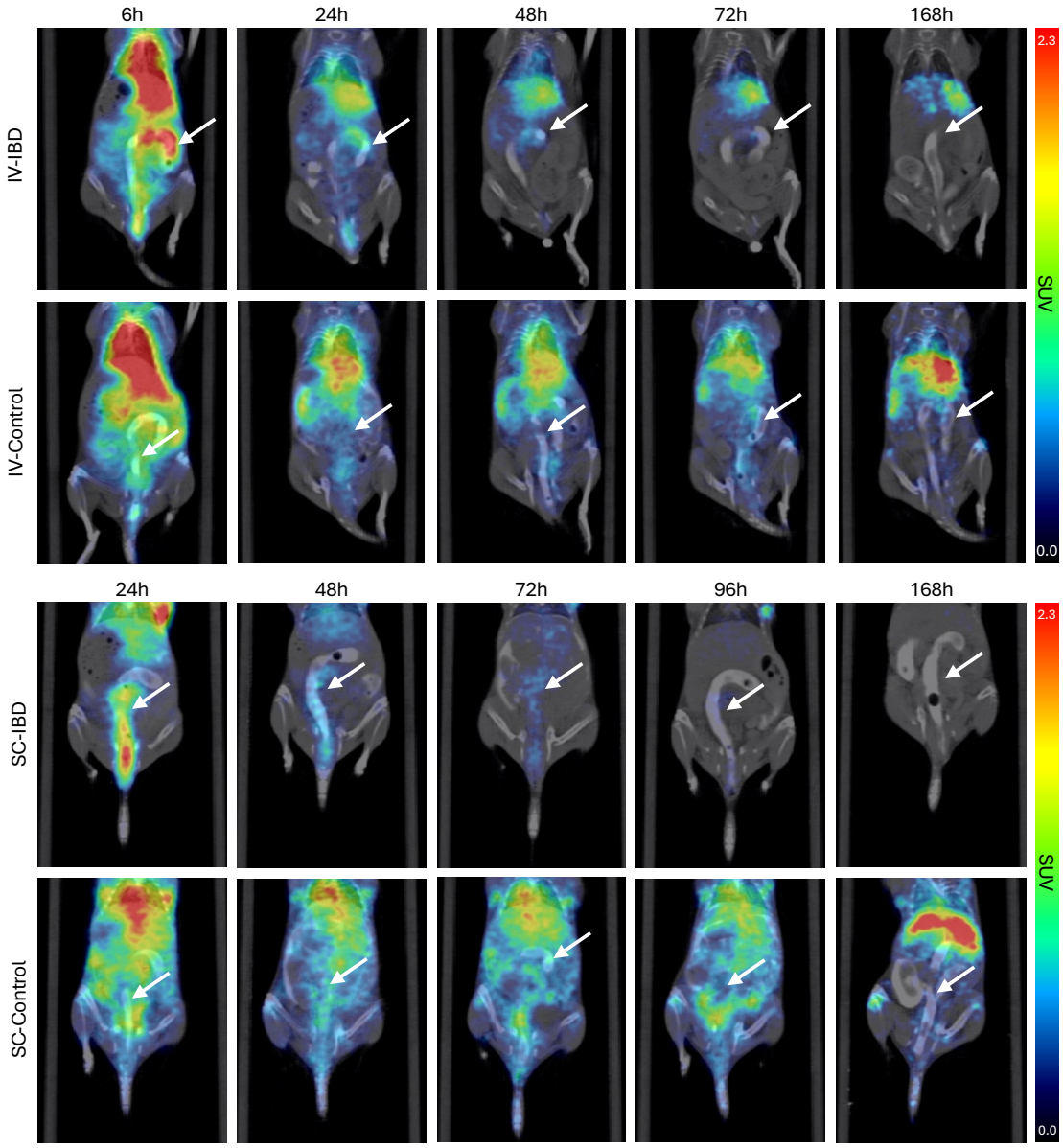

Figure 13: Fused PET/CT images displayed in coronal plane showing mice body from different groups at different time points.

Figure 14A and Figure 14B show the temporal evolution of colon SUV values for both IBD and control groups across SC and IV administration routes. In the SC group, IBD animals exhibited a peak colon SUV at 24 hours post-injection (1.49 ± 0.27), significantly higher than that of controls (0.89 ± 0.05, $p < 0.05$). By 168 hours, the colon SUV in IBD animals declined markedly to 0.13 ± 0.03, whereas control values remained relatively unchanged over time. Similarly, following IV administration, IBD animals showed a peak colon SUV at 6 hours (2.11 ± 0.18), which decreased to 0.18 ± 0.05 at 168 hours. In contrast, control animals displayed stable colon SUV values across all time points. Statistically significant differences between IBD and control groups were observed only at 24 hours post-SC injection ($p < 0.05$) and at 6 hours post-IV injection ($p < 0.001$).

Figure 14C and Figure 14D illustrate liver SUV kinetics over time for both administration routes. In all groups, liver SUV peaked at the earliest measured time point and gradually declined thereafter, with the rate of decline varying between groups. Liver SUV values were consistently higher following IV administration compared to SC, for both IBD and control animals. Within each administration route, liver uptake was significantly greater in control animals relative to IBD counterparts. Notably, an increase in liver SUV was observed at the final time point (168 h) across all groups, with a modest rise in IBD animals and a more pronounced increase in control animals.

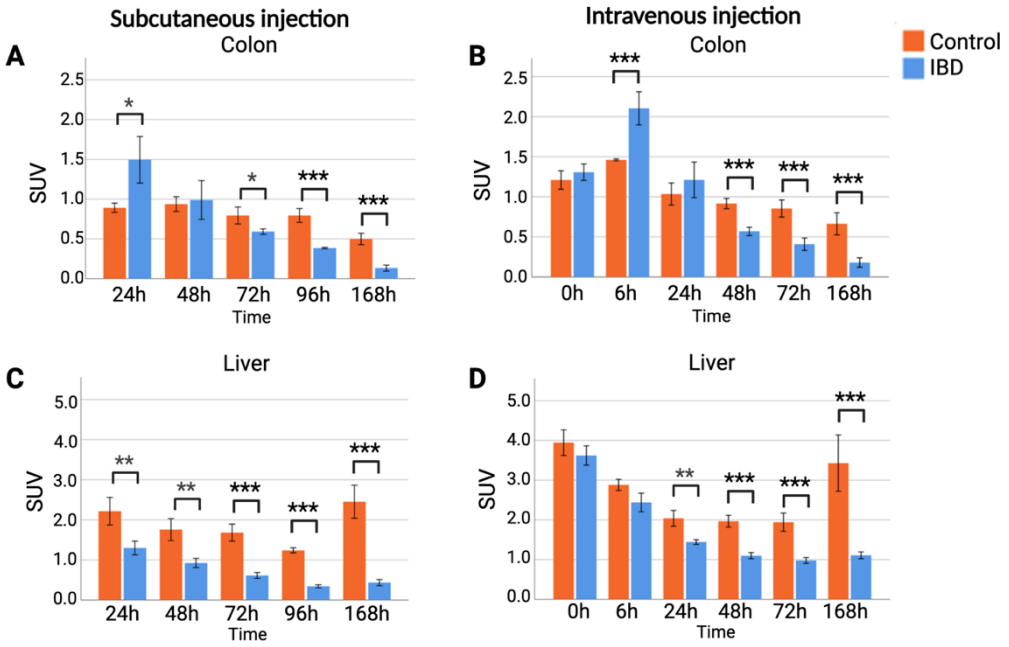

Figure 14: Colon SUV values of control group (orange) and IBD group (blue) over time after (A) subcutaneous injection or (B) intravenous injection. Liver SUV values of control group (orange) and IBD group (blue) over time after (C) subcutaneous injection or (D) intravenous injection. Values are expressed as mean ± SE. *, p < 0.05; **, p < 0.01 ***, p < 0.001.

3.5 EX VIVO ANALYSIS

Ex vivo quantitative analysis at 168 hours post-injection (Figure 15) revealed significantly higher radioactivity levels in the livers of control animals in both administration groups (IV and SC), consistent with liver SUV values observed in PET imaging. These findings suggest prolonged hepatic retention of [^{89}Zr]Zr-DFO-adalimumab in control animals compared to those with IBD, and further indicate that the PET-derived liver signal predominantly reflects tissue-associated radiotracer rather than residual blood pool activity. In contrast, radioactivity levels in the colon were minimal across all groups, aligning with the low colon SUV values observed at 168 hours in PET images. However, no statistically significant differences in colon radioactivity were detected between groups. This suggests that the PET signal at this late time point may still partially reflect the vascular component of the colon, potentially accounting for the relatively higher colon uptake observed in control animals compared to IBD counterparts.

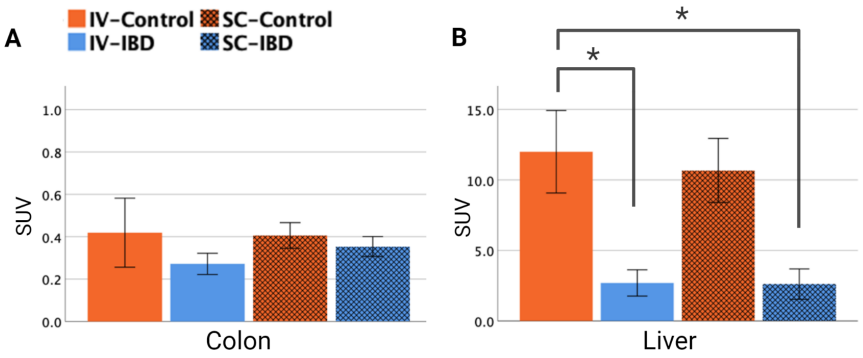

Figure 15: SUV values of *ex vivo* measurements of (A) colon tissue and (B) liver after 168h of [^{89}Zr]Zr-DFO-adalimumab injection. IV-control group is represented in orange color, IV-IBD in blue, SC-control in orange dotted pattern and SC-IBD group in blue dotted pattern. Values are expressed as mean ± SE. *, p < 0.05; ***, p < 0.001.

4.DISCUSSION

The optimization of anti-TNF-α therapies for inflammatory bowel disease (IBD) has traditionally centred on monitoring serum antibody concentrations over time. However, it is increasingly evident that therapeutic efficacy is not solely dependent on systemic antibody levels, but also on the extent to which the therapeutic antibody reaches the target tissue, i.e. the colon. Several studies have associated clinical outcomes with local TNF-α expression in colonic tissue, suggesting its potential as a predictive biomarker for treatment response (54,57,61). In the present study, we demonstrate that TNF-α expression alone may not fully account for therapeutic outcomes. Instead, we propose that the delivery of anti-TNF-α mAbs, such as adalimumab, to the colon is more strongly influenced by pharmacokinetic behavior, biodistribution, and overall bioavailability parameters that have also been shown to affect the tissue penetration of other mAbs administered via subcutaneous or intravenous routes (62).

Accordingly, our work focused on elucidating the mechanisms by which Anti-TNF-α transverses biological barriers from the point of administration to its eventual accumulation in the colon, as well as characterizing its elimination kinetics. Within this framework, the route of administration emerges as a critical determinant of tissue targeting, independent of TNF-α expression levels in the colon. This perspective is particularly important given that elevated TNF-α expression can occur in multiple anatomical locations beyond the colon, potentially modulating antibody distribution and bioavailability at the disease site.

To address this question and delineate the biodistribution pathway of Anti-TNF-α following different routes of administration, we employed radiolabelling of the monoclonal antibody with zirconium-89 ([^{89}Zr]Zr-DFO-adalimumab), coupled with PET imaging. This strategy was based on previously established methodologies developed in our group (64,71–73).

Firstly, our findings in terms of blood pharmacokinetic data corroborated earlier findings, confirming a slower systemic absorption of adalimumab following SC administration compared to IV delivery (74). Furthermore, we observed an accelerated clearance of the radiolabelled antibody in IBD models relative to healthy controls. This enhanced elimination is likely attributable to elevated levels of TNF-α in both the systemic circulation and colonic tissue of

IBD animals, which may promote the formation of antigen–antibody complexes, thereby facilitating more rapid clearance from the bloodstream (75,76).

Our findings on the whole-body distribution of adalimumab provide critical insight into both its accumulation in the colon and its subsequent elimination profile. PET imaging revealed distinct qualitative differences in radiotracer uptake between groups. In IBD models, adalimumab accumulation was clearly localized within the colonic region, whereas in control animals, uptake appeared more diffusely distributed across surrounding tissues. Additionally, adalimumab exhibited a more rapid systemic distribution in IBD animals compared to controls. This accelerated clearance is likely attributable to the earlier formation of antigen–antibody complexes in IBD models, followed by immune-mediated clearance mechanisms such as NK cell activity, endocytosis, and lysosomal degradation (76,77). Conversely, in the absence of specific antigen targets, as in the control group, adalimumab persists longer in circulation due to its high molecular weight (78) and protection from degradation through neonatal Fc receptor (FcRn)-mediated recycling (75).

These different pharmacokinetics significantly impact adalimumab uptake in the colon, as visualized by PET. IBD animals exhibited higher early colonic uptake compared to controls, particularly those with elevated TNF-α expression (IBD1, IBD2, IBD10), showing SUV values of 2.01 ± 0.59, in contrast to lower TNF-α expressers (IBD3, IBD11, IBD12), which presented SUV values of 1.16 ± 0.65 (not statistically significant; $p = 0.886$). These results suggest that increased TNF-α expression in the colon enhances both local delivery and binding of adalimumab. At later time points, however, control animals displayed higher colonic SUV values than IBD models. This reversal is likely due to the presence of circulating radiolabelled adalimumab in the vascular compartment of the colon, as higher blood concentrations were maintained in controls. This was confirmed by *ex-vivo* analysis, where adalimumab radioactivity coming from the blood can be removed by perfusing colon samples, and consequently the differences IBD and control disappear.

Regarding the route of administration, our findings in the intravenous (IV) group are partially aligned with those reported before (66) where the biodistribution of infliximab was studied employing PET imaging. Their study demonstrated increased colonic uptake in inflammatory bowel disease (IBD) models relative to controls, but did not report a subsequent reduction in colonic signal at later time points. It is important to note that their investigation focused on infliximab rather than adalimumab and was limited to a pharmacokinetic evaluation up to 72 hours post-injection (p.i.), whereas our study extended the observation period to 7 days p.i. Additionally, another study examined the pharmacokinetics and biodistribution of infliximab using SPECT in human subjects (79). However, the short half-life of the radiotracer used (^{99m}Tc, $T_{1/2} = 6$ hours) constrained the duration of imaging, thereby limiting the ability to detect delayed colonic accumulation and complicating direct comparisons with our extended longitudinal analysis.

Furthermore, our PET-based pharmacokinetic and biodistribution analysis allowed for the evaluation of hepatic involvement in adalimumab clearance. The liver is known to play a central role in the catabolism of therapeutic antibodies, progressively degrading them into smaller peptides and amino acids that may be reutilized for protein synthesis (80). This mechanism likely accounts for the elevated hepatic signal observed in PET imaging. Following IV administration, hepatic uptake of adalimumab was initially comparable between IBD models and control animals. However, at later time points, liver associated radioactivity was higher in controls relative to IBD models. A similar trend was noted with the SC administration route, though in this case, differences in hepatic uptake were apparent from the earliest measured time

points. Across all SC time points, controls exhibited consistently higher hepatic adalimumab accumulation than IBD models. These findings suggest that hepatic clearance constitutes a major route of adalimumab elimination. Nonetheless, the formation and distribution of adalimumab-immune complexes may also involve other organs, including the spleen, kidneys, and peripheral tissues.

Finally, it is important to emphasize the rigorous validation of the IBD models through multiple complementary assessments to ensure effective disease induction. In the first instance, [^{18}F]FDG PET imaging was employed to evaluate colonic inflammation, following the protocol previously described (81). Notably, no statistically significant correlation was observed between colonic uptake values of [^{18}F]FDG and adalimumab ($r^2 = 0.29$, $p < 0.05$). Although a weak trend was present, the absence of a strong correlation is expected, given that these tracers reflect distinct biological processes. [^{18}F]FDG is an indirect marker of inflammation based on glucose metabolism, whereas adalimumab uptake is more likely associated with local TNF-α expression, as previously discussed. This imaging analysis was further supported by monitoring weight loss in individual animals, a less specific but commonly used indicator of disease severity. *Ex vivo* evaluations corroborated the persistence of colonic pathology at 168 hours p.i., as evidenced by histological examination. These results were further substantiated by immunohistochemical analysis, which demonstrated elevated TNF-α expression in several IBD animals compared to controls, along with noticeable inter-individual variability within the IBD group. While this heterogeneity in TNF-α levels could be viewed as a limitation due to non-uniform model induction, it was leveraged in our study to explore whether the extent of adalimumab accumulation in the colon is influenced by local TNF-α expression levels.

This study is subject to several limitations. First, the experimental design did not allow for the characterization of adalimumab pharmacokinetics prior to 24 hours post-injection following SC administration. Although a delayed absorption phase was initially anticipated, the observed kinetics were faster than expected, precluding accurate determination of the time point at which peak colonic uptake occurred.

Another limitation concerns the interpretation of SUVs in the colon derived from PET imaging. These values reflect the total radiolabelled adalimumab signal, encompassing both antigen-bound and unbound fractions within the tissue, as well as circulating drug within the local vasculature (i.e., capillaries and veins of the colon). This may introduce bias, particularly in comparisons involving low colonic SUV values and differing systemic concentrations of adalimumab. Addressing this issue would require advanced kinetic modeling of dynamic PET data to deconvolve vascular and tissue compartments, a level of analysis beyond the scope of the current study. Such an approach would necessitate the identification and validation of an appropriate compartmental model tailored to our dataset.

It is also important to note that our investigation employed tracer doses of radiolabelled adalimumab, in accordance with the tracer principle required for PET imaging (82). This methodological constraint enabled the *in vivo* detection of target engagement and provided insights into differential elimination pathways, notably hepatic clearance in control animals versus potential immune complex-mediated elimination in IBD models. However, the pharmacokinetic profiles observed in this study do not reflect those expected at therapeutic dosing levels. Future studies aiming to assess therapeutic efficacy and dose-dependent distribution could integrate tracer quantities of radiolabelled adalimumab with unlabeled adalimumab administered at clinically relevant doses.

To the best of our knowledge, this study represents the first investigation to comprehensively evaluate the biodistribution and pharmacokinetics of Anti-TNF-α using PET

imaging over an extended timeframe of up to 7 days post-injection. This approach enables precise, longitudinal tracking of adalimumab distribution, providing valuable insights into its pharmacokinetic behavior and tissue-specific uptake. The methodology presented here has potential applications in optimizing adalimumab therapy, particularly with regard to administration route, dosing strategies, and injection frequency. Moreover, it may serve as a valuable tool for evaluating alternative administration routes or novel drug delivery systems, such as rectally administered anti-TNF-α nanoparticles, as recently proposed (83). Importantly, the translational relevance of this methodology is underscored by its compatibility with clinical practice, given that PET imaging with radiolabelled monoclonal antibodies is already being implemented in ongoing clinical trials.

5.CONCLUSION

Our work studied for the first time the *in vivo* biodistribution of adalimumab after SC and IV administration in IBD models and controls. Our results demonstrated that adalimumab is cleared from the blood of IBD models faster than in controls, either after IV or SC administration. Despite this faster blood clearance, adalimumab reached higher colon concentration in IBD models than in controls, both after IV and SC administration. Although both administration routes showed a peak of maximum colon concentration at early time points, significant differences were found between administration routes, providing an earlier and higher maximum concentration peak of adalimumab after IV (SUV 6h p.i. IBD-IV = 2.11 ± 0.18) compared to SC (SUV 24h p.i. IBD-SC = 1.49 ± 0.27).

Altogether, our findings demonstrated the amount of adalimumabreaching the colon over time is strongly affected by the route of administration and by the expression of TNF-α, both locally in the colon and systemic levels.

CHAPTER II

PET IMAGING REVEALS LIMITED OCULAR PENETRATION OF ADALIMUMAB IN SYSTEMIC UVEITIS

ABSTRACT

The optimisation of anti-TNF-α therapies for non-infectious uveitis has traditionally focused on clinical signs, without direct assessment of monoclonal antibody (mAb) penetration into the eye. In this study, zirconium-89 radiolabelling combined with positron emission tomography (PET) imaging was employed to evaluate the biodistribution of adalimumab following subcutaneous (SC) and intravitreal (IVT) administration. Results demonstrated greater antibody retention in inflamed eyes after IVT administration, whereas SC delivery resulted in reduced ocular uptake in uveitic animals. Pro-inflammatory cytokine expression (IL-6, IL-8, MIP-1α, TNF-α) was significantly elevated in uveitis-induced animals, confirming a strong inflammatory response triggered by LPS (lipopolysaccharide). Furthermore, adalimumab levels in the blood were lower in diseased animals, suggesting tissue retention. Systemic inflammation in uveitis may lead to antibody sequestration in organs such as the liver or spleen, thereby limiting SC-derived ocular bioavailability. This study highlights the potential limitations of SC administration and suggests that IVT delivery may offer superior therapeutic outcomes in patients unresponsive to SC adalimumab treatment.

GRAPHICAL ABSTRACT

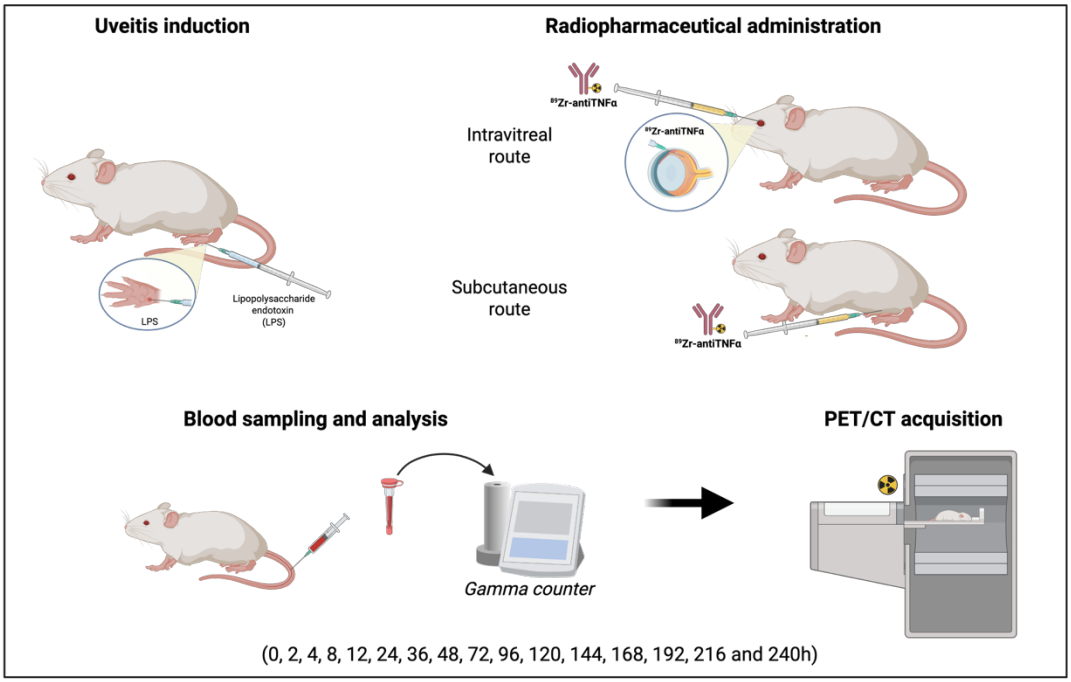

Figure 16: Graphical abstract illustrating the experimental design of the administration routes and the PET and blood samples time points. Created with BioRender.com

1.INTRODUCTION

Non-infectious uveitis encompasses a heterogeneous group of intraocular inflammatory conditions primarily affecting the uveal tract, which includes the iris, ciliary body, and choroid. It can lead to visual impairment and blindness if left untreated. Although its precise etiology remains incompletely understood, there is growing evidence that pro-inflammatory cytokines, particularly TNF-α, play a central role in disease pathogenesis (84,85). In individuals with active uveitis, TNF-α levels in serum and aqueous humour are elevated and correlate with disease activity and severity (86).

Non-infectious uveitis accounts for the most uveitis cases (67–90%) in the developed world (87). A significant proportion of these cases, up to 40%, are associated with underlying systemic autoimmune disorders, which represent an important risk factor for the development and persistence of ocular inflammation (86).

The first-line treatment for uveitis are corticosteroids due to their potent anti-inflammatory effects. However, prolonged corticosteroid use, alongside chronic inflammation, can lead to significant long-term complications, ultimately compromising treatment outcomes. In recent years, therapeutic strategies have advanced with the development of biologic agents, mainly monoclonal antibodies (mAbs). Among these, anti-TNF-α therapies have become widely accepted for the management of uveitis, offering a more favourable safety profile compared to extended corticosteroid therapy (86).

In this regard, last July 2016, adalimumab became the first anti-TNF-α biologic approved by the United States Food and Drug Administration (FDA) for the treatment of non-infectious uveitis (88). While adalimumab has shown significant clinical efficacy, the ocular distribution remains insufficiently characterised. The accumulation of mAbs in ocular tissues is determined by multiple factors, such as drug bioavailability, permeability of blood-retinal barrier (BRB), molecular diffusion, tissues barrier permeability, and routes of administration (89). Although subcutaneous injection is the standard route, recent clinical trials have explored intravitreal administration as an alternative, demonstrating comparable, if not superior, efficacy in controlling intraocular inflammation, with a notably lower incidence of systemic adverse events. Importantly, these findings are based on the evaluation of a single IVT dose, which limits broader conclusions regarding long-term safety and optimal dosing regimens (90,91). A deeper understanding of biodistribution would allow for the development of more effective and personalized strategies and, such insights, could optimize drug delivery, enhance efficacy, and reduce systemic side effects.

In this context, non-invasive molecular imaging techniques, particularly positron emission tomography (PET), offer valuable insights into drug pharmacokinetics and tissue distribution. Employing radiolabelled antibodies, enables real-time, whole-body tracking of therapeutic mAbs and it has demonstrated substantial promise in oncology for both preclinical and clinical applications (63). Instead, its application in inflammatory diseases is still emerging, with recent studies exploring its potential in models of uveitis (64), arthritis (65), and colitis (66).

The objective of this study was to evaluate and compare the *in vivo* biodistribution and pharmacokinetics of adalimumab therapy following subcutaneous (SC) and intravitreal (IVT) administration in a rat model of systemic non-infectious uveitis (endotoxin-induced uveitis), using [^{89}Zr]Zr-DFO-adalimumab ImmunoPET. This approach enables visualization and quantification of mAb delivery to the eye, offering novel insights into the relationship between administration route, systemic pharmacokinetics, and target site engagement.

2.SPECIFIC METHODS

2.1 ANIMALS

A total of 28 male Sprague-Dawley rats, with an average weight of 262.8±28.2g, were obtained from the animal facility of the Centre for Experimental Biomedicine of Galicia (CEBEGA), University of Santiago de Compostela (Spain). Animals were housed in groups of 2 per cage under standardized environmental conditions, including controlled temperature (22 ± 1 °C), relative humidity (60 ± 5%), and a 12-hour light/dark cycle. Rats had unrestricted access to food and water (ad libitum) throughout the study period. A total of 18 animals were included in the PET study (12 with uveitis and 6 controls), and 10 animals were used in the quantitative real-time polymerase chain reaction (qPCR) study (5 with uveitis and 5 controls).

All experimental procedures were carried out in compliance with European and national regulations for the ethical use of animals in research. Experiments were approved by the Committee for Ethical Research of the Health Research Institute of Santiago de Compostela (IDIS) (15012/2021/001) and followed the Spanish and European Union (EU) rules (86/609/CEE, 2003/ 65/CE, 2010/63/EU, RD 1201/2005, and RD53/2013).

2.2 ENDOTOXIN-INDUCED UVEITIS MODEL

The animals were randomly assigned to two experimental groups: uveitis group (n = 17) and a healthy control group (n = 11). Before uveitis induction, animals were anesthetized in a veterinary gas chamber with 2.5-3% (v/v) isoflurane/oxygen (Baxter®, Deerfield, Illinois, USA). During inductions, animals were anesthetized in a platform with a face mask with 2-2.5% of isoflurane/oxygen. For the induction, the protocol previously described in the literature was followed, consisting of an injection of Escherichia coli LPS at a dose of 1 mg/kg diluted in 0.1 mL of balanced salt solution (BSS™, Alcon Healthcare, Texas, USA) into the right hind paw of the rat (92–95). The induction models were carried out 24 hours prior to all experimental procedures, corresponding to the peak of inflammation (96).

2.3 [^{89}ZR]ZR-DFO-ADALIMUMAB PET/CT IMAGING

For this study, the total number of animals was divided into groups according to both the route of administration of radiolabelled adalimumab and the experimental condition (disease model versus control). Uveitis group (n=12) was divided into two subgroups: subcutaneous (SC) uveitis (n = 6) and intravitreal (IVT) uveitis (n = 6), while two control subgroups were considered: IVT control (n = 3) and SC control (n = 3).

Animals were injected with [^{89}Zr]Zr-DFO-adalimumab (7.04 ± 0.73 MBq) subcutaneously. Before PET/CT scans, animals were anesthetized in a gas chamber containing 3–4% of isoflurane in oxygen (induction) and then kept under anaesthesia with a face mask (2–2.5% of isoflurane in oxygen for maintenance). SC groups received [^{89}Zr]Zr-DFO-adalimumab (7.04 ± 0.73 MBq) into the abdomen by subcutaneous route, while IVT groups were injected into the vitreous chamber via *pars plana* with a surgical lamp and the help of a Hamilton syringe with a 35G needle with [^{89}Zr]Zr-DFO-adalimumab (3.47 ± 0.01 MBq). Before each scan, a 10 µL blood sample was collected from the tail vein of each animal. Static PET/CT scans were performed at 0, 2, 4, 8, 12, 24, 36, 48, 72, 96, 120, 144, 168, 192, 216 and 240h post

subcutaneous and intravitreal injections. All rats were weight after each PET and were euthanised in a CO_2 chamber.

2.4 IMAGE ANALYSIS

PET image analysis was performed using PMOD v4.2 software (PMOD Technologies, Zürich, Switzerland). Initially, PET and CT images were accurately fused to ensure precise localization and consistency across all measurements. The mean radioactivity concentration was determined for different manual volumes-of-interest (VOIs) located in the area under analysis: eyes (6 x 6 x 6 mm), liver (7 x 7 x 7 mm) and in SC group retention area (variable volume depending on the uptake) was additionally measured. They were corrected for decay and expressed in terms of percentage of injected dose per milliliter (%ID/mL), as follows:

$$\%ID/ml = \frac{Mean\ radioactivity\ concentration\ in\ VOI\ \left(\frac{kBq}{ml}\right) * Volume\ of\ VOI\ (ml)}{Injected\ dose\ (kBq)} * 100$$

2.4.1 Image analysis of retention area

Due to the irregular uptake in the SC injection area among the animals, this was analysed. For the delineation of the abdominal injection site, a constant saturation threshold was applied to all PET images in order to standardise the visualisation of the areas with the highest radiotracer uptake. Subsequently, the injection site was selected based on an analysis of the relative intensity distribution, identifying those regions exhibiting the highest values on the signal scale.

2.5 IMPACT OF ADALIMUMAB ADMINISTRATION ROUTE ON OCULAR BIOAVAILABILITY

To assess the impact of the administration route on ocular drug distribution, we first measure the sum of the activity of the 2 eyes, and then calculated the percentage of adalimumab concentrations increase in uveitis compared with healthy control eyes for each administration route. Specifically, we first determined the mean concentration of adalimumab at each time in healthy control eyes, separately for each route of administration. Subsequently, we assessed the difference in ocular drug concentration for each uveitis eye relative to the mean concentration observed in control eyes at corresponding time points, as follow:

$$[Uveitis\ eye]\ (\%) = \frac{([Uveitis] - ([Controls\ mean]))}{[Controls\ mean]} * 100$$

The increase of the [^{89}Zr]Zr-DFO-adalimumab concentration was interpreted as an indicator of relative ocular drug bioavailability. Positive values (in %) indicate a higher concentration of the adalimumab in diseased eyes relative to healthy eyes (negative values would suggest a higher concentration in healthy controls than in diseased eyes). This approach allowed an evaluation of the efficiency of drug delivery to the eye for each route of administration (SC or IVT), highlighting differences in ocular drug penetration and bioavailability under pathological versus physiological conditions.

2.6 RNA ISOLATION AND QPCR ANALYSIS

Quantitative analysis of TNF-α, IL-6, IL-8, IL-10, and MIP-1α expression was performed in ocular tissues from uveitis (n = 5) and control (n = 5) animals using real-time PCR, following

the protocol established in our previous study (95). After the animal was slaughter, the eyeballs were enucleated and stored at -80 °C and the right eyes were used (the left eye was used for a proteomic study already published (97)). TRIzol reagent (Invitrogen, Barcelona, Spain) was used to isolated total RNA. RNA purification was carried out using the PureLink™ RNA Micro Scale Kit (Thermo Fisher Scientific), according to the manufacturer's instructions. After the binding, washing, and elution steps, RNA concentration and purity were assessed using a NanoDrop spectrophotometer (Thermo Fisher Scientific). cDNA was synthesized using the High-Capacity cDNA Reverse Transcription Kit (Applied Biosystems). A volume of 20 µL with 2 ug of cDNA (complementary deoxyribonucleic Acid) was mixture in a thermal cycler for a three-step reaction: an initial incubation at 25 °C for 10 minutes to allow primer binding, followed by reverse transcription at 37 °C for 120 minutes. Inactivation occurred at 94 ºC for 10 s, while annealing and extension were 58 s and 72 ºC respectively, both for a period of 10 s. Quantitative real-time PCR was performed using Luminaris Color HiGreeengPCR Master Mix (Fisher Scientific, Rockford, IL, USA). SYBR Green fluorescence was used to find the amount of PCR products formed in each cycle. 18S was used as an endogenous control.

3. RESULTS

3.1 CONJUGATION AND RADIOLABELLING OF [^{89}ZR]ZR-DFO-ADALIMUMAB

Adalimumab was successfully conjugated with DFO molecules as confirmed by radio-HPLC analysis. No dimer formation was observed in the chromatogram post-conjugation. Biological activity study after adalimumab conjugation was descripted in chapter 1. The theoretical specific activity was 74 MBq/mg and was consistent across all animals. Following radiolabelling, the RCP was 99.85%.

3.2 ENDOTOXIN-INDUCED UVEITIS MODEL

3.2.1 RNA isolation and quantitative real-time polymerase chain reaction (qPCR) analysis

To confirm the presence of proinflammatory cytokine RNA in the right eye unextracted, RNA analysis of proinflammatory cytokines TNF-α, MIP-1α, IL-6 and IL-8 was performed in uveitis (n=5) and control animals (n=5). Figure 17 shows the representation of these proinflammatory cytokines present in the different groups of animals studied (healthy control group and uveitis group).

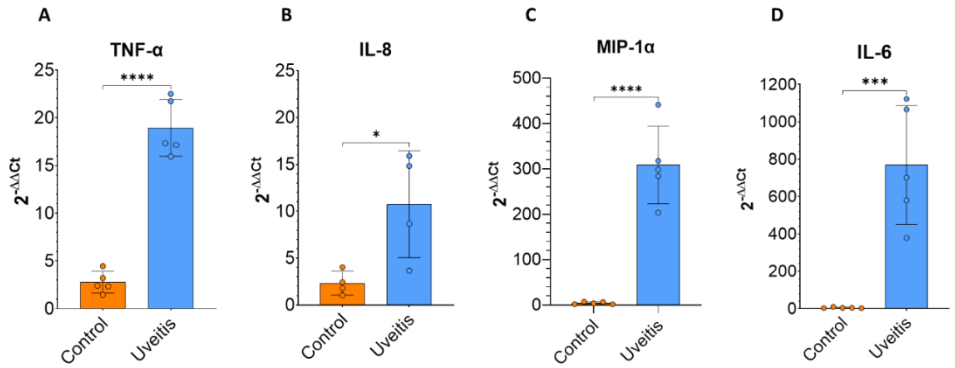

Figure 17: Representation of the different proinflammatory cytokines evaluated in each study group for PCR (A: TNF-α; B: IL-8; C: MIP-1α; D: IL-6). Values are expressed as mean ± SD. *, p < 0.05; **, p < 0.01 ***, p < 0.001, ****, p < 0.0001.

Significantly higher values of TNF-α were found in the tissues that had had induced compared to the healthy control group confirming the presence of inflammation in those tissues ($p<0.001$). In turn, the group induced had significantly higher values of IL-8, MIP-1α and IL-6 compared to the healthy control group ($p=0.026$; $p<0.001$; $p<0.0001$ respectively).

3.3 [^{89}Zr]Zr-DFO-adalimumab in blood

Figure 18 shows the blood permanence of [^{89}Zr]Zr-DFO-adalimumab after SC and IVT injection in uveitis and control groups.

We observe that [^{89}Zr]Zr-DFO-adalimumab exhibited significantly higher clearance in uveitis rats compared to controls, regardless of the administration route (Figure 18). The area under the curve in SC group showed a value of 178.6 ± 5.1 in controls and 126.6 ± 5.6 in uveitis rats. Similarly, in the IVT group, the AUC was 583.4 ± 48.5 for controls and 511.8 ± 33.4 for uveitis animals.

In SC cohorts, the highest concentration was observed at 24h p.i. and remained relatively stable until 36 hours, when it starts to decrease, after which a decline was noted in both groups. In control animals, the maximum was above 1.10 % ID/ml at 24, 36 and 48h (1.13 ± 0.13, 1.10 ± 0.06 and 1.15 ± 0.07, respectively). However, the uveitis group exhibited lower maximum concentrations, with the peak at 24 hours (0.90 ± 0.24 %ID/ml), followed by stable levels at 36 and 48 hours (0.85 ± 0.18 and 0.84 ± 0.12, respectively).

In the IVT group, peak concentration occurred at different times. In IVT-controls the peak was reached between 12 and 48h p.i., with a %ID /ml around 1.7 (1.72 ± 0.26, 1.75 ± 0.47, 1.69 ± 0.59 and 1.78 ± 0.60 at 12, 24, 36 and 48h p.i.). In contrast, IVT-uveitis animals showed a delayed peak at 72 and 96 h p.i., with % ID/ml values of 1.31 ± 0.34 and 1.31 ± 0.41, respectively. After these time points, both uveitis and control groups showed similar clearance patterns.

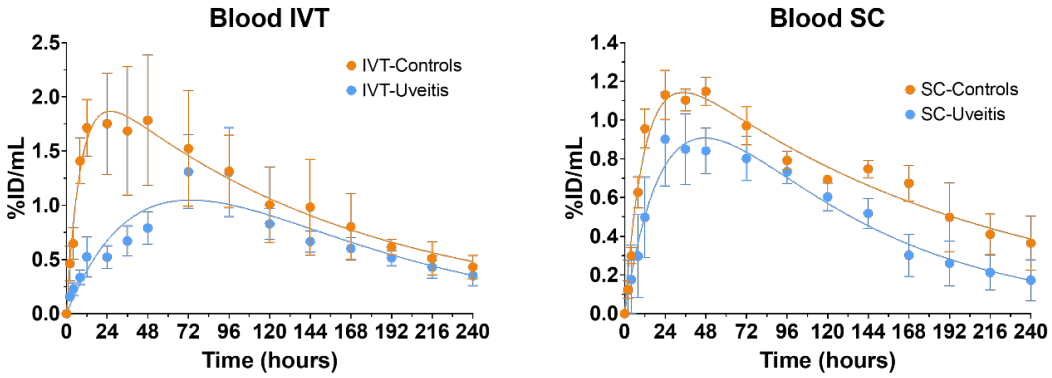

Figure 18: Blood permanence of [^{89}Zr]Zr-DFO-adalimumab (blood versus time) after SC injection (left) and IVT injection (right). Control group is shown in orange and Uveitis group in blue. Values are expressed as means ± SD.

3.4 Impact of adalimumab administration route on ocular bioavailability

Animals with uveitis exhibited higher ocular [^{89}Zr]Zr-DFO-adalimumab cumulative concentrations compared to controls when the compound was administered intravitreally (AUC 5475 ± 265.37 vs 2422 ± 155.1).

Subcutaneous administration did not result in appreciable ocular uptake in uveitis animals; notably, control animals displayed higher ocular cumulative concentrations than uveitis animals under this route (AUC in uveitis group: 139.8 ± 2.9; controls: 92.68 ± 4.05) (Figure 19). In this

case, ocular concentration of [^{89}Zr]Zr-DFO-adalimumab was significantly influenced by the route of administration, and not by local TNF-α expression levels which also increase BRB permeability, only slightly in the case of intravitreal injection and not at all following subcutaneous administration, which even showed an inverse behaviour.

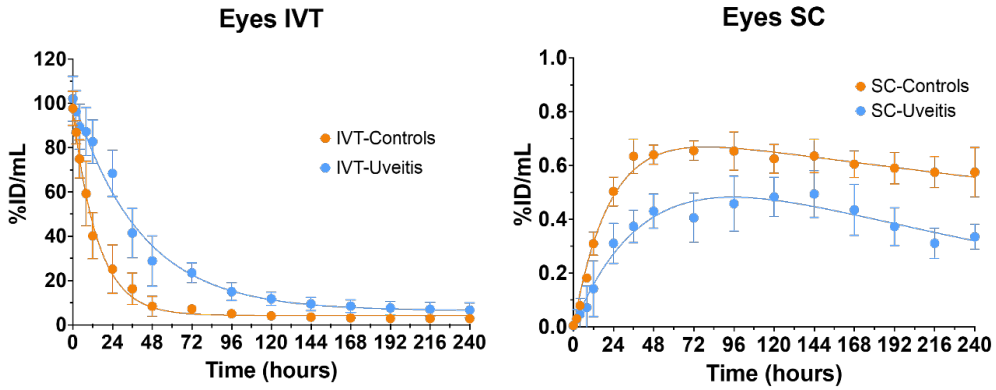

Figure 19: Temporal dynamics of [^{89}Zr]Zr-DFO-adalimumab retention in eyes following IVT (left) and SC (right) administration in controls and uveitis groups.

When comparing ocular concentrations between uveitis and control groups following IVT and SC administration, positive values indicate a higher concentration in the uveitis group, while negative values reflect greater levels in controls (see Figure 20). In the IVT group, ocular concentrations were consistently elevated in uveitis cases, with the most notable differences observed at 48–72 hours (+244% and +226%). Conversely, in the SC group, concentrations were uniformly higher in controls, peaking at 12–24 hours (-60% and -55%), followed by a stabilisation phase with an average decrease of approximately 35% (Figure 20).

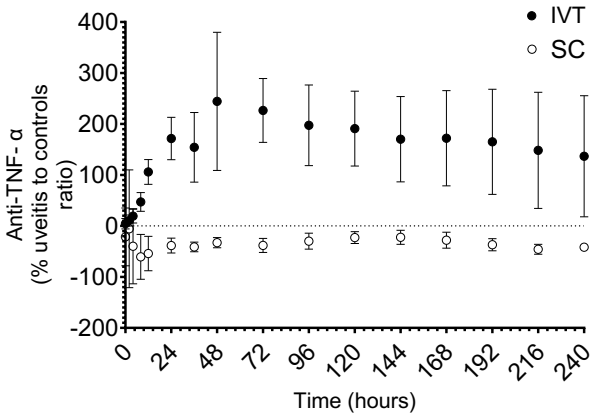

Figure 20: Percentage increase of adalimumab anti-TNF-α in eyes with uveitis compared to controls over time following intravitreal (black) and subcutaneous (white) administration.

3.5 ADALIMUMAB WHOLE-BODY PET BIODISTRIBUTION

Anti-TNF-α PET imaging was used to evaluate the whole-body biodistribution of [^{89}Zr]Zr-adalimumab (Figure 21). Following a 48 h period post injection to allow for systemic biodistribution, it was observed that both SC and IVT administered control animals exhibited higher and diffuse radiotracer uptake throughout the body, consistent with elevated radiotracer levels in the vascular compartment. Notably, significant uptake was also observed in lymphoid tissues. In the SC-administered group, pronounced accumulation was seen in axillary lymph

nodes and the thymus. In contrast, the IVT-administered group showed increased uptake in the cervical lymph nodes.

Additionally, within the SC-administered group, animals with uveitis (SC uveitis) demonstrated greater tracer uptake at the injection site compared to SC controls, as shown in Figure 23.

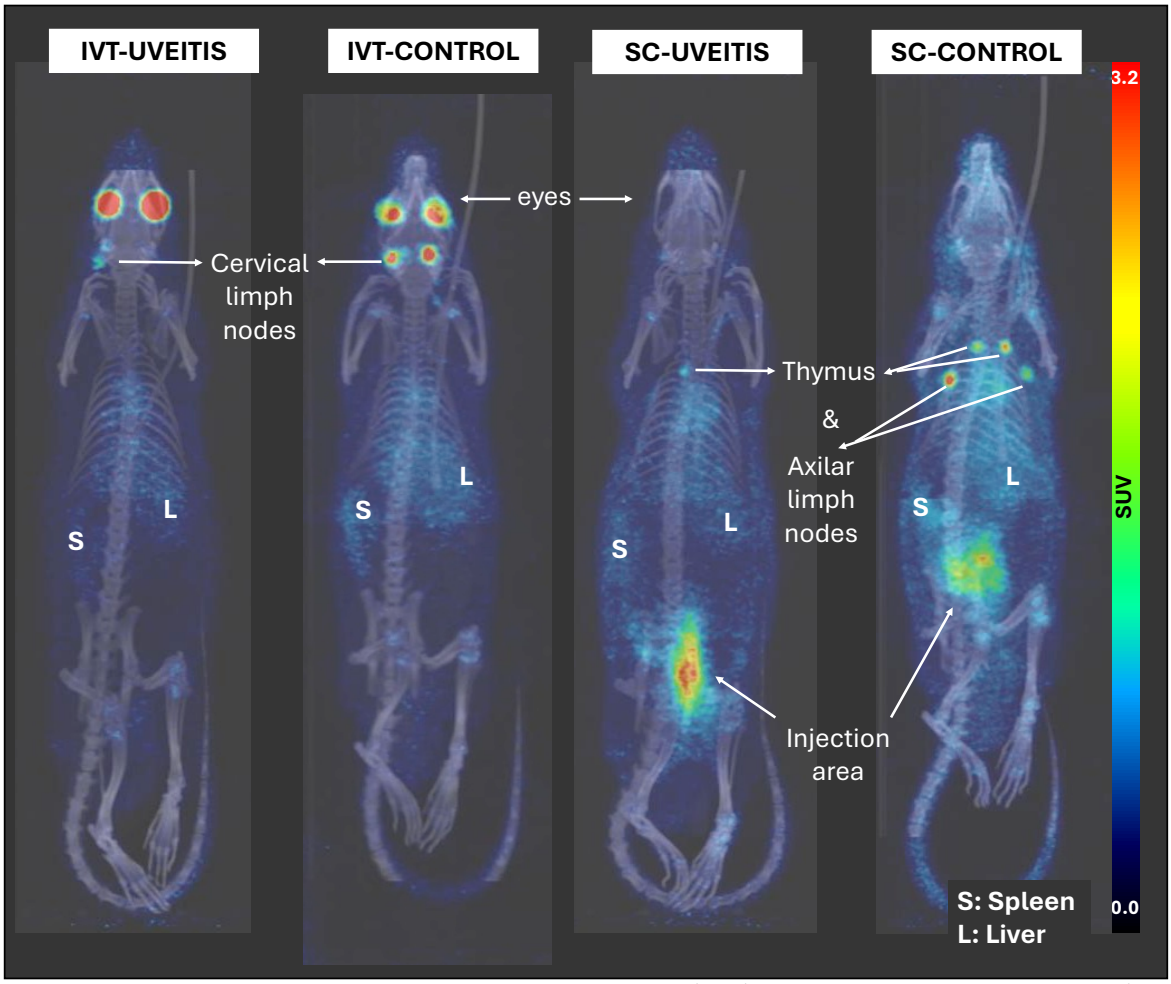

Figure 21: Representative PET images (MIP format) acquired 48 h p.i. from IVT-uveitis, IVT-control, SC-uveitis and SC-control groups. White arrows indicate the eyes, lymph nodes, and injection sites. The livers (L) are also labelled.

Figure 22A and Figure 22B show the temporal evolution of liver in %ID/ml values for both control and uveitis groups across IVT and SC administration routes. In the IVT group, uveitis animals exhibited a peak liver uptake (%ID/mL) at 72 hours post-injection (0.95 ± 0.18), after which the values remained stable. This uptake was significantly lower than that observed in control animals (1.40 ± 0.26, $p < 0.05$). In contrast, control animals reached their peak liver uptake earlier, at 12 hours post-injection (1.17 ± 0.30), followed by a stable plateau.

SC group, similar to IVT group, showed both in uveitis and control animals progressive increase in liver uptake up to 48 hours, with control animals displaying higher values (1.04 ± 0.28 vs. 1.35 ± 0.04). Thereafter, uptake began to decline in both groups. Notably, from 168 hours post-injection, a renewed increase in liver uptake was observed across all groups, more modest in control animals (1.56 ± 0.75) and more pronounced in uveitis animals (2.06 ± 0.53).

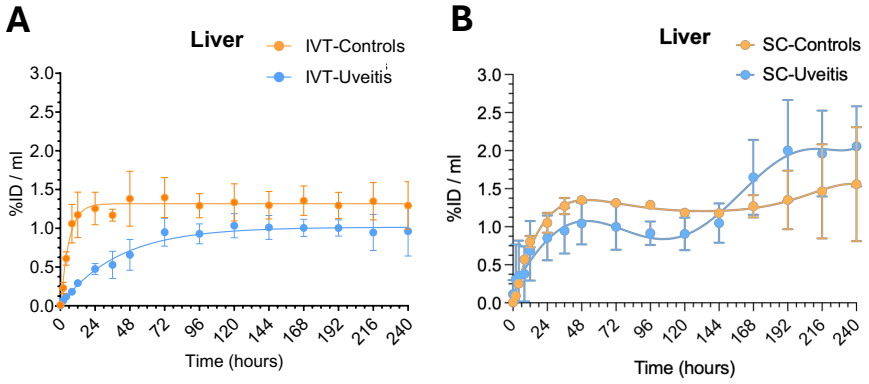

Figure 22: Liver %ID/ml values of control group (orange) and IBD group (blue) over time after IVT injection (A) or SC injection (B).

3.5.1 Retention in the injection area

Following SC administration of [^{89}Zr]Zr-DFO-adalimumab, the retention of the drug in the injection site was significantly higher in the uveitis group compared to the healthy control group (AUC uveitis: 3514 ± 177.7; controls: 1812 ± 75.58). This differential retention was particularly notable during the early stages post-injection. At earlier time points, the concentration of [^{89}Zr]Zr-DFO-adalimumab in the uveitis injection area was significantly greater than that observed in the control group. As expected, this difference in retention gradually diminished over time, with the concentrations of [^{89}Zr]Zr-DFO-adalimumab in both the uveitis and control groups becoming comparable after 72 hours post-injection, as depicted in Figure 23.

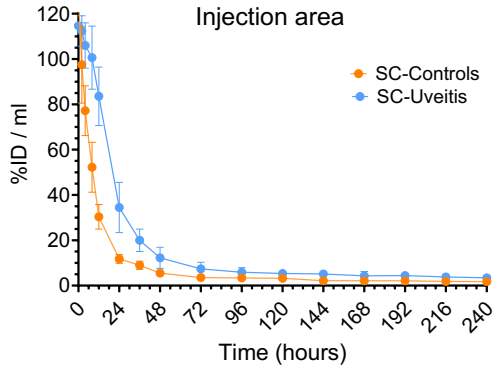

Figure 23: Temporal dynamics of [^{89}Zr]Zr-DFO-adalimumab retention in the injection area following SC administration in controls and uveitis groups.

4. Discussion

The management of non-infectious uveitis with anti-TNF-α therapies has historically relied on clinical evaluation of ocular inflammation, such as anterior chamber cell counts, vitritis grading, and retinal findings, to guide treatment decisions. Therapeutic modifications are largely empirical: dosing intervals are adjusted, biologics are switched, or combined with conventional immunosuppressants solely on the basis of observed clinical response. This approach does not incorporate pharmacokinetic information, as the ocular penetration and retention of these antibodies remain poorly characterized. In this context, molecular imaging with radiolabelled anti-TNF-α provides a unique opportunity to visualize drug distribution *in vivo* and may help refine treatment strategies toward a more rational and personalized approach.

Although adalimumab is currently approved only for SC administration, Hassoun M et al. have recently reported the results of a clinical trial showing that IVT administration is not less effective than the SC route and is associated with fewer adverse effects (91). However, neither the optimal dose nor the administration regimen has yet been established. Nevertheless, the ability of SC mAbs to penetrate ocular tissues has not been previously assessed *in vivo.* To directly compare IVT and SC administration of adalimumab, we have applied a new PET-based methodology using [^{89}Zr]Zr-DFO-adalimumab following a strategy previously developed by our group (57,64–66). The biodistribution of the antibody was delineated following SC and IVT administration route, using new experiments and reanalysed data from previous study by Garcia-Otero et al (71).

As first step, our findings regarding cytokine RNA expression confirmed elevated levels of pro-inflammatory cytokines in uveitis-induced animals compared with controls. Specifically, increased expression of IL-6, IL-8, MIP-1α, and TNF-α was observed, thus confirming that the model was correctly generated. These results confirm that LPS administration induces a significant inflammatory response in the eye, consistent with findings by Andrea Cuartero et al. (97), who also reported elevated inflammatory mediators in this model relative to healthy controls.

Specifically, regarding our results from the [^{89}Zr]Zr-DFO-adalimumab PET study, analysis of adalimumab concentrations in blood further revealed lower levels in disease groups compared to controls, suggesting that more mAb remains available systemically in healthy animals. Notably, even following IVT administration, higher circulating levels of adalimumab were detected in control animals during the early time points. This suggests that in uveitis groups, adalimumab is retained in the injection point (vitreous or injection point of SC administration) rather than diffusing into the bloodstream, possibly due to TNF-α affinity in this area. In line with this, recent PBPK modelling of [^{89}Zr]Zr-DFO-adalimumab in the LPS uveitis model has predicted that increased local TNF-α concentrations and BRB alterations can significantly slow ocular clearance and prolong intravitreal retention, particularly in inflamed eyes (98). Regarding the bioavailability in the eye, IVT administration of [^{89}Zr]Zr-DFO-adalimumab led to ocular concentrations up to two orders of magnitude higher than SC administration. While expected, the result is striking, subcutaneous delivery resulted in minimal ocular uptake, with even lower concentrations in uveitis animals than in controls, highlighting the limited ability of the adalimumab to reach the eye via SC administration.

In this regard, the BRB plays a crucial role in regulating ocular drug delivery, serving as a selective barrier that protects the internal ocular environment. Previous studies have identified TNF-α as a key contributor to BRB disruption via its effects on retinal pigment epithelium integrity and inflammatory signalling (99). Elevated TNF-α levels have been linked to increased vascular permeability and BRB breakdown in uveitis models (100). Although BRB disruption facilitates intraocular diffusion, our data showed that after SC administration, no ocular antibody uptake was observed in uveitis animals. Instead, higher adalimumab retention was found in inflamed eyes compared to controls following IVT administration. This observation aligns with PBPK simulations in LPS induced uveítis, showing that inflammatory changes in ocular physiology, including barrier disruption and increased antigen presence, enhance local retention but do not compensate for the low ocular delivery efficiency of systemic administration (98). Upon normalising the SC biodistribution data between uveitis and control animals, we observed that subcutaneously administered adalimumab fails to reach the ocular globe in diseased animals. We suspect that these low levels of adalimumab in the eyes may be influenced not only by BRB but also by systemic inflammatory activity after LPS induction (101) and the retention in the administration area as we showed in Figure 23. In the first case,

we hypothesise that, in this model, adalimumab may be sequestered in other inflamed organs as also suggested by Andrea Cuartero et al. (97), thereby limiting its ocular bioavailability. And on the other hand, the retention in the administered area shows an increase in binding already at the injection site, which is consistent with the high serum TNF levels described by Jiang Q et al. in this model (86).

In the eyes, the concentration curves of [^{89}Zr]Zr-DFO-adalimumab (Figure 19) demonstrate a rapid decline in drug concentration following intravitreal (IVT) administration. In control animals, concentrations were almost undetectable by 72 hours post-injection, whereas in uveitis-induced animals, this decline was delayed until 144 hours post-injection. This suggests an altered ocular clearance potentially attributable to target binding, where the antigen–antibody complex may be eliminated more slowly (64). In contrast, following subcutaneous (SC) administration, the concentration decreased more gradually compared to the intravitreal route. Control animals exhibited relatively stable ocular concentrations, peaking at 48 hours and remaining constant up to 240 hours (102). Uveitis-induced animals showed a similar profile up to 144 hours post-injection, after which ocular concentrations began to decline. Additionally, the uveitis group consistently exhibited lower concentrations than controls. This difference in ocular concentrations between control and uveitis animals may reflect altered drug absorption or increased retention in the latter, suggesting a slower distribution process. Following subcutaneous administration, a stabilization phase with relatively high drug concentrations was sustained for a longer duration. This may indicate that systemic distribution via the subcutaneous route enables prolonged exposure, potentially offering therapeutic benefits for conditions that require continuous drug presence in systemic circulation (102). The observed results following SC administration may be related to reduced drug clearance, thereby extending its systemic residence time.

In control animals, high concentrations of adalimumab were observed in lymphoid organs near injection area, such as the thymus and axillary lymph nodes (in the SC group), and cervical lymph nodes (in the IVT group). These organs serve as immunological reservoirs where physiological levels of TNF may be present, potentially leading to local retention of anti-TNF-α agents. Additionally, due to their large molecular size, mAbs primarily circulate via the lymphatic system. In control conditions, this allows their accumulation in lymphoid tissues. However, in uveitis subjects, the lymphatic flow is redirected toward the site of inflammation, carrying immune mediators, including anti-TNF mAbs, toward the inflamed tissues(103).

These results align with hepatic biodistribution patterns observed in healthy animals, where higher levels of radiolabelled adalimumab were detected. This accumulation is likely attributable to the presence of circulating antibody within the hepatic vasculature. The liver is a key organ in the catabolism of therapeutic monoclonal antibodies, where they are progressively degraded into peptides and amino acids that may be recycled for endogenous protein synthesis (80). This metabolic activity likely contributes to the elevated hepatic signal observed in PET imaging.

Following IVT administration, hepatic uptake of adalimumab was consistently greater in control animals. A similar trend was observed after SC administration, although at 168 h p.i, liver-associated radioactivity was higher in uveitis models compared to controls. These findings suggest the formation and systemic clearance of anti-TNF-α immune complexes appear later, particularly under inflammatory conditions.

The binding of adalimumab to the eye following SC administration is notably low, which was expected. However, it is surprising that it is even lower in the uveitis group compared to the controls. This observation suggests that, in uveitis, binding may occur preferentially in other

parts of the body. With all this information and knowing that adalimumab is an approved and effective treatment for non-infectious uveitis (85), its effect indirectly benefits the eye by modulating systemic immune activity even if it is not able to penetrate the eye. Importantly, non-infectious uveitis is not only a localised ocular condition because it often manifests as a systemic autoimmune disease, affecting other organs in up to 40% of patients (86). These findings may offer critical insights into improving current therapeutic strategies for uveitis. Specifically, they highlight the potential limitations of SC administration in effectively delivering adalimumab to treat eyes and suggest that IVT administration may represent a more effective route in patients unresponsive to SC treatment.

5. CONCLUSION

This is the first study focused on using PET imaging with [^{89}Zr]Zr-DFO-adalimumab to compare administration routes of adalimumab in non-infectious uveitis. This approach enables *in vivo* whole-body quantification of antibody biodistribution and provides novel insights into how delivery method impacts ocular bioavailability.

Our findings underscore the importance of administration route in the effective delivery of anti-TNF-α therapies for non-infectious uveitis. While subcutaneous administration is less invasive and widely used, our findings suggest that it may be insufficient for achieving therapeutic concentrations within inflamed ocular tissues. Intravitreal administration, by contrast, ensures higher local retention of the antibody. Moreover, systemic inflammation may further hinder ocular bioavailability by diverting antibodies to other affected organs. These insights suggest that intravitreal delivery should be considered in patients with poor response to systemic anti-TNF-α treatment and support a more personalised approach to the management of uveitis.

CHAPTER III

PET-BASED ASSESSMENT OF [^{89}ZR]ZR-ADALIMUMAB TARGETING AND BIODISTRIBUTION IN THE K/BXN MURINE MODEL OF ARTHRITIS

ABSTRACT:

Rheumatoid arthritis (RA) is a chronic autoimmune disease driven by pro-inflammatory cytokines, particularly TNF-α, which plays a critical role in joint inflammation and damage. In this study, we characterized the K/BxN serum-transfer arthritis model using [^{89}Zr]Zr-DFO-adalimumab PET to non-invasively visualize TNF-α biodistribution and inflammatory activity *in vivo*. Following successful radiolabelling of the adalimumab monoclonal antibody, with high radiochemical purity and serum stability, PET/CT imaging revealed progressive and joint-specific tracer accumulation, particularly in the ankle joints from day 7 post-induction, consistent with increased joint diameter and elevated [^{18}F]FDG uptake. Blood pharmacokinetics showed initially lower circulating tracer levels in arthritic animals compared to controls, but convergence occurred by 12 h post-injection. PET analysis demonstrated spatial heterogeneity, with at least two inflamed joints per animal showing significant tracer uptake, although some joints, notably in the wrist, exhibited minimal signal. *Ex vivo* analysis confirmed increased TNF-α expression at both the mRNA level in joints and protein level in serum, which remained unaffected by radiotracer injection, indicating that the imaging approach did not alter cytokine biology. Histological examination supported these findings, revealing leukocyte infiltration and proteoglycan depletion in arthritic cartilage. These results establishes a robust and reproducible preclinical RA model, showing that [^{18}F]FDG and [^{89}Zr]Zr-DFO-adalimumab PET/CT imaging, combined with histological validation, provide a powerful toolkit for studying RA progression and TNF-α expression. These findings could aid in the development of new diagnostic and therapeutic strategies, particularly those targeting TNF-α, a key inflammatory mediator in RA.

GRAPHICAL ABSTRACT:

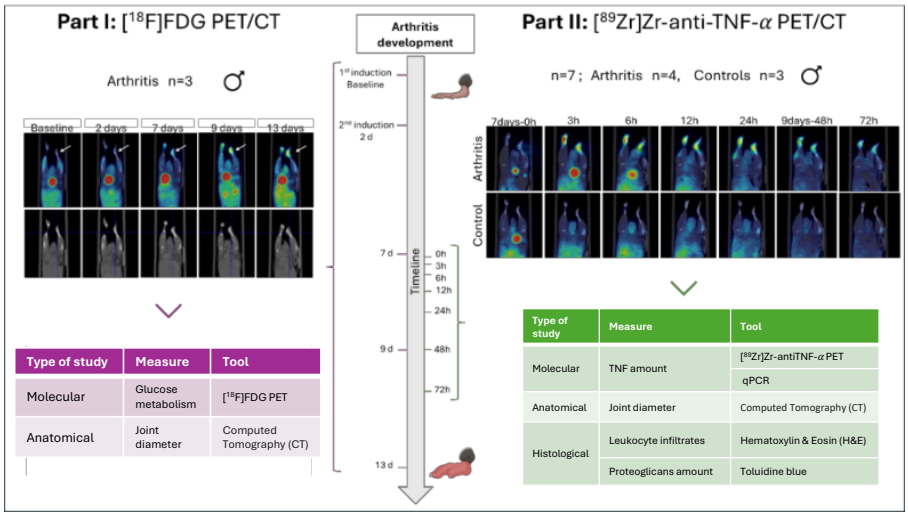

Figure 24: Graphical abstract illustrating the experimental design and multimodal assessment strategies employed to monitor inflammatory processes in a murine model of arthritis. Longitudinal evaluation of joint inflammation was performed using molecular, anatomical, and histological approaches. On the left, [^{18}F]FDG PET and CT imaging were employed to assess glucose metabolism and joint diameter, respectively, at multiple timepoints post-induction. On the right, [^{89}Zr]Zr-adalimumab PET, qPCR, ELISA, CT, H&E and toluidine blue staining were used to evaluate TNF-α expression, leukocyte infiltration, and proteoglycan content. The timeline in the centre summarises the experimental progression. Tables below each panel detail the type of study, measured parameter, and corresponding analytical tools. Created with BioRender.com

1.INTRODUCTION

Rheumatoid arthritis (RA) is a chronic, systemic autoimmune disease that primarily manifests as inflammatory arthritis, typically affecting the small joints of the hands and feet. If left untreated, RA can lead to severe disability and even death (104). Diagnosis of RA relies on clinical assessment, serological markers and imaging as X-rays, magnetic resonance and or ultrasound imaging. Current therapies involve drugs such as methotrexate or antibodies like adalimumab, an anti-TNF-α drug to reduce inflammation and slow disease progression (105).

Regarding pathogenesis of RA, pro-inflammatory cytokines, particularly tumor necrosis factor-alpha (TNF-α), play a pivotal role in driving inflammation in RA. Elevated levels of these cytokines have been detected in the synovium, synovial fluid, serum, and peripheral blood of RA patients (106). Due to its central role in RA pathogenesis, TNF-α has become a major therapeutic target, with TNF inhibitors such as adalimumab mentioned before. However, despite their efficacy, up to 24% of patients treated with adalimumab require salvage therapy between weeks 14 and 26, highlighting the need for improved therapeutic strategies (107)

The development of new therapeutic strategies, as well as the optimization of existing ones such as adalimumab, requires robust preclinical research using animal models. Among the available experimental models, the K/BxN serum transfer model allows an earlier induction of arthritic symptoms (around 7 days). It is not as extensively studied as collagen-induced arthritis (108) where first signs of arthritis appear approximately 21 to 28 days after immunization (109), its characteristics make K/BxN serum transfer model particularly valuable for a wide range of applications and in particular for studying TNF-α (110).

In the context of preclinical research, non-invasive molecular imaging techniques such as PET offer powerful tools to study *in vivo* drug biodistribution. In particular, ImmunoPET, which combines PET imaging with radiolabelled monoclonal antibodies (mAbs), enables real-time, whole-body tracking of therapeutic antibodies and has shown considerable promise in preclinical and clinical research (111–113).

This study aims to evaluate the biodistribution and specific targeting of [^{89}Zr]Zr-DFO-adalimumab to inflamed joints in the K/BxN murine model of rheumatoid arthritis using PET/CT imaging. This approach allows for the visualization and quantification of antibody accumulation in arthritic joints, providing new insights into the relationship between adalimumab biodistribution, circulating TNF-α levels, and local TNF-α expression in the affected joints.

2. SPECIFIC METHODS

2.1 ANIMALS

A total of 16 male C57BL/6 mice were divided into two experimental groups: arthritic group (n=10) and healthy control group (n=6). All animals were obtained from the animal facility of the Centre for Experimental Biomedicine of Galicia (CEBEGA), University of Santiago de Compostela (Spain). These animals were further subdivided into two cohorts: one designated for a longitudinal *in vivo* PET imaging study (arthritic group, n = 7; control group, n = 3), and the other for a longitudinal *ex vivo* study (arthritic group, n = 3; control group, n = 3).

Animals were housed in groups of 3 to 4 per cage under standardized environmental conditions, including controlled temperature (22 ± 1 °C), relative humidity (60 ± 5%), and a 12-hour light/dark cycle. Mice had unrestricted access to food and water (ad libitum) throughout the study period.

All experimental procedures were carried out in compliance with European and national regulations for the ethical use of animals in research (86/609/CEE, 2003/65/CE, 2010/63/EU and RD53/2013), as well as the ARRIVE guidelines. The study protocol was reviewed and approved by the Animal Ethics Committee of the University of Santiago de Compostela (code 15012/2022/011).

2.2 KBX/N ARTHRITIC MODEL

The K/BxN serum-transfer arthritis model was used to induce acute RA in mice. The model is based on the transfer of arthritogenic serum from K/BxN mice which spontaneously develop arthritis at 4 to 5 weeks of age into naïve mice. To obtain the serum, blood was collected from 4 to 8 week-old arthritic K/BxN mice via the submandibular vein. Serum were pooled and stored at −80 °C until further use (110). K/BxN mice were generated by crossing male KRN T cell receptor transgenic mice (a kind gift from Dr. Carmen Conde, Instituto de Investigación Sanitaria de Santiago de Compostela, IDIS, Spain) with female NOD/ShiLtJ mice (Charles River Laboratories, Barcelona, Spain). C57BL/6J mice, used as serum recipients, were bred and maintained at the Centre for Experimental Biomedicine (CEBEGA, University of Santiago de Compostela, Spain).

Arthritis was induced in C57BL/6J mice by intraperitoneal administration of 100 µL K/BxN serum on days 0 and 2. After 10 days (peak of symptoms) the animals will be sacrificed, hindlimbs comprising the ankle and metatarsophalangeal joints will be stained with H&E, safranin-O, for the evaluation of inflammation and bone erosion, respectively. Expression of inflammatory mediators will be evaluated through mRNA isolation from right forelimbs, cDNA synthesis and qPCR. Mice serum will be collected on the day of sacrifice and the production of proinflammatory cytokines will be measured via ELISA.

All animal procedures were performed in accordance with Spanish legislation for the protection of animals used for scientific purposes (Real Decreto 1386/2018) and were approved by the Ethics Committee for Animal Research of the University of Santiago de Compostela and the regional Galician authorities (authorization no. 15012/2022/007).

2.3 [^{18}F]FDG PET/CT IMAGING

[^{18}F]FDG PET/CT scans were performed to study model development, with the first scans taken immediately after the first and second inductions (on days 0 and 2), followed by scans on days 7, 9, and 13. Arthritic model animals (n=3) were under fasting conditions the night before the scan. Mice were placed on a grid floor during fasting to avoid coprophagia. Before PET, animals were anesthetized in a gas chamber containing 3% of isoflurane in oxygen for the induction and then kept under anesthesia with a face mask (2–2.5% of isoflurane in oxygen for maintenance). Animals were injected with 6.49 ± 0.37 MBq of [^{18}F]FDG through the tail vein, then animals woke up few minutes later and they remained at rest. Thirty minutes after the radiotracer administration, PET/CT static acquisitions were performed in a microPET/SPECT/CT Albira Bruker (Bruker Biospin Corp. Billerica, MA), consisting of 10 min PET scan (covering whole-body) followed by a 10 min CT scan (35 kV for a tube current of 200 μA with 250 projections per bed, centred in the abdominal region). Finally, animals were returned to their cages with free access to food and water.

2.4 [^{89}Zr]Zr-DFO-adalimumab PET/CT IMAGING

Arthritic model animals (n=4) and control animals (n=3) were placed in a gas chamber containing 3% isoflurane in oxygen until they were unconscious. Afterwards, the animals were removed from the chamber and were kept under the effects of anesthesia (2% of isoflurane) for the administration of [^{89}Zr]Zr-DFO-adalimumab. Animals were injected with [^{89}Zr]Zr-DFO-adalimumab (3.97 ±0.20 MBq, 60 μg) through the tail vein,as it enables a faster and more uniform biodistribution, guarantees full bioavailability of the administered dose, and minimises background radioactive signal. It was injected 7 days after the first induction, and the study was continued for 3 days, the time range during which inflammation is persistent. Before the scans, a blood sample of 10 ul was collected from the tail vein of all animals. PET/CT static acquisitions (following the acquisition protocol mentioned in 2.3.2) were performed at 0h, 3h, 6h, 12h, 24h, 48h and 72h post injection (p.i.). Following euthanasia, *ex vivo* analyses were conducted, including serological and histological assessment of the ankles, and molecular analysis of the left wrist using qPCR. For the optimisation of serological and molecular protocols, samples from one arthritic animal were used; therefore, final results include n = 3 for the uveitis group and n=3 for the control group.

2.5 IMAGE ANALYSIS

PET image analysis was performed using PMOD v4.2 software (PMOD Technologies, Zürich, Switzerland). Joint SUV and SUVmax were obtained from ellipsoid VOIs (4.14 x 4.14 x 4.14 mm) manually delineated on the joint region. This size was determined by considering the average joint diameter of the controls measured via CT, the resolution of the PET scan, and positron range of the Zr-89 as follows:

$$\emptyset = \sqrt{(CT\ \emptyset)^2 + (PET\ resolution)^2 + (Zr89\ \ positron\ range)^2}$$

2.6 HISTOLOGICAL ANALYSIS

On days 8, 9, and 10 following serum injection (corresponding to the peak of symptoms), one control and one uveitic animal were euthanised for sample histological and molecular (qPCR and ELISA) study, in addition to the analysis of samples from animals subjected to the [^{89}Zr]Zr-

DFO-adalimumab PET/CT imaging study. Histological analysis was performed as previously described (114). Briefly, both hindlimbs, including the ankle and metatarsophalangeal joints, were prepared for histology by dissecting the skin and sectioning the joints. Samples were then fixed in 10% neutral buffered formalin (Bio-Optica) for 24 h, demineralized using the decalcifier kit for bone biopsy Mielotec (Bio-Optica), and embedded in paraffin. Some sections were stained using standard hematoxylin and eosin stains, to assess infiltration and bone erosion. Finally, some sections were stained with toluidine blue to assess the degree of cartilage damage.

2.7 RNA ISOLATION AND QUANTITATIVE REAL-TIME POLYMERASE CHAIN REACTION (qPCR) ANALYSIS

In parallel to the histological study, left wrists were homogenized using a physical homogenizer (Polytron immersion dispenser, Kinematica), while the right wrists are preserved for future western blot protein studies. The resulting lysate was incubated with TRIzol reagent (Qiagen), and total RNA was extracted from the aqueous phase following the addition of chloroform. RNA purification was carried out using the PureLink™ RNA Micro Scale Kit (Thermo Fisher Scientific), according to the manufacturer's instructions. After the binding, washing, and elution steps, RNA concentration and purity were assessed using a NanoDrop spectrophotometer (Thermo Fisher Scientific). Purified RNA samples were stored at –80 °C until use to prevent degradation.

cDNA was synthesized using the High-Capacity cDNA Reverse Transcription Kit (Applied Biosystems). An equal volume of reaction mix was added to the RNA sample, and the mixture was placed in a thermal cycler for a three-step reaction: an initial incubation at 25 °C for 10 minutes to allow primer binding, followed by reverse transcription at 37 °C for 120 minutes. Finally, the reaction was inactivated at 85 °C for 5 minutes. The resulting cDNA was stored at –80 °C.

Quantitative real-time PCR was performed in duplicate wells using PowerTrack SYBR Green (Thermo Fisher Scientific) in a QuantStudio™ 5 (Applied Biosystems) thermocycler. Gene expression was quantified by the ΔΔCt method, using as normalization control the *GAPDH* genes. Primers were designed with the Primer3 (115) using the genomic sequences provided by the National Center for Biotechnology Information as reference (Table 4), and synthetized by Condalab Co., (Torrejón de Ardoz, Madrid, España).

Table 4: Primer sequences used for (qPCR).

Gene	Amplicon length	Sequence
GAPDH	115	F: ACATCAAGAAGGTGGTGAAGC
		R: AAGGTGGAAGAGTGGGAGTTG
TNF	120	F: AGAAGTTCCCAAATGGCCT
		R: AGAAGTTCCCAAATGGCCT

2.8 ELISA

For quantification of serum level of TNF, enzyme-linked immunosorbent assay (ELISA) was performed using the ELISA MAX™ Standard Set Mouse TNF-α kit (Biolegend). The sandwich ELISA started with the coating of a 96 well plate with a capture antibody. After an incubation with the antigen, the plate was rewashed, and the primary antibody was added. Then, the secondary enzyme-conjugated antibody was added, and the substrate produces a color change depending on the amount of antigen.

2.9 STATISTICAL ANALYSIS

Simple linear regression analyses were conducted to explore associations between quantitative variables across multiple datasets. The strength and direction of the relationships were assessed using the regression coefficient and the coefficient of determination (R^2). Statistical significance was evaluated using p-values, with values below 0.05 considered indicative of a significant association. All analyses were performed using Graphpad Prism v10.

3.RESULTS

3.1 CONJUGATION AND RADIOLABELLING OF [^{89}ZR]ZR-DFO-ADALIMUMAB

Adalimumab was successfully conjugated with DFO molecules as confirmed by radio-HPLC analysis. No dimer formation was detected in the chromatogram following conjugation. Biological activity study after adalimumab conjugation was descripted in chapter I. The theoretical specific activity was 74 MBq/mg, consistent across all mice. Following radiolabelling, the RCP was 97.08%.

The stability of the radioconjugate, assessed by radiochemical purity after 7 days of incubation in human serum at 37 °C, was 98%.

3.2 ARTHRITIS MODEL

3.2.1 Joint diameter with Computed Tomography (CT)

A progressive diameter increase was observed in four joints when compared to baseline values (day 0 before induction), indicating a sustained accumulation of radiopharmaceutical over time. Notably, the most significant changes were detected from day 7 onwards, with the most pronounced accumulation localized in the ankle joints at day 13, but a slight increase was detected in the wrists at day 9 (Figure 25).

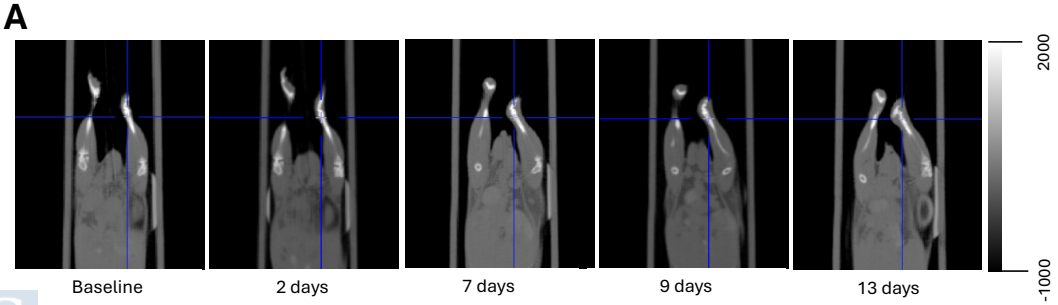

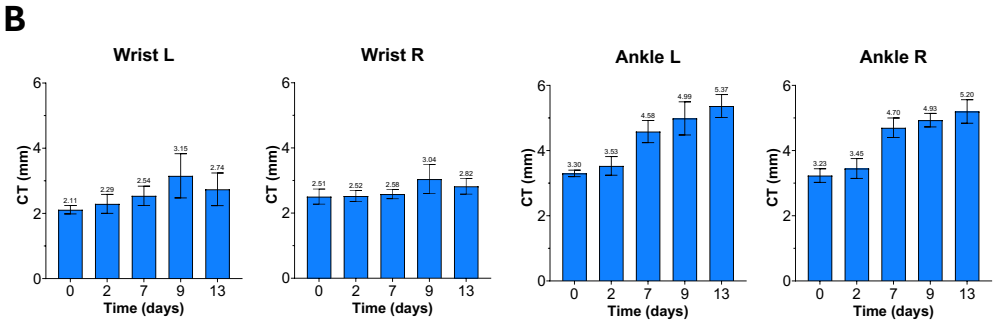

Figure 25: Longitudinal assessment of joint diameter following arthritis induction. Above: CT images of affected joints at five time points: baseline (day 0), and days 2, 7, 9, and 13 post-induction. Below: Quantitative analysis of joint swelling, represented by the mean diameters (in mm) of the left wrist, right wrist, right ankle, and left ankle at the corresponding time points.

3.3 [^{18}F]FDG PET IMAGING

Quantitative [^{18}F]FDG PET analysis demonstrated an elevation in [^{18}F]FDG uptake in terms of SUV localized to the ankle joints, with detectable increases emerging as early as day 7 following disease induction (Figure 26 below). In contrast, SUV in the wrist joints remained stable and did not exhibit statistically significant variation throughout the duration of the study. SUV in the ankle joints exhibited a progressive upward trajectory, with interindividual variability at peak uptake between day 9 and 13.

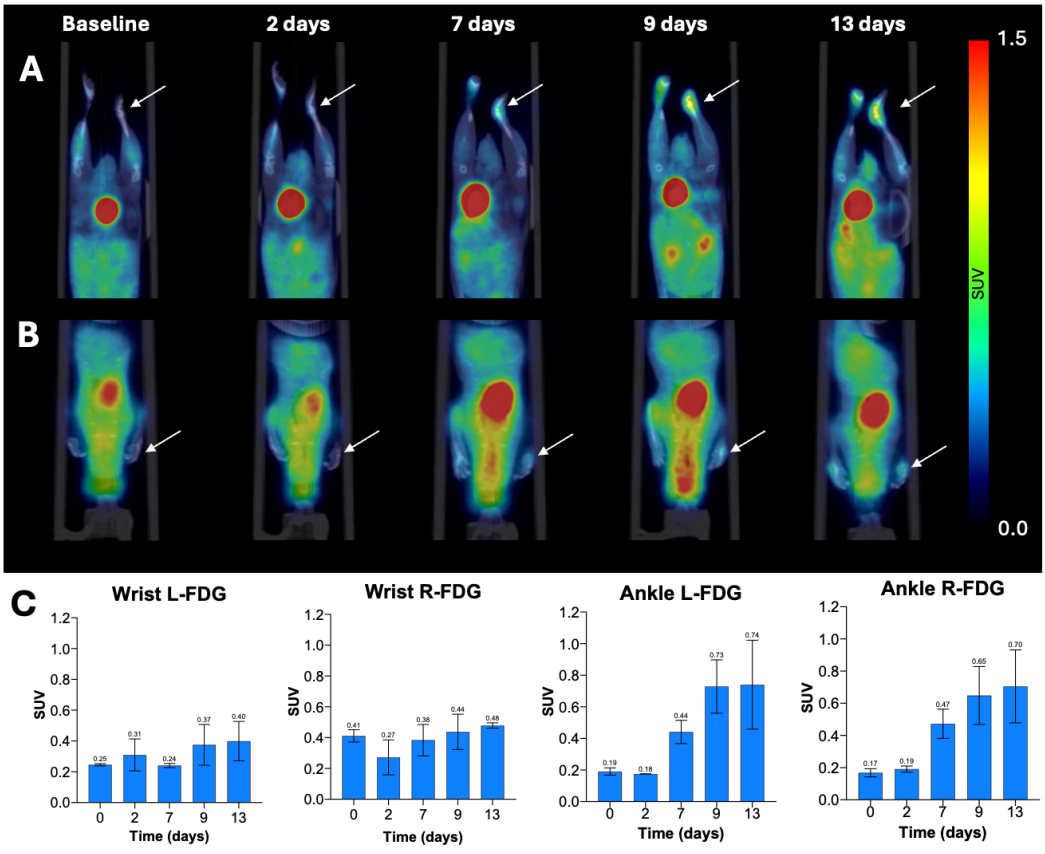

Figure 26: Longitudinal assessment of [^{18}F]FDG SUV joint following arthritis induction. (A): PET images of affected ankles at five time points: baseline (day 0), and days 2, 7, 9, and 13 post-inductions. (B): PET images of affected wrist at five time points: baseline (day 0), and days 2, 7, 9, and 13 post-inductions. (C): Quantitative analysis of joint, represented by the mean uptake (in SUV) of the left wrist, right wrist, right ankle, and left ankle at the corresponding time points.

3.3.1 Relation between [^{18}F]FDG PET and Joint diameter with CT

A linear regression analysis revealed a moderate positive correlation between [^{18}F]FDG PET-derived SUV and joint diameter measured by CT, with an R^2 value of 0.4357 (Figure 27). This indicates that approximately 43.57% of the variance in joint diameter can be attributed to variations in metabolic activity as quantified by the SUV. These findings suggest that increased FDG uptake is moderately associated with greater joint dimensions

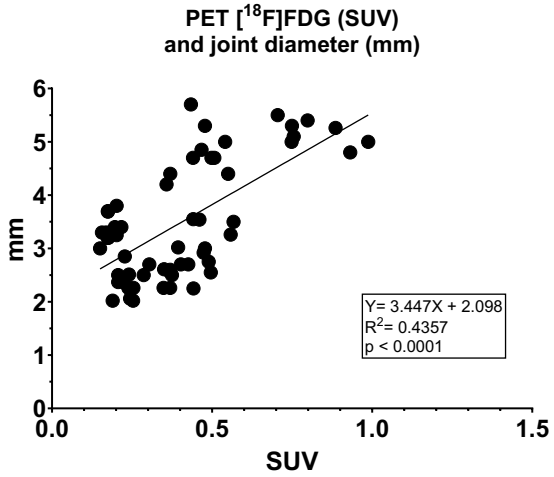

Figure 27: Linear regression between [^{18}F]FDG PET SUV and joint diameter measured by CT.

3.4 [^{89}Zr]Zr-DFO-adalimumab in blood

Following administration of [^{89}Zr]Zr-DFO-adalimumab, blood concentrations, expressed as %ID/mL, were initially higher in the control group compared to the arthritic model. At 3 hours post-injection, control animals showed a tendency of higher [^{89}Zr]Zr-DFO-adalimumab levels (140.26 ± 23.95 %ID/mL) than the arthritic group (117.42 ± 19.46 %ID/mL; p = 0.22). This trend persisted at 6 hours (controls: 120.35 ± 15.13 vs arthritis: 104.05 ± 8.84 %ID/mL; p = 0.13). However, by 12 hours post-injection, blood concentrations converged between groups (controls: 81.05 ± 3.51 vs arthritis: 80.04 ± 6.58 %ID/mL; p = 0.82) and remained comparable until 72 hours (controls: 42.48 ± 0.57 vs arthritis: 41.42 ± 2.76 %ID/mL; p = 0.55). These dynamics don't show differences and are illustrated in *Figure 28*, highlighting the temporal pharmacokinetic profile of the radiotracer in both experimental conditions.

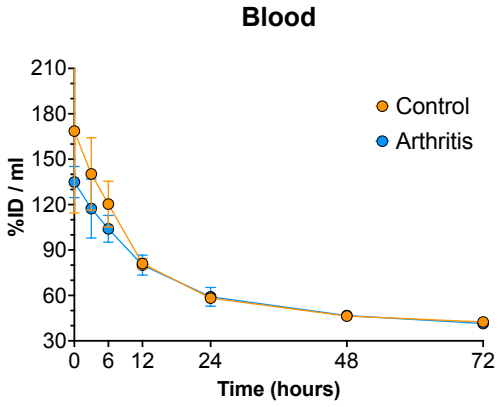

Figure 28: Blood permanence of [^{89}Zr]Zr-DFO-adalimumab (blood versus time). Control group is shown in orange and arthritis group in blue. Values are expressed as means ± SD.

3.5 [^{89}Zr]Zr-anti-adalimumab PET joints distribution

Anti-TNF-α PET imaging was employed to evaluate the biodistribution of [^{89}Zr]Zr-DFO-adalimumab in the joints, showing specifically wrists (Figure 29-A) and ankles (Figure 29-B). From 3 hours onwards, significant differences were found in most limbs between controls and arthritis models ($p < 0.001$). Regarding the quantitative analysis of wrists (Figure 29-B), arthritis models exhibited higher tracer uptake than controls in 5/8 wrists (3/4 left and 2/4 right). Regarding ankles (Figure 30-B), arthritis models exhibited higher tracer uptake than controls in 7/8 ankles (4/4 left and 3/4 right).

Overall, all arthritis models showed higher tracer uptake than controls in, at least, two joints (all joints in 2/4 animals, shown in orange and grey triangles, and two joints in 2/4 animals, shown in pink and green triangles).

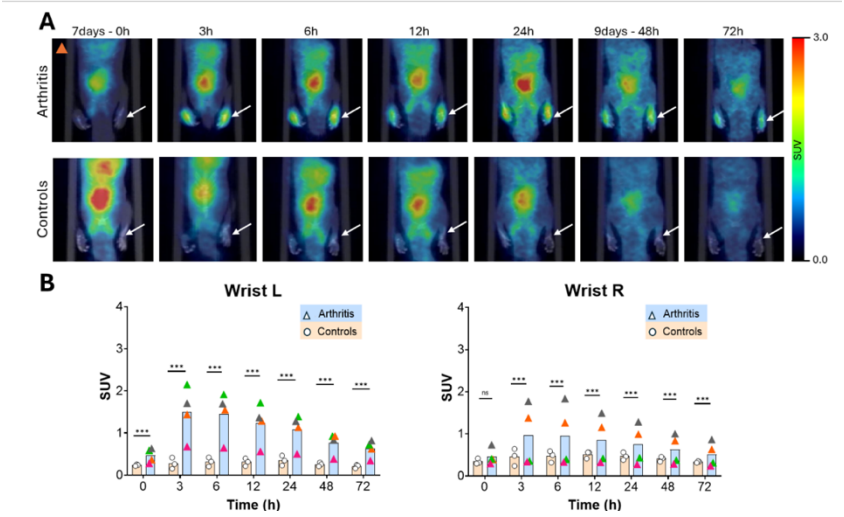

Figure 29: (A) Longitudinal assessment of [^{89}Zr]-ZR-DFO-adalimumab wrists following arthritis induction (signalled by white arrow), from day 7 until 10 days post induction. (B) Quantitative analysis of wrist, represented by the mean uptake (in SUV) of the left wrist (Wrist L) and right wrist (Wrist R) at the corresponding time points.

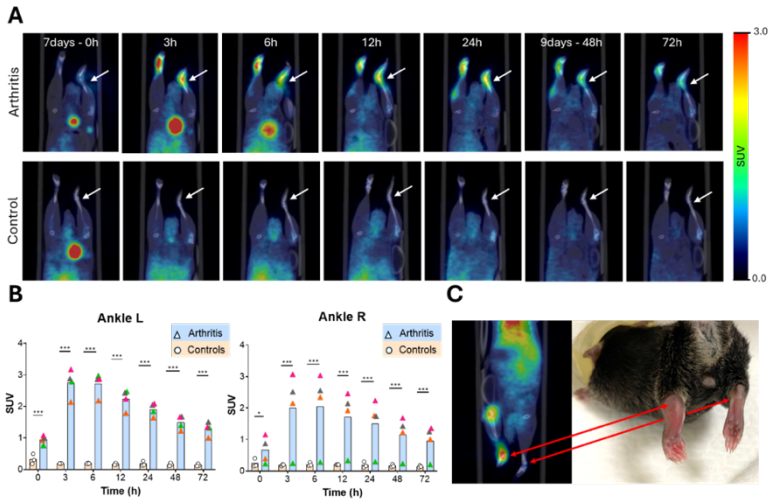

Figure 30: (A) Longitudinal assessment of [^{89}Zr]Zr-DFO-adalimumab ankles following arthritis induction (signalled by white arrow), from day 7 until 10 days post induction. (B) Quantitative analysis of ankles, represented by the mean uptake (in SUV) of the left ankle (Ankle L) and right ankle (Ankle R) at the corresponding time points. (C) Animal exhibiting inflammation in the left limbs (denoted by green triangles in the graphs). On the left is the PET image acquired 3 hours p.i., and on the right is a photograph taken prior to the PET scan, showing the visibly inflamed left ankle and the non-inflamed right ankle.

3.6 EX VIVO ANALYSIS

3.6.1 TNF-*α* in joints

QPCR analysis of TNF-α mRNA expression in wrist L revealed a progressive increase in the arthritic group from day 8 to day 10, in contrast to consistently low levels in healthy controls (Figure 31A). On day 8, TNF-α levels in arthritic mice were slightly elevated compared to controls (1.3 vs. 1.0), with a marked increase observed by day 9 (3.6-fold vs. control 1.0). By day 10, TNF-α expression remained significantly elevated in the arthritis group.

In addition to characterising the natural progression of TNF-α expression in the joints within this model (Figure 31A), we observed that the values obtained from animals injected with [^{89}Zr]Zr-DFO-adalimumab were comparable to those from non-injected animals (injected: 2.15 ± 0.07; non-injected: 2.0; control injected: 1.03 ± 0.30; control non-injected: 1.0), indicating a high degree of model reproducibility. Furthermore, PET analysis results demonstrated a strong correlation with *ex vivo* TNF-α levels in the joints (R^2= 0.88;Figure 31B).

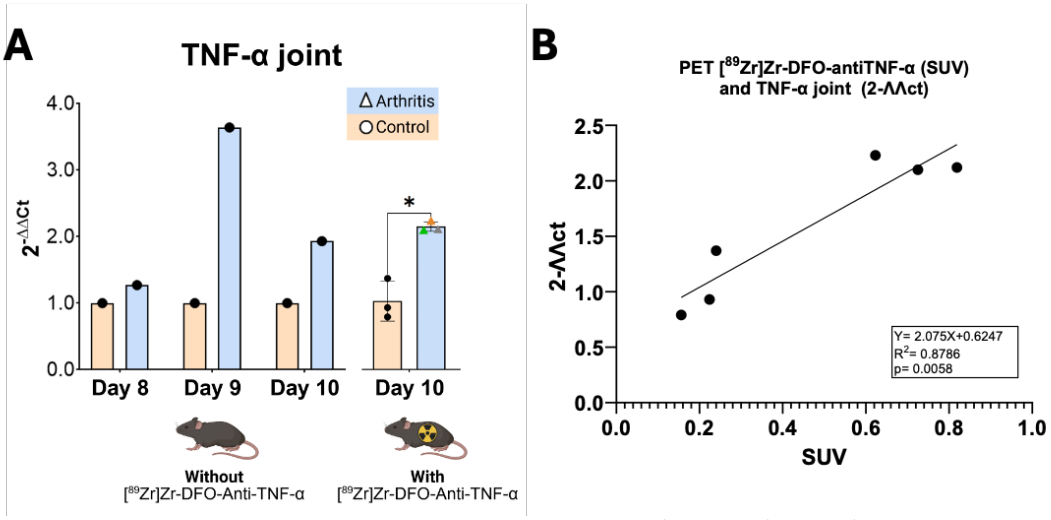

Figure 31:(A) TNF-α mRNA expression in wrist L tissue of arthritic and control mice. Quantification of TNF-α expression in joints was performed by qPCR and plotted as $2^{-\Delta\Delta Ct}$ values. Data are shown for arthritic (blue bars) and control (orange bars) mice from day 8 to day 10 post-induction. On the right, expression levels on day 10 are shown in the separate cohort that received [^{89}Zr]Zr-DFO-Anti-TNF-α 72 h prior to tissue collection. Values are expressed as means ± SD. (B) Correlation between PET signal (SUV) from [^{89}Zr]Zr-DFO-anti-TNF-α and *ex vivo* TNF-α expression in joints at day 10. A strong positive correlation was observed (R^2 = 0.88, p = 0.0058).

3.6.2 TNF-*α* in blood

Serum concentrations of TNF-α expression revealed a significantly increase in the arthritic group compared to consistently low levels in healthy controls from day 8 through day 10 post-induction (**¡Error! No se encuentra el origen de la referencia.**-A). Specifically, TNF-α levels peaked on day 8 in arthritic animals and gradually declined over time, though they remained consistently higher than in controls.

In addition to characterizing the natural progression of TNF-α in serum within this model (**¡Error! No se encuentra el origen de la referencia.**A), we observed that the values obtained from animals injected with [^{89}Zr]Zr-DFO-adalimumab were comparable to those from non-injected animals 10 days post induction (injected: 9.07 ± 1.65; non-injected: 8.50; control

injected: 4.34 ± 0.49; control non-injected: 5.93), indicating a high degree of model reproducibility. Furthermore, PET analysis results demonstrated a strong correlation with *ex vivo* TNF-α levels in the joints (R^2 = 0.83; **¡Error! No se encuentra el origen de la referencia.**B).

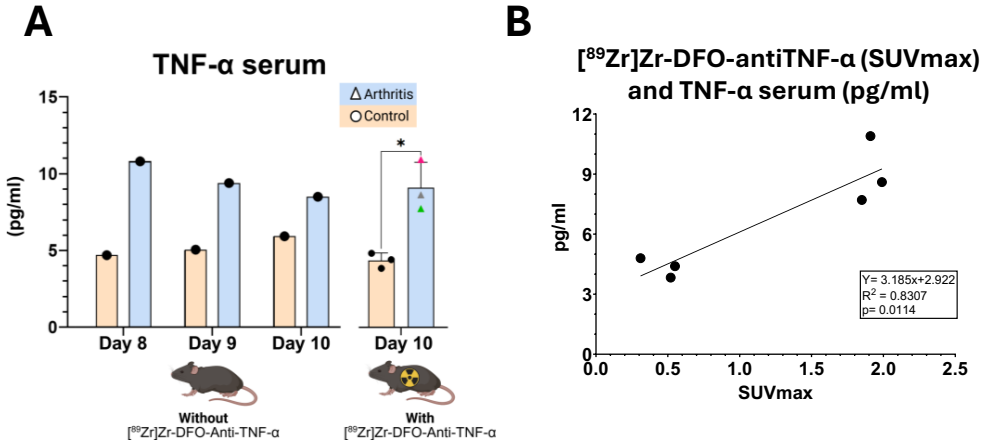

Figure 32: TNF-α levels in serum of arthritic and control mice. Serum TNF-α concentrations were quantified by ELISA at different time points following arthritis induction. Arthritic mice (blue bars) consistently exhibited elevated TNF-α levels compared to control animals (orange bars), particularly evident between days 7 and 10 post-induction. On day 10, a separate cohort received [^{89}Zr]Zr-DFO-Anti-TNF-α 24 hours prior to serum collection. In this group, TNF-α levels remained significantly higher in arthritic animals relative to controls ($p < 0.05$), indicating sustained systemic inflammation. *Values are expressed as means ± SD.* (B) Correlation between [^{89}Zr]Zr-DFO-anti-TNF-α of joints (SUV_{max}) and *ex vivo* TNF-α expression in serum at day 10. A strong positive correlation was observed (R^2 = 0.83, p=0.0114).

3.6.3 Histopathological evaluation

Due to the similarity anatomical interindividual a representative histological images from one animal of each group are shown in

On the left, H&E staining reveals substantial leukocyte infiltration in the arthritic joints (indicated by white arrows), which is absent in the control samples.

On the right, toluidine blue staining highlights proteoglycan content, which appears significantly reduced in the arthritic cartilage. In contrast, control joints exhibit intense blue staining adjacent to the joint cavity, indicating a well-preserved cartilage matrix.

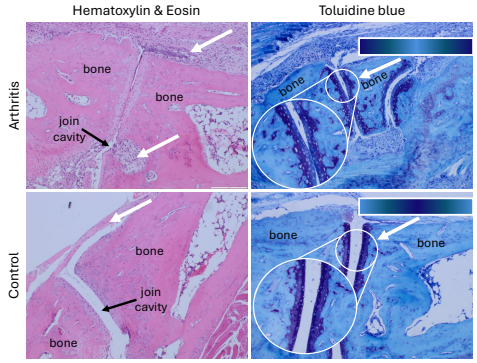

Figure 33: Histological analysis of arthritic and control joints. Upper panel: representative image of an arthritic joint; lower panel: control joint. Left column shows H&E staining, highlighting leukocyte infiltration in the arthritic joint (white arrows), absent in controls. Right column shows toluidine blue staining, where the loss of proteoglycans in arthritic cartilage is evidenced by reduced blue staining. In contrast, control joints show intense blue staining adjacent to the joint cavity, indicating preserved cartilage matrix. Note the marked narrowing of the joint cavity in arthritic samples compared to controls.

4. DISCUSSION

In this study, we investigated the *in vivo* biodistribution of TNF-α over time in both joints and blood of the K/BxN serum transfer model. To achieve this, we employed PET imaging with [^{89}Zr]Zr-DFO-adalimumab, a radiolabelling strategy on protocols previously established by our group.

K/BxN serum transfer model was used a well-established and advantageous model of rheumatoid arthritis (RA) due to its rapid onset and progression of pathological features. Compared with the more commonly used collagen-induced arthritis (CIA) model, the K/BxN model exhibits a significantly faster clinical course. Although both models show similar timelines for TNF-α upregulation, CIA typically requires 21 to 28 days to develop overt arthritic signs such as joint swelling, redness, and deformation. In contrast, the K/BxN model manifests these clinical symptoms within approximately 7 days (99). In our experiments, we monitored disease progression from day 0 to day 13 post induction using PET molecular imaging. Upon injection of serum, autoantibodies target joint structures, particularly the synovial fluid, triggering inflammation. Using this model and our PET-based methodology based on a radiopharmaceutical specifically targeting TNF-α, we introduced a critical aspect in the field of new therapies, the detection of TNF-α, a central cytokine in RA and the primary therapeutic target of anti-TNF agents.

In the first phase of the study, we monitored joint diameter over a 13-day period, focusing on wrists and ankles. Although wrist diameter changes did not reach statistical significance, we observed a peak in swelling at day 9, which aligned with elevated TNF-α levels in the joints. In the ankles, joint diameter began to increase around day 7. This progression mirrored findings from FDG-PET imaging (r^2= 0.44). Based on these results, we initiated the second phase of the study starting on day 7 post-induction.

In this second phase, [^{89}Zr]Zr-DFO-adalimumab was administered at low concentrations (60 µg/mouse) on day 7 post-induction. Early blood activity measurements revealed reduced tracer levels in arthritic mice compared to controls, suggesting effective targeting of inflamed joints. By 12 hours post-injection, tracer distribution became comparable between groups, potentially indicating target saturation. Moreover, circulating levels of adalimumab inversely correlated with serum TNF-α concentrations ($R^2 = 0.96$, $p < 0.01$). In other words, higher serum TNF-α levels were associated with lower levels of free anti-TNF-α, suggesting the formation of TNF–anti-TNF immune complexes. This interaction likely initiates immune-mediated clearance mechanisms, including NK cells activity, endocytosis, and subsequent lysosomal degradation (76,77).

Whole-body distribution analyses revealed specific uptake of the radiotracer in the joints of arthritic mice, particularly in the wrists and ankles. In contrast, control mice displayed consistently low baseline uptake throughout the study. Interestingly, all arthritic animals developed inflamed extremities, though the pattern of joint involvement varied. Some mice exhibited inflammation only in the lower limbs, while others were affected unilaterally, highlighting the heterogeneity of disease progression.

These findings were supported by molecular analyses, which showed elevated TNF-α expression in arthritic animals relative to controls. From day 8 onward, TNF-α levels in the joints remained consistently higher than those of control animals. Moreover, tracer-injected animals exhibited similar TNF-α trends which correlated strongly with local adalimumab concentrations in the joints (R^2= 0.88; $p < 0.01$), further validating our imaging results. This indirectly suggests that the radiotracer binds proportionally to TNF-α levels in inflamed tissues.

Beyond the joints, serum TNF-α concentrations also increased between days 8 and 10 post-induction in arthritic mice, both in longitudinal and tracer-injected groups. This indirectly suggests that the radiotracer binds proportionally to TNF-α levels in inflamed tissues ($p < 0.05$). These serum levels showed a strong correlation with PET results (R^2=0.83), indicating that higher systemic TNF-α concentrations are associated with increased joint SUV values. In addition, histological analysis supported the successful induction of the disease model, further reinforcing the molecular and imaging findings.

Although no previous studies have addressed this specific approach, other PET-based strategies have been applied to this or arthritis models. Thus, PET imaging has been already applied to this model in four previous studies. First, Puuvuori et al (116) used a radiopharmaceutical targeting CD69, an early activation marker of the immune system, enabling the detection of immune activity before clinical symptoms manifest. This approach investigated CD69 activation and it may not trigger TNF release. In their study, radiopharmaceutical was observed in the ankles from day 3 post induction, whereas clinical signs of arthritis did not become apparent until day 7 post induction. Our findings are consistent with theirs, as we did not observe FDG uptake or joint diameter enlargement at day 2 post-induction, whereas both parameters became evident by day 7. Gawne et al. also utilised this model to analyse the biodistribution of liposomal glucocorticoids labelled with Zr-89 (NSSL MPS) within inflamed joints. This approach facilitates the prediction of therapeutic efficacy and optimisation of dosage, although the signal is based on the general therapeutic vector glucocorticoids rather than a specific pro-inflammatory molecule (117). Meanwhile, Guenthoer et al. employed [^{18}F]FMISO PET imaging to evaluate hypoxia within inflamed joint regions in the KB/xN arthritis model, assessing the therapeutic response to p38 MAPK and combined p38/JNK3 inhibition. While clinical improvements are observed, the correlation between FMISO signal and inflammation proves inadequate, highlighting the limitations of non-specific tracers (118). Bezière et al. introduced an innovative strategy involving a GPVI Fc tracer labelled with Cu-64, capable of binding to exposed extracellular matrix components such as collagen and fibrin (119). This method enables the visualisation of active fibrosis and post-inflammatory tissue remodelling in chronic arthritis, providing new avenues for studying persistent inflammatory processes.

5. CONCLUSION

This study establishes PET/CT imaging with [^{89}Zr]Zr-DFO-adalimumab as a valuable tool for visualizing and quantifying TNF-α expression in the K/BxN serum-transfer arthritis model. Our findings support its use as a sensitive and specific modality for assessing joint inflammation *in vivo*, particularly in the context of preclinical research on TNF-driven pathologies. Complementarily, [^{18}F]FDG PET imaging provided additional information on metabolic activity, highlighting its potential role as a supportive biomarker in joint inflammation studies.

We also characterized the spatiotemporal pattern of inflammation in this model, observing a predominant involvement of the posterior paw joints compared to the anterior paws, with TNF-α levels rising by day 7 post-induction and remaining elevated through day 13. These results provide a foundation for future investigations of inflammatory joint diseases and offer valuable guidance for the evaluation of TNF-targeted therapies and other novel therapeutic interventions.

GENERAL DISCUSSION

A novel methodology has been developed to study the pharmacokinetics and biodistribution of adalimumab, based on PET imaging through radiolabelling with Zr-89. A consistent experimental approach was applied across the three disease models, all of which share a common pathogenesis associated with elevated levels of TNF-α. In total, 547 PET images were analysed to assess the distribution of adalimumab in target tissues, 140 PET images in chapter I, 294 in chapter II, and 113 in Chapter III. This strategy enabled a comparative analysis of key parameters, including biodistribution in blood and target tissues, routes of administration, and comparison with [^{18}F]FDG uptake. This unified framework facilitated the identification of shared biodistribution patterns, contributing to a deeper understanding of the underlying mechanisms governing the distribution of adalimumab in different pathological contexts.

Across all three models, radiotracer levels in the blood were consistently lower in diseased animals than in healthy controls. This trend can be partly attributed to the pharmacokinetic properties of adalimumab, which in controls persists longer in circulation due to its high molecular weight and protection from degradation via the neonatal Fc receptor mediated recycling (66, 69). Notably, this reduction in systemic levels was most pronounced in the IBD and uveitis models, both of which are driven by systemic inflammatory stimuli such as DSS and LPS, respectively (90). In RA, although there are more localized inflammatory response due to it is induced by autoantibodies, blood levels of adalimumab were also reduced during the early post-injection phase. These findings suggest that in all models, adalimumab preferentially accumulates in inflamed tissues, thereby limiting its systemic availability and reinforcing its potential for targeted therapy (75,76).

Inflammed tissues showed distinct biodistribution patterns depending on the pathological context. In the IBD model, tracer uptake was rapid, but declined markedly after 48 hours, irrespective of the administration route. In the uveitis model, SC administration failed to deliver adalimumab to the eye, whereas IVT delivery led to prolonged intraocular retention compared to controls. In RA, tracer uptake was both rapid and sustained up to 72 h p.i. These observations underscore the predominant influence of the pathological context on tracer biodistribution, which appears to surpass the effect of the administration route. In healthy controls, tracer uptake in target tissues remained generally stable over time, further highlighting the role of the disease process in shaping the distribution pattern (62).

The role of the administration route was another central theme of this thesis. Adalimumab was administered via SC injection in the IBD and uveitis models, IV in IBD and RA, and IVT in uveitis. Despite differences in the disease model, certain biodistribution characteristics were found to be route-dependent. For instance, prolonged retention at the injection site was observed following SC administration in both IBD and uveitis models (62), while IV administration allowed for rapid systemic distribution (74). These findings align with previous studies suggesting that SC injection typically results in slower absorption and prolonged retention at the injection site due to its more localized nature and the need to pass through the lymphatic system before entering the bloodstream. In contrast, IV administration provides more immediate and widespread distribution to the target tissues.

Confirming the inflammatory models was a critical step in ensuring the rigorous interpretation of the pharmacokinetic and biodistribution results of adalimumab. Several assays were conducted to ensure the relevance of the models employed. Some assays were applied

across all models, such as [^{18}F]FDG PET/CT imaging (97), which provided a measure of the metabolic activity associated with inflammation in tissues. Other assays were model-specific, such as histopathological analysis in IBD and RA. Moreover, confirmation of elevated TNF-α in the target tissues was a consistent requirement: intestinal immunohistochemistry was used for IBD, and qPCR was employed for ocular and joint tissues in uveitis and RA. These methods allowed for validation of the presence of inflammation and ensured that the biodistribution findings were linked to the ongoing pathological processes. Additionally, clinical and functional endpoints adapted to each model, such as joint swelling in RA and weight loss in IBD.

To date, this approach has been scarcely explored in preclinical models of inflammatory diseases. Within the context of IBD, only one prior study was identified that used PET imaging to assess the IV biodistribution of infliximab (66). While that study demonstrated increased colonic radiopharmaceutical accumulation in inflammatory models compared to controls, it did not investigate the temporal evolution of the signal and was limited to a 72 h p.i. analysis. Additionally, a clinical study employing technetium-99m [^{99m}Tc]-labelled infliximab with SPECT imaging faced constraints due to the short half-life of the radionuclide (6 h), which limited the imaging window and hindered detection of delayed radiopharmaceutical accumulation in inflamed tissues (79). In both cases, these temporal limitations precluded a comprehensive characterisation of drug dynamics. In contrast, our study extended the observation period to 7 days p.i., employing adalimumab and a PET-based approach, thereby enabling a more sensitive and prolonged assessment of therapeutic agent distribution.

In the case of uveitis, although SC administration remains the standard route for adalimumab, preliminary reports have explored IVT injection, with promising therapeutic outcomes (90,91). These findings underscore the importance of understanding drug distribution in relation to the anatomical localisation of inflammation, a central premise also addressed in our study. Characterising biodistribution in this model may facilitate the development of more personalised therapeutic strategies aligned with the spatial profile of inflammatory activity.

In RA, the study by Puuvuori et al. represents one of the few relevant references, utilising molecular imaging to detect early immune activation via a radiopharmaceutical targeting CD69 (116). Their findings revealed immune activation as early as day 3 post induction, preceding the onset of clinical symptoms, which appeared by day 7. This temporal pattern is consistent with our observations in the experimental model, where both [^{18}F]FDG uptake and joint inflammation became evident from day 7 onwards. Although CD69 is not directly associated with TNF-α signalling, their results complement our interpretation of the inflammatory progression in this pathology.

Despite the widespread use and characterization of animal models for IBD, uveitis, and RA, it is important to acknowledge that these models do not fully replicate the complexity of human diseases. Physiological, immunological, and pharmacokinetic differences between mice and humans may limit the direct extrapolation of these findings to clinical settings. For instance, immune responses and biodistribution characteristics can differ significantly between species, suggesting that, while these models offer valuable insights into disease mechanisms, caution should be exercised when translating these results to human clinical settings (110).

GENERAL CONCLUSIONS

In this thesis, we have developed a new methodology with [^{89}Zr]Zr-DFO-adalimumab for the imaging of three immune-mediated diseases: IBD, uveitis, and RA. Furthermore, we characterised its biodistribution following different routes of administration, including SC, IV, and IVT delivery. Along all models, complementary biomarkers were obtained, including [^{18}F]FDG PET imaging, histological assessment and various complementary TNF-α assessment methods, such as immunohistochemistry, qPCR, and ELISA. These approaches confirmed successful model induction and enabled the exploration of correlations between [^{89}Zr]Zr-DFO-adalimumab uptake and other relevant biomarkers.

Chapter 1 provided novel insights into how intestinal inflammation and the route of administration influence the pharmacokinetics and tissue distribution of adalimumab therapy in a murine model of colitis. By validating the DSS-induced colitis model and characterising the biodistribution of adalimumab following both SC and IV administration, we demonstrated that inflammatory status significantly alters drug kinetics. Notably, adalimumab exhibited faster systemic clearance yet achieved higher colonic concentrations in inflamed animals compared to healthy controls. Moreover, our results highlight that the route of administration critically determines the timing and magnitude of drug accumulation in target tissues, with IV administration producing earlier and higher peak levels in the colon than SC injection. These findings underscore the importance of considering both disease state and administration route in optimising adalimumab therapy for inflammatory bowel disease.

Chapter 2 explored, for the first time, the ocular biodistribution of radiolabelled adalimumab in a non-infectious uveitis model using PET imaging with [^{89}Zr]Zr-DFO-adalimumab. Our results demonstrated that the route of administration plays a crucial role in determining ocular availability of the antibody. While subcutaneous delivery is less invasive and commonly used in clinical practice, it failed to achieve sufficient intraocular concentrations in the inflamed eye. In contrast, intravitreal injection resulted in markedly higher and more sustained local retention. These findings highlight the limitations of systemic delivery in targeting immune-mediated ocular inflammation and support the use of local delivery strategies in patients with poor systemic treatment response. Moreover, systemic inflammation appeared to compromise ocular drug bioavailability further, possibly by redirecting circulating antibodies toward other inflamed tissues. Altogether, this work supports a more personalised, route-specific approach for the management of uveitis using anti-TNF-α therapies.

Chapter 3 examined the biodistribution and joint-specific accumulation of radiolabelled adalimumab in the K/BxN model of RA, offering new insights into the spatial and temporal dynamics of TNF-α driven inflammation. By monitoring disease progression from baseline to 13 days post-induction, we characterised both systemic and local TNF-α expression patterns in arthritic versus healthy animals. PET imaging revealed that adalimumab accumulates preferentially in inflamed joints, with rapid and sustained uptake observed over time. Importantly, arthritic animals exhibited reduced blood tracer levels in the early post-injection phase, suggesting a redistribution of the antibody to sites of active inflammation. These results reinforce the relevance of local TNF-α expression in guiding therapeutic antibody accumulation and highlight the utility of PET imaging as a non-invasive tool for tracking drug distribution in arthritis.

In conclusion, this thesis provides novel insights into the cross-pathology application of [^{89}Zr]Zr-DFO-adalimumab, highlighting its biodistribution patterns across different inflammatory conditions. The data presented here are scarce in current literature and may offer

valuable contributions to the optimisation of diagnostic and therapeutic strategies in autoimmune diseases.

BIBLIOGRAPHY

1. Veerasubramanian PK, Wynn TA, Quan J, Karlsson FJ. Targeting TNF/TNFR superfamilies in immune-mediated inflammatory diseases. J Exp Med [Internet]. 2024 Nov 4 [cited 2025 Jan 21];221(11). Available from: https://doi.org/10.1084/jem.20240806
2. Cai Z, Wang S, Li J. Treatment of Inflammatory Bowel Disease: A Comprehensive Review. Front Med (Lausanne) [Internet]. 2021 Dec 20 [cited 2025 Jan 27];8:765474. Available from: https://pmc.ncbi.nlm.nih.gov/articles/PMC8720971/
3. Chaparro M, Garre A, Núñez Ortiz A, Diz-Lois Palomares MT, Rodríguez C, Riestra S, et al. Incidence, clinical characteristics and management of inflammatory bowel disease in spain: Large-scale epidemiological study. J Clin Med [Internet]. 2021 Jul 1 [cited 2025 Aug 8];10(13):2885. Available from: https://www.mdpi.com/2077-0383/10/13/2885/htm
4. Coufal S, Kverka M, Kreisinger J, Thon T, Rob F, Kolar M, et al. Serum TGF-β1 and CD14 Predicts Response to Anti-TNF-α Therapy in IBD. Hindawi Journal of Immunology Research [Internet]. 2023 [cited 2023 Aug 8];2023:16. Available from: https://doi.org/10.1155/2023/1535484
5. Billmeier U, Dieterich W, Neurath MF, Atreya R. Molecular mechanism of action of anti-tumor necrosis factor antibodies in inflammatory bowel diseases. Vol. 22, World Journal of Gastroenterology. Baishideng Publishing Group Co; 2016. p. 9300–13.
6. Takeuchi M, Mizuki N, Ohno S, Usui Y, Iwahashi C, University K, et al. Pathogenesis of Non-Infectious Uveitis Elucidated by Recent Genetic Findings. Front Immunol [Internet]. 2021 Apr 12 [cited 2025 Jan 27];12:640473. Available from: https://pmc.ncbi.nlm.nih.gov/articles/PMC8072111/
7. Adán-Civera AM, Benítez-del-Castillo JM, Blanco-Alonso R, Pato-Cour E, Sellas-Fernández A, Bañares-Cañizares A. Carga y costes directos de la uveítis no infecciosa en España. Reumatol Clin [Internet]. 2016 Jul 1 [cited 2025 Aug 8];12(4):196–200. Available from: https://www.reumatologiaclinica.org/es-carga-costes-directos-uveitis-no-articulo-S1699258X15001473
8. Gil-Conesa M, Del-Moral-Luque JA, Gil-Prieto R, Gil-De-Miguel Á, Mazzuccheli-Esteban R, Rodríguez-Caravaca G. Hospitalization burden and comorbidities of patients with rheumatoid arthritis in Spain during the period 2002-2017. BMC Health Serv Res [Internet]. 2020 May 4 [cited 2025 Aug 8];20(1):1–8. Available from: https://bmchealthservres.biomedcentral.com/articles/10.1186/s12913-020-05243-0
9. Han P, Liu X, He J, Han L, Li J. Overview of mechanisms and novel therapies on rheumatoid arthritis from a cellular perspective. Front Immunol [Internet]. 2024 [cited 2025 Jan 27];15:1461756. Available from: https://pmc.ncbi.nlm.nih.gov/articles/PMC11456432/
10. Recommendations EULAR ACR | EULAR [Internet]. [cited 2025 Aug 8]. Available from: https://www.eular.org/recommendations-eular-acr
11. Song Y, Li J, Wu Y. Evolving understanding of autoimmune mechanisms and new therapeutic strategies of autoimmune disorders. Signal Transduct Target Ther [Internet]. 2024 Dec 1 [cited 2025 Jan 21];9(1):263. Available from: https://pmc.ncbi.nlm.nih.gov/articles/PMC11452214/

12. Conrad N, Misra S, Verbakel JY, Verbeke G, Molenberghs G, Taylor PN, et al. Incidence, prevalence, and co-occurrence of autoimmune disorders over time and by age, sex, and socioeconomic status: a population-based cohort study of 22 million individuals in the UK. The Lancet [Internet]. 2023 Jun 3 [cited 2025 Jan 22];401(10391):1878–90. Available from: http://www.thelancet.com/article/S0140673623004579/fulltext

13. Lim H, Lee SH, Lee HT, Lee JU, Son JY, Shin W, et al. Structural Biology of the TNFα Antagonists Used in the Treatment of Rheumatoid Arthritis. Int J Mol Sci [Internet]. 2018 Mar 7 [cited 2025 Jan 21];19(3):768. Available from: https://pmc.ncbi.nlm.nih.gov/articles/PMC5877629/

14. Gordon H, Minozzi S, Kopylov U, Verstockt B, Chaparro M, Buskens C, et al. ECCO Guidelines on Therapeutics in Crohn's Disease: Medical Treatment. J Crohns Colitis [Internet]. 2024 Oct 15 [cited 2025 Aug 8];18(10):1531–55. Available from: https://dx.doi.org/10.1093/ecco-jcc/jjae091

15. Smolen JS, Landewé RBM, Bergstra SA, Kerschbaumer A, Sepriano A, Aletaha D, et al. EULAR recommendations for the management of rheumatoid arthritis with synthetic and biological disease-modifying antirheumatic drugs: 2022 update. Ann Rheum Dis [Internet]. 2022 Nov 10 [cited 2025 Aug 8];82(1):3–18. Available from: https://ard.bmj.com/content/82/1/3

16. Fink DJ, Dell J, Heinz C, Wintergerst MWM, Höller T, Berger M, et al. Treatment exit options for non-infectious uveitis registry: participant characteristics at 3 years. British Journal of Ophthalmology [Internet]. 2025 Jan 1 [cited 2025 Aug 8];109(1):27–33. Available from: https://bjo.bmj.com/content/109/1/27

17. Beltrán Catalán E, Brito García N, Pato Cour E, Muñoz Fernández S, Gómez Gómez A, Díaz Valle D, et al. SER recommendations for the treatment of uveitis. Reumatol Clin [Internet]. 2023 Nov 1 [cited 2025 Aug 8];19(9):465–77. Available from: https://www.reumatologiaclinica.org/en-ser-recommendations-for-treatment-uveitis-articulo-S2173574323001375

18. Molina JF, Molina J, Alejandro GJ, Gonzalez LA. Reumatología, fundamentos de medicina 8va ed. CIB Fondo Editorial. 2018;1–831.

19. Felten R, Mertz P, Sebbag E, Scherlinger M, Arnaud L. Novel therapeutic strategies for autoimmune and inflammatory rheumatic diseases. Drug Discov Today. 2023 Jul 1;28(7):103612.

20. Belmellat N, Semerano L, Segueni N, Damotte D, Decker P, Ryffel B, et al. Tumor necrosis factor-alpha targeting can protect against Arthritis with low sensitization to infection. Volume 8, Issue NOV. 1533 Jan 1;8(NOV).

21. Gerriets V, Goyal A, Khaddour K. Tumor Necrosis Factor Inhibitors. StatPearls [Internet]. 2023 Jul 3 [cited 2025 Jan 26]; Available from: https://www.ncbi.nlm.nih.gov/books/NBK482425/

22. Burmester GR, Gordon KB, Rosenbaum JT, Arikan D, Lau WL, Li P, et al. Long-Term Safety of Adalimumab in 29,967 Adult Patients From Global Clinical Trials Across Multiple Indications: An Updated Analysis. Adv Ther [Internet]. 2019 Jan 1 [cited 2025 Jan 21];37(1):364. Available from: https://pmc.ncbi.nlm.nih.gov/articles/PMC6979455/

23. Hafeez U, Gan HK, Scott AM. Monoclonal antibodies as immunomodulatory therapy against cancer and autoimmune diseases. Curr Opin Pharmacol. 2018 Aug 1;41:114–21.

24. Edner NM, Wang CJ, Petersone L, Walker LSK. Predicting clinical response to costimulation blockade in autoimmunity. Immunotherapy Advances [Internet]. 2021 Jan 1 [cited 2025 Jan 27];1(1):1–6. Available from: https://dx.doi.org/10.1093/immadv/ltaa003

25. Gorman C, Leandro M, Isenberg D. B cell depletion in autoimmune disease. Arthritis Res Ther [Internet]. 2003 Dec 1 [cited 2025 Jan 27];5(SUPPL. 4):1409–20. Available from: http://ard.eular.org/article/S0003496724665349/fulltext

26. Kopylov U, Seidman E. Predicting durable response or resistance to antitumor necrosis factor therapy in inflammatory bowel disease. Therap Adv Gastroenterol [Internet]. 2016 Jul 1 [cited 2023 Aug 7];9(4):513. Available from: /pmc/articles/PMC4913332/

27. Salzer R. Biomedical Imaging : Principles and Applications. 2012.

28. Wang ZJ, Chang TTA, Slauter R. Use of Imaging for Preclinical Evaluation. A Comprehensive Guide to Toxicology in Nonclinical Drug Development. 2017 Jan 1;921–38.

29. Evidence-based Positron Emission Tomography. Evidence-based Positron Emission Tomography. 2020.

30. Adler SS, Seidel J, Choyke PL. Advances in Preclinical PET. Semin Nucl Med [Internet]. 2022 May 1 [cited 2025 May 8];52(3):382. Available from: https://pmc.ncbi.nlm.nih.gov/articles/PMC9038721/

31. Lauber DT, Fülöp A, Kovács T, Szigeti K, Máthé D, Szijártó A. State of the art in vivo imaging techniques for laboratory animals. Lab Anim [Internet]. 2017 Oct 1 [cited 2025 Jan 29];51(5):465–78. Available from: https://journals.sagepub.com/doi/10.1177/0023677217695852?url_ver=Z39.88-2003&rfr_id=ori%3Arid%3Acrossref.org&rfr_dat=cr_pub++0pubmed

32. Saha GB. Basics of PET Imaging: Physics, Chemistry, and Regulations.

33. Nielsen AW, Hansen IT, Nielsen BD, Kjær SG, Blegvad-Nissen J, Rewers K, et al. The effect of prednisolone and a short-term prednisolone discontinuation for the diagnostic accuracy of FDG-PET/CT in polymyalgia rheumatica—a prospective study of 101 patients. Eur J Nucl Med Mol Imaging [Internet]. 2024 Jul 1 [cited 2025 May 8];51(9):2614–24. Available from: https://pubmed.ncbi.nlm.nih.gov/38563881/

34. Kaur S, Shafiq N, Dogra S, Mittal BR, Attri SV, Bahl A, et al. 18F-fluorodeoxyglucose positron emission tomography-based evaluation of systemic and vascular inflammation and assessment of the effect of systemic treatment on inflammation in patients with moderate-to-severe psoriasis: A randomized placebo-controlled pilot study. Indian J Dermatol Venereol Leprol [Internet]. 2018 Nov 1 [cited 2025 May 8];84(6):660–6. Available from: https://pubmed.ncbi.nlm.nih.gov/29893297/

35. Kuwaki K, Mitsuyama K, Kaida H, Takedatsu H, Yoshioka S, Yamasaki H, et al. A longitudinal study of FDG-PET in Crohn disease patients receiving granulocyte/monocyte apheresis therapy. Cytotherapy [Internet]. 2015 Sep 8 [cited 2025 May 8];18(2):291–9. Available from: https://pubmed.ncbi.nlm.nih.gov/26700210/

36. Li Y, Khamou M, Schaarschmidt BM, Umutlu L, Forsting M, Demircioglu A, et al. Comparison of 18F-FDG PET-MR and fecal biomarkers in the assessment of disease activity in patients with ulcerative colitis. British Journal of Radiology [Internet]. 2020

Aug 1 [cited 2025 May 8];93(1112). Available from: https://pubmed.ncbi.nlm.nih.gov/32579403/

37. Domachevsky L, Leibovitzh H, Avni-Biron I, Lichtenstein L, Goldberg N, Nidam M, et al. Correlation of 18F-FDG PET/MRE metrics with inflammatory biomarkers in patients with crohn's disease: A pilot study. Contrast Media Mol Imaging [Internet]. 2017 Jan 1 [cited 2025 May 8];2017. Available from: https://pubmed.ncbi.nlm.nih.gov/29097934/

38. Giles JT, Solomon DH, Liao KP, Rist PM, Fayad ZA, Tawakol A, et al. Association of the multi-biomarker disease activity score with arterial 18-fluorodeoxyglucose uptake in rheumatoid arthritis. Rheumatology [Internet]. 2024 Mar 1 [cited 2025 May 8];64(3). Available from: https://pubmed.ncbi.nlm.nih.gov/38652572/

39. McDougald W, Vanhove C, Lehnert A, Lewellen B, Wright J, Mingarelli M, et al. Standardization of Preclinical PET/CT Imaging to Improve Quantitative Accuracy, Precision, and Reproducibility: A Multicenter Study. Journal of Nuclear Medicine [Internet]. 2020 Mar 1 [cited 2025 May 8];61(3):461–8. Available from: https://pubmed.ncbi.nlm.nih.gov/31562220/

40. Xing Y, Wang S, Du Y, Ma X, Yan H. Application of Positron Emission Tomography in Preclinical Research. 2023 [cited 2025 May 8]; Available from: https://papers.ssrn.com/abstract=4537218

41. Wei W, Rosenkrans ZT, Liu J, Huang G, Luo QY, Cai W. ImmunoPET: Concept, Design, and Applications. Chem Rev [Internet]. 2020 Apr 22 [cited 2025 Feb 2];120(8):3787. Available from: https://pmc.ncbi.nlm.nih.gov/articles/PMC7265988/

42. Lugat A, Bailly C, Chérel M, Rousseau C, Kraeber-Bodéré F, Bodet-Milin C, et al. Immuno-PET: Design options and clinical proof-of-concept. Front Med (Lausanne). 2022 Oct 14;9:1026083.

43. Rong J, Haider A, Jeppesen TE, Josephson L, Liang SH. Radiochemistry for positron emission tomography. Nature Communications 2023 14:1 [Internet]. 2023 Jun 5 [cited 2025 Feb 10];14(1):1–23. Available from: https://www.nature.com/articles/s41467-023-36377-4

44. Lange R, Schreuder N, Hendrikse H. Radiopharmaceuticals. Practical Pharmaceutics: An International Guideline for the Preparation, Care and Use of Medicinal Products, Second Edition [Internet]. 2023 Jun 20 [cited 2025 Feb 10];531–50. Available from: https://www.ncbi.nlm.nih.gov/books/NBK554440/

45. Basu S, Hess S, Nielsen Braad PE. The Basic Principles of FDG-PET/CT Imaging. PET Clinics, 9(4), 355–370 | 10.1016/j.cpet.2014.07.006 [Internet]. 2014 [cited 2025 Feb 11]. 355–370 p. Available from: https://sci-hub.se/10.1016/j.cpet.2014.07.006

46. Glossary: Three Rs principle (in animal experimentation) [Internet]. [cited 2025 Feb 23]. Available from: https://ec.europa.eu/health/opinions/en/non-human-primates/glossary/tuv/three-rs-principle.htm

47. Robinson NB, Krieger K, Khan F, Huffman W, Chang M, Naik A, et al. The current state of animal models in research: A review. International Journal of Surgery. 2019 Dec 1;72:9–13.

48. Verel I, Gerard ;, Visser WM, Boellaard ; Ronald, Marijke ;, Walsum SV, et al. BASIC SCIENCE INVESTIGATIONS 89 Zr Immuno-PET: Comprehensive Procedures for the Production of 89 Zr-Labeled Monoclonal Antibodies. J Nucl Med. 2003;44:1271–81.

49. Pablo Aguiar. Quantification in Positron Emission Tomography: Reconstruction, standarization and processing methods. 2010.

50. Mak WY, Zhao M, Ng SC, Burisch J. The epidemiology of inflammatory bowel disease: East meets west. Vol. 35, Journal of Gastroenterology and Hepatology (Australia). Blackwell Publishing; 2020. p. 380–9.

51. Aardoom MA, Veereman G, de Ridder L. A Review on the Use of Anti-TNF in Children and Adolescents with Inflammatory Bowel Disease. Int J Mol Sci [Internet]. 2019 May 2 [cited 2023 Aug 7];20(10). Available from: /pmc/articles/PMC6566820/

52. Souza RF, Caetano MAF, Magalhães HIR, Castelucci P. Study of tumor necrosis factor receptor in the inflammatory bowel disease. World J Gastroenterol. 2023;29(18):2733–46.

53. Billiet T, Rutgeerts P, Ferrante M, Van Assche G, Vermeire S. Targeting TNF-α for the treatment of inflammatory bowel disease. https://doi.org/101517/147125982014858695 [Internet]. 2013 Jan [cited 2023 Aug 7];14(1):75–101. Available from: https://www.tandfonline.com/doi/abs/10.1517/14712598.2014.858695

54. Villanacci V, Cadei M, Lanzarotto F, Ricci C, Antonelli E, Cannatelli R, et al. Localization of TNF alpha in ileocolonic biopsies of patients with inflammatory bowel disease. Ann Diagn Pathol. 2019 Feb 1;38:20–5.

55. Zhang C, Shu W, Zhou G, Lin J, Chu F, Wu H, et al. Anti-TNF-α therapy suppresses proinflammatory activities of mucosal neutrophils in inflammatory bowel disease. Mediators Inflamm. 2018;2018.

56. Oikonomopoulos A, van Deen W, Hommes D. Anti-TNF antibodies in inflammatory bowel disease: do we finally know how it works? Curr Drug Targets [Internet]. 2013 Dec 27 [cited 2023 Aug 30];14(12):1421–32. Available from: https://pubmed.ncbi.nlm.nih.gov/23627866/

57. Cui G, Fan Q, Li Z, Goll R, Florholmen J. Evaluation of anti-TNF therapeutic response in patients with inflammatory bowel disease: Current and novel biomarkers. EBioMedicine [Internet]. 2021 Apr 1 [cited 2023 Aug 7];66:103329. Available from: /pmc/articles/PMC8054158/

58. Yang HH, Huang Y, Zhou XC, Wang RN. Efficacy and safety of adalimumab in comparison to infliximab for Crohn's disease: A systematic review and meta-analysis. World J Clin Cases. 2022 Jun 26;10(18):6091–104.

59. Sicilia B, García-López S, González-Lama Y, Zabana Y, Hinojosa J, Gomollón F. GETECCU 2020 guidelines for the treatment of ulcerative colitis. Developed using the GRADE approach. Vol. 43, Gastroenterologia y Hepatologia. Ediciones Doyma, S.L.; 2020. p. 1–57.

60. Gisbert JP, Chaparro M. Predictors of Primary Response to Biologic Treatment [Anti-TNF, Vedolizumab, and Ustekinumab] in Patients with Inflammatory Bowel Disease: From Basic Science to Clinical Practice. Vol. 14, Journal of Crohn's and Colitis. Oxford University Press; 2020. p. 694–709.

61. Hinojosa J, Muñoz F, Martínez-Romero GJ. Relationship between Serum Adalimumab Levels and Clinical Outcome in the Treatment of Inflammatory Bowel Disease. Vol. 37, Digestive Diseases. S. Karger AG; 2019. p. 444–50.

62. González García J, Gutiérrez Nicolás F, Ramos Díaz R, Nazco Casariego GJ, Viña Romero MM, Llabres Martinez M, et al. Pharmacokinetics of Trastuzumab After Subcutaneous and Intravenous Administration in Obese Patients. Annals of Pharmacotherapy. 2020 Aug 1;54(8):775–9.

63. Van Dongen GAMS, Beaino W, Windhorst AD, Zwezerijnen GJC, Oprea-Lager DE, Harry Hendrikse N, et al. The role of 89zr-immuno-pet in navigating and derisking the development of biopharmaceuticals. Journal of Nuclear Medicine. 2021;62(4):438–45.

64. García-Otero X, Mondelo-García C, Bandín-Vilar E, Gómez-Lado N, Silva-Rodríguez J, Rey-Bretal D, et al. PET study of intravitreal adalimumab pharmacokinetics in a uveitis rat model. Int J Pharm. 2022 Nov 5;627.

65. Beckford-Vera DR, Gonzalez-Junca A, Janneck JS, Huynh TL, Blecha JE, Seo Y, et al. PET/CT Imaging of Human TNFα Using [89Zr]Certolizumab Pegol in a Transgenic Preclinical Model of Rheumatoid Arthritis. Mol Imaging Biol. 2020 Feb 1;22(1):105–14.

66. Yan G, Wang X, Fan Y, Lin J, Yan J, Wang L, et al. Immuno-PET Imaging of TNF-α in Colitis Using 89Zr-DFO-infliximab. Mol Pharm [Internet]. 2022 Oct 3 [cited 2023 Aug 7];19(10):3632–9. Available from: https://pubs.acs.org/doi/abs/10.1021/acs.molpharmaceut.2c00411

67. Chassaing B, Aitken JD, Malleshappa M, Vijay-Kumar M. Dextran Sulfate Sodium (DSS)-Induced Colitis in Mice. Current protocols in immunology / edited by John E Coligan . [et al] [Internet]. 2014 [cited 2023 Aug 30];104(SUPPL.104):Unit. Available from: /pmc/articles/PMC3980572/

68. Katsandegwaza B, Horsnell W, Smith K. Inflammatory Bowel Disease: A Review of Pre-Clinical Murine Models of Human Disease. Int J Mol Sci [Internet]. 2022 Aug 1 [cited 2023 Aug 7];23(16). Available from: /pmc/articles/PMC9409205/

69. Shargel L, Yu AC. Empirical Models, Mechanistic Models, Statistical Moments, and Noncompartmental Analysis. In: Applied Biopharmaceutics & Pharmacokinetics [Internet]. 7th ed. McGraw-Hill Education; 2016 [cited 2024 Jun 4]. Available from: https://accesspharmacy.mhmedical.com/content.aspx?bookid=1592&sectionid=100668516

70. Marchal-Bressenot A, Salleron J, Boulagnon-Rombi C, Bastien C, Cahn V, Cadiot G, et al. Development and validation of the Nancy histological index for UC. Available from: http://dx.doi.org/10.

71. Luaces-Rodríguez A, del Amo EM, Mondelo-García C, Gómez-Lado N, Gonzalez F, Ruibal Á, et al. PET study of ocular and blood pharmacokinetics of intravitreal bevacizumab and aflibercept in rats. European Journal of Pharmaceutics and Biopharmaceutics. 2020 Sep 1;154:330–7.

72. Díez-Villares S, García-Varela L, Antas SG de, Caeiro JR, Carpintero-Fernandez P, Mayán MD, et al. Quantitative PET tracking of intra-articularly administered 89Zr-peptide-decorated nanoemulsions. Journal of Controlled Release. 2023 Apr 1;356:702–13.

73. García-Varela L, Codesido J, Perez-Pedrosa A, Muñoz-González M, Ramos-Docampo E, Rey-Bretal D, et al. Biodistribution and pharmacokinetics of [89Zr]-anti-VEGF mAbs

using PET in glioblastoma rat models. Int J Pharm [Internet]. 2024 Mar;652:123795. Available from: https://linkinghub.elsevier.com/retrieve/pii/S0378517324000292

74. Schreiber S, Ben-Horin S, Leszczyszyn J, Dudkowiak R, Lahat A, Gawdis-Wojnarska B, et al. Randomized Controlled Trial: Subcutaneous vs Intravenous Infliximab CT-P13 Maintenance in Inflammatory Bowel Disease. Gastroenterology. 2021 Jun 1;160(7):2340–53.

75. Tabrizi MA, Tseng CML, Roskos LK. Elimination mechanisms of therapeutic monoclonal antibodies. Vol. 11, Drug Discovery Today. 2006. p. 81–8.

76. Tom Herschel, Ali El-Armouche, Silvio Weber. Monoclonal antibody. Dtsch Med Wochenschr [Internet]. 2016 [cited 2024 Mar 23];141(19):1390–4. Available from: https://www.thieme-connect.de/products/ejournals/html/10.1055/s-0042-102980#

77. Levin AD, Wildenberg ME, van den Brink GR. Mechanism of Action of Anti-TNF Therapy in Inflammatory Bowel Disease. J Crohns Colitis [Internet]. 2016 Aug 1 [cited 2023 Aug 8];10(8):989–97. Available from: https://dx.doi.org/10.1093/ecco-jcc/jjw053

78. Conner KP, Devanaboyina SC, Thomas VA, Rock DA. The biodistribution of therapeutic proteins: Mechanism, implications for pharmacokinetics, and methods of evaluation. Pharmacol Ther. 2020 Aug 1;212:107574.

79. C D´Álessandria, G Malviya, A Viscido, A Aratari, F Maccioni, A Amato, et al. Use of a 99mTc labeled anti-TNFalpha monoclonal antibody in Crohn's disease: in vitro and in vivo studies. The quarterly journal of Nuclear Medicine and Molecular Imaging. 2007 May 1;51(4):334–42.

80. Waldmann TA, Strober W. Metabolism of Immunoglobulins. In: Chemical Immunology and Allergy. Prog. Allergy, 13; 1969. p. 1–110.

81. Seoane-Viaño I, Gómez-Lado N, Lázare-Iglesias H, Barreiro-de Acosta M, Silva-Rodríguez J, Luzardo-Álvarez A, et al. Longitudinal PET/CT evaluation of TNBS-induced inflammatory bowel disease rat model. Int J Pharm. 2018 Oct 5;549(1–2):335–42.

82. Hoberuck S, Zophel K, Pomper MG, Rowe SP, Gafita A. One Hundred Years of the Tracer Principle. Journal of Nuclear Medicine. 2023;64(12):1998–2000.

83. Fan Y, Wang X, Yan G, Gao H, Yang M. Rectal delivery of 89Zr-labeled infliximab-loaded nanoparticles enables PET imaging-guided localized therapy of inflammatory bowel disease. J Mater Chem B. 2023 Nov 14;11(47):11228–34.

84. Kalogeropoulos D, Kanavaros P, Vartholomatos G, Moussa G, Ch'Ng SW, Kalogeropoulos C. Cytokines in Immune-mediated "Non-infectious" Uveitis. Klin Monbl Augenheilkd [Internet]. 2025 Dec 22 [cited 2025 May 20];242(01):31–46. Available from: http://www.thieme-connect.com/products/ejournals/html/10.1055/a-2202-8704

85. Merrill PT, Vitale A, Zierhut M, Goto H, Kron M, Song AP, et al. Efficacy of Adalimumab in Non-Infectious Uveitis Across Different Etiologies: A Post Hoc Analysis of the VISUAL I and VISUAL II Trials. Ocul Immunol Inflamm [Internet]. 2021 Nov 17 [cited 2025 May 28];29(7–8):1569–75. Available from: https://www.tandfonline.com/doi/pdf/10.1080/09273948.2020.1757123

86. Jiang Q, Li Z, Tao T, Duan R, Wang X, Su W. TNF-α in Uveitis: From Bench to Clinic. Front Pharmacol [Internet]. 2021 Nov 2 [cited 2025 May 20];12:740057. Available from: https://pmc.ncbi.nlm.nih.gov/articles/PMC8592912/

87. Joltikov KA, Lobo-Chan AM. Epidemiology and Risk Factors in Non-infectious Uveitis: A Systematic Review. Front Med (Lausanne) [Internet]. 2021 Sep 10 [cited 2025 May 20];8:695904. Available from: https://pmc.ncbi.nlm.nih.gov/articles/PMC8461013/

88. Noninfectious Uveitis - American Academy of Ophthalmology [Internet]. [cited 2025 May 20]. Available from: https://www.aao.org/eyenet/article/noninfectious-uveitis-3

89. Li H, Yoneda M, Takeyama M, Sugita I, Tsunekawa H, Yamada H, et al. Effect of infliximab on tumor necrosis factor-alpha-induced alterations in retinal microvascular endothelial cells and retinal pigment epithelial cells. Journal of Ocular Pharmacology and Therapeutics [Internet]. 2010 Dec 1 [cited 2025 May 20];26(6):549–56. Available from: /doi/pdf/10.1089/jop.2010.0079?download=true

90. Hamam RN, Barikian AW, Antonios RS, Abdulaal MR, Alameddine RM, El Mollayess G, et al. Intravitreal Adalimumab in Active Noninfectious Uveitis: A Pilot Study. Ocul Immunol Inflamm [Internet]. 2016 May 3 [cited 2025 Jul 14];24(3):319–26. Available from: https://www.tandfonline.com/doi/pdf/10.3109/09273948.2014.990041

91. Hassoun MM, Mahfoud ZR, Istambouli R, Mansour AM, Salti H, Allam S, et al. Intravitreal versus Subcutaneous Adalimumab in Active Non-Infectious Uveitis: A Randomized Non-Inferiority Trial. Ocul Immunol Inflamm. 2025;

92. Girol AP, Mimura KKO, Drewes CC, Bolonheis SM, Solito E, Farsky SHP, et al. Anti-Inflammatory Mechanisms of the Annexin A1 Protein and Its Mimetic Peptide Ac2-26 in Models of Ocular Inflammation In Vivo and In Vitro. The Journal of Immunology [Internet]. 2013 Jun 1 [cited 2025 May 15];190(11):5689–701. Available from: https://dx.doi.org/10.4049/jimmunol.1202030

93. da Silva PS, Giro AP, Oliani SM. Mast cells modulate the inflammatory process in endotoxin-induced uveitis. Mol Vis [Internet]. 2011 [cited 2025 May 15];17:1310. Available from: https://pmc.ncbi.nlm.nih.gov/articles/PMC3103740/

94. García-Otero X, Mondelo-García C, Bandín-Vilar E, Gómez-Lado N, Silva-Rodríguez J, Rey-Bretal D, et al. PET study of intravitreal adalimumab pharmacokinetics in a uveitis rat model. Int J Pharm [Internet]. 2022 Nov 5 [cited 2025 May 15];627:122261. Available from: https://www.sciencedirect.com/science/article/pii/S037851732200816X?via%3Dihub

95. García-Otero X, Mondelo-García C, González F, Perez-Fernandez R, Avila L, Antúnez-López JR, et al. Anti-Inflammatory Effect of Tacrolimus/Hydroxypropyl-β-Cyclodextrin Eye Drops in an Endotoxin-Induced Uveitis Model. Pharmaceutics 2021, Vol 13, Page 1737 [Internet]. 2021 Oct 19 [cited 2025 May 15];13(10):1737. Available from: https://www.mdpi.com/1999-4923/13/10/1737/htm

96. Bermudez MA, Sendon-Lago J, Seoane S, Eiro N, Gonzalez F, Saa J, et al. Anti-inflammatory effect of conditioned medium from human uterine cervical stem cells in uveitis. Exp Eye Res [Internet]. 2016 Aug 1 [cited 2025 May 15];149:84–92. Available from: https://www.sciencedirect.com/science/article/pii/S0014483516301750?via%3Dihub

97. Cuartero-Martínez A, Codesido J, Mateos J, Rodríguez-Fernández CA, González-Barcia M, Fernández-Ferreiro A, et al. Preclinical characterization of endotoxin-induced uveitis models using OCT, PET/CT and proteomics. Int J Pharm [Internet]. 2024 Sep 5 [cited 2025 May 25];662:124516. Available from: https://www.sciencedirect.com/science/article/pii/S0378517324007506?via%3Dihub

98. Reig-López J, García-Otero X, Cuquerella-Gilabert M, Bandín-Vilar E, Otero-Espinar FJ, Fernández-Ferreiro A, et al. A physiologically based pharmacokinetic model to describe [89Zr]Zr-DFO-Adalimumab specific activity after intravitreal administration to rats with endotoxin-induced uveitis. Int J Pharm [Internet]. 2025 Aug 20 [cited 2025 Aug 9];681:125845. Available from: https://www.sciencedirect.com/science/article/pii/S0378517325006829

99. Li H, Yoneda M, Takeyama M, Sugita I, Tsunekawa H, Yamada H, et al. Effect of infliximab on tumor necrosis factor-alpha-induced alterations in retinal microvascular endothelial cells and retinal pigment epithelial cells. Journal of Ocular Pharmacology and Therapeutics [Internet]. 2010 Dec 1 [cited 2025 May 26];26(6):549–56. Available from: https://pubmed.ncbi.nlm.nih.gov/21054185/

100. Aveleira CA, Lin CM, Abcouwer SF, Ambrósio AF, Antonetti DA. TNF-α Signals Through PKCζ/NF-κB to Alter the Tight Junction Complex and Increase Retinal Endothelial Cell Permeability. Diabetes [Internet]. 2010 Nov 1 [cited 2025 May 28];59(11):2872–82. Available from: https://dx.doi.org/10.2337/db09-1606

101. Ramírez K, Quesada-Yamasaki D, Fornaguera-Trías J, Ramírez K, Quesada-Yamasaki D, Fornaguera-Trías J. A Protocol to Perform Systemic Lipopolysacharide (LPS) Challenge in Rats. Odovtos International Journal of Dental Sciences [Internet]. 2019 [cited 2025 May 28];21(1):53–66. Available from: http://www.scielo.sa.cr/scielo.php?script=sci_arttext&pid=S2215-34112019000100053&lng=en&nrm=iso&tlng=en

102. Balevic SJ, Rabinovich CE. Profile of adalimumab and its potential in the treatment of uveitis. Drug Des Devel Ther [Internet]. 2016 Sep 19 [cited 2025 Jul 14];10:2997. Available from: https://pmc.ncbi.nlm.nih.gov/articles/PMC5034916/

103. Rahimi E. Transport and lymphatic uptake of monoclonal antibodies after subcutaneous injection. 2023 Aug 2 [cited 2025 May 28]; Available from: /articles/thesis/Transport_and_lymphatic_uptake_of_monoclonal_antibodies_after_subcutaneous_injection/23786460/1

104. Gravallese EM, Firestein GS. Rheumatoid Arthritis — Common Origins, Divergent Mechanisms. New England Journal of Medicine [Internet]. 2023 Feb 9 [cited 2025 Jun 25];388(6):529–42. Available from: https://www.nejm.org/doi/full/10.1056/NEJMra2103726

105. Aletaha D, Smolen JS. Diagnosis and Management of Rheumatoid Arthritis: A Review. JAMA [Internet]. 2018 Oct 2 [cited 2025 Jul 14];320(13):1360–72. Available from: https://jamanetwork.com/journals/jama/fullarticle/2705192

106. Huang J, Fu X, Chen X, Li Z, Huang Y, Liang C. Promising Therapeutic Targets for Treatment of Rheumatoid Arthritis. Front Immunol [Internet]. 2021 Jul 9 [cited 2025 Jun 25];12:686155. Available from: https://pmc.ncbi.nlm.nih.gov/articles/PMC8299711/

107. Fleischmann R, Pangan AL, Song IH, Mysler E, Bessette L, Peterfy C, et al. Upadacitinib Versus Placebo or Adalimumab in Patients With Rheumatoid Arthritis and an Inadequate Response to Methotrexate: Results of a Phase III, Double-Blind, Randomized Controlled Trial. Arthritis & Rheumatology [Internet]. 2019 Nov 1 [cited 2025 Jun 29];71(11):1788–800. Available from: /doi/pdf/10.1002/art.41032

108. Zhao T, Xie Z, Xi Y, Liu L, Li Z, Qin D. How to Model Rheumatoid Arthritis in Animals: From Rodents to Non-Human Primates. Front Immunol [Internet]. 2022 May 25 [cited 2025 Jul 14];13:887460. Available from: www.frontiersin.org

109. Rosloniec EF, Whittington K, Proslovsky A, Brand DD. Collagen-Induced Arthritis Mouse Model. Curr Protoc [Internet]. 2021 Dec 1 [cited 2025 Jul 14];1(12). Available from: https://pubmed.ncbi.nlm.nih.gov/34890495/

110. Monach PA, Benoist C, Mathis D. The Role of Antibodies in Mouse Models of Rheumatoid Arthritis, and Relevance to Human Disease. Adv Immunol [Internet]. 2004 Jan 1 [cited 2025 Jun 26];82:217–48. Available from: https://www.sciencedirect.com/science/article/abs/pii/S0065277604820054?via%3Dihub

111. Beckford-Vera DR, Gonzalez-Junca A, Janneck JS, Huynh TL, Blecha JE, Seo Y, et al. PET/CT Imaging of Human TNFα Using [89Zr]Certolizumab Pegol in a Transgenic Preclinical Model of Rheumatoid Arthritis. Mol Imaging Biol [Internet]. 2020 Feb 1 [cited 2025 Jul 14];22(1):105–14. Available from: https://link.springer.com/article/10.1007/s11307-019-01363-0

112. Clausen AS, Christensen C, Christensen E, Cold S, Kristensen LK, Hansen AE, et al. Development of a 64Cu-labeled CD4+ T cell targeting PET tracer: evaluation of CD4 specificity and its potential use in collagen-induced arthritis. EJNMMI Res [Internet]. 2022 [cited 2025 Jul 14];12(1). Available from: https://pubmed.ncbi.nlm.nih.gov/36114433/

113. Jamar F, Versari A, Galli F, Lecouvet F, Signore A. Molecular Imaging of Inflammatory Arthritis and Related Disorders. Semin Nucl Med [Internet]. 2018 May 1 [cited 2025 Jul 14];48(3):277–90. Available from: https://www.sciencedirect.com/science/article/pii/S0001299817301186?via%3Dihub#s0020

114. Orosa B, García S, Martínez P, González A, Gómez-Reino JJ, Conde C. Lysophosphatidic acid receptor inhibition as a new multipronged treatment for rheumatoid arthritis. Ann Rheum Dis [Internet]. 2014 Jan [cited 2025 Jun 26];73(1):298–305. Available from: https://pubmed.ncbi.nlm.nih.gov/23486415/

115. Untergasser A, Cutcutache I, Koressaar T, Ye J, Faircloth BC, Remm M, et al. Primer3-new capabilities and interfaces. Nucleic Acids Res [Internet]. 2012 Aug [cited 2025 Jun 26];40(15). Available from: https://pubmed.ncbi.nlm.nih.gov/22730293/

116. Puuvuori E, Shen Y, Hulsart-Billström G, Mitran B, Zhang B, Cheung P, et al. Noninvasive PET Detection of CD69-Positive Immune Cells Before Signs of Clinical Disease in Inflammatory Arthritis. Journal of Nuclear Medicine [Internet]. 2024 Feb 1 [cited 2025 Jun 25];65(2):294–9. Available from: https://jnm.snmjournals.org/content/65/2/294

117. Gawne PJ, Clarke F, Turjeman K, Cope AP, Long NJ, Barenholz Y, et al. PET Imaging of Liposomal Glucocorticoids using 89Zr-oxine: Theranostic Applications in Inflammatory Arthritis. Theranostics [Internet]. 2020 [cited 2025 Jun 25];10(9):3867. Available from: https://pmc.ncbi.nlm.nih.gov/articles/PMC7086351/

118. Guenthoer P, Fuchs K, Reischl G, Quintanilla-Martinez L, Gonzalez-Menendez I, Laufer S, et al. Evaluation of the therapeutic potential of the selective p38 MAPK inhibitor Skepinone-L and the dual p38/JNK 3 inhibitor LN 950 in experimental K/BxN serum transfer arthritis. Inflammopharmacology [Internet]. 2019 Dec 1 [cited 2025 Jun 25];27(6):1217–27. Available from: https://pubmed.ncbi.nlm.nih.gov/31037574/

119. Beziere N, Fuchs K, Maurer A, Reischl G, Brück J, Ghoreschi K, et al. Imaging fibrosis in inflammatory diseases: targeting the exposed extracellular matrix. Theranostics [Internet]. 2019 [cited 2025 Jun 26];9(10):2868–81. Available from: http://www.thno.org

120. Abbas AK, Lichtman AH, Pillai S. Inmunología básica. Funciones y trastornos del sistema inmunitario. 4º. Elsevier; 2014.

APPENDIX

CONFLICT OF INTEREST

The PhD candidate declares that there is no conflict of interest in relation to the Doctoral Thesis.

FUNDING AND SUPPORT

The PhD candidate was supported during the completion of this doctoral thesis by a competitive predoctoral contract awarded by the Health Research Institute of Santiago de Compostela.

PERMISSION TO REPRODUCE PAPERS

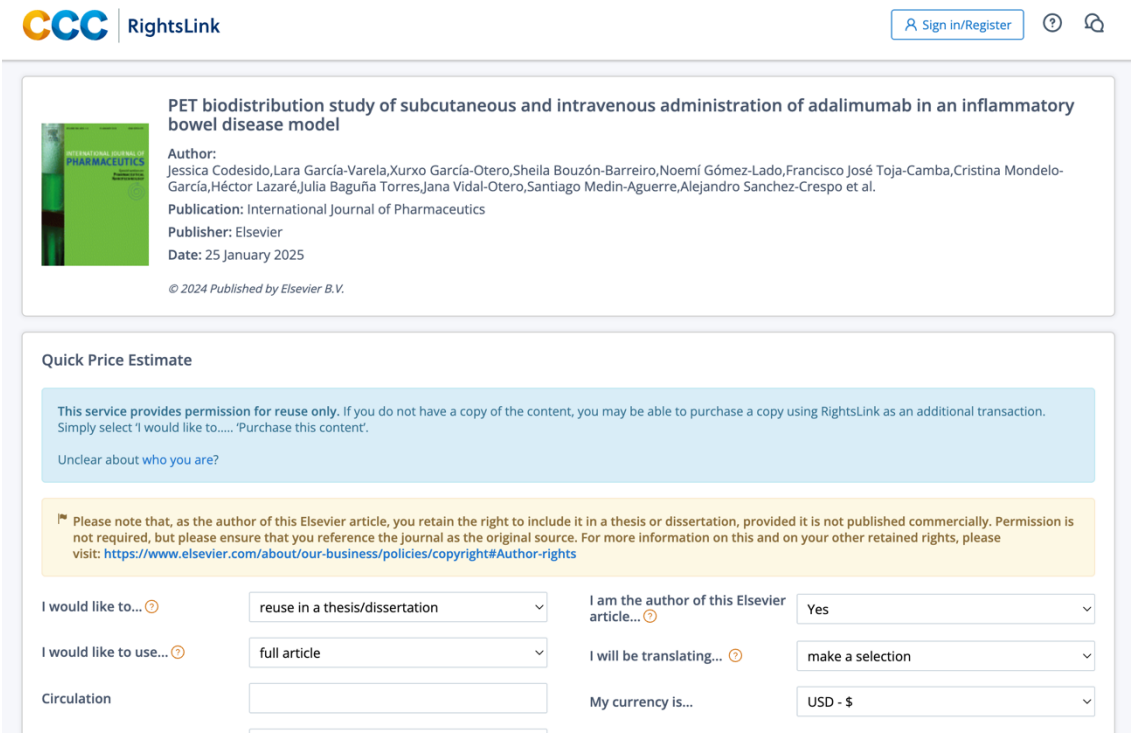

CCC RightsLink

Sign in/Register

PET biodistribution study of subcutaneous and intravenous administration of adalimumab in an inflammatory bowel disease model

Author:
Jessica Codesido,Lara García-Varela,Xurxo García-Otero,Sheila Bouzón-Barreiro,Noemí Gómez-Lado,Francisco José Toja-Camba,Cristina Mondelo-García,Héctor Lazaré,Julia Baguña Torres,Jana Vidal-Otero,Santiago Medin-Aguerre,Alejandro Sanchez-Crespo et al.

Publication: International Journal of Pharmaceutics

Publisher: Elsevier

Date: 25 January 2025

© 2024 Published by Elsevier B.V.

Quick Price Estimate

This service provides permission for reuse only. If you do not have a copy of the content, you may be able to purchase a copy using RightsLink as an additional transaction. Simply select 'I would like to..... 'Purchase this content'.

Unclear about who you are?

Please note that, as the author of this Elsevier article, you retain the right to include it in a thesis or dissertation, provided it is not published commercially. Permission is not required, but please ensure that you reference the journal as the original source. For more information on this and on your other retained rights, please visit: https://www.elsevier.com/about/our-business/policies/copyright#Author-rights

I would like to... reuse in a thesis/dissertation

I am the author of this Elsevier article... Yes

I would like to use... full article

I will be translating... make a selection

Circulation

My currency is... USD - $

LIST OF FIGURES

	and *ex vivo* TNF-α expression in serum at day 10. A strong positive correlation was observed ($R^2 = 0.83$, p=0.0114).	
Figure 33	Histological analysis of arthritic and control joints. Upper panel: representative image of an arthritic joint; lower panel: control joint. Left column shows H&E staining, highlighting leukocyte infiltration in the arthritic joint (white arrows), absent in controls. Right column shows toluidine blue staining, where the loss of proteoglycans in arthritic cartilage is evidenced by reduced blue staining. In contrast, control joints show intense blue staining adjacent to the joint cavity, indicating preserved cartilage matrix. Note the marked narrowing of the joint cavity in arthritic samples compared to controls.	81

LIST OF TABLES

EXPERIMENTAL ANIMALS ARRIVE

Yes/No/NA		page
	Title	
Yes	Provide as accurate and concise a description of the content of the article as possible.	41, 57, 70
	Abstract	
Yes	Provide an accurate summary of the background, research objectives, including details of the species or strain of animal used, key methods, principal findings and conclusions of the study.	42, 58, 71
	Background	
Yes	Provide an accurate summary of the background, research objectives, including details of the species or strain of animal used, key methods, principal findings and conclusions of the study.	44, 60, 73
Yes	Explain how and why the animal species and model being used can address the scientific objectives and, where appropriate, the study's relevance to human biology.	45, 61, 74
	Objectives	
Yes	Clearly describe the primary and any secondary objectives of the study, or specific hypotheses being tested.	33-34
	Methods	
	Ethical statement	
Yes	Indicate the nature of the ethical review permissions, relevant licenses, and national or institutional guidelines for the care and use of animals, that cover the research.	45, 60, 73
	Study design	
Yes	Number of experimental and control groups	45, 60, 73
Yes	Steps taken to minimize the effects of subjective bias when allocating animals to treatment (e.g. randomization procedure) and when assessing results (e.g. if done, describe who was blinded and when).	48, 60, 73
Yes	The experimental unit (e.g. a single animal, group or cage of animals). A time-line diagram or flow chart can be useful to illustrate how complex study designs were carried out.	48, 60, 73
	Experimental procedures	
Yes	How (e.g. drug formulation and dose, site and route of administration, anesthesia and analgesia used [including monitoring], surgical procedure, method of euthanasia). Provide details of any specialist equipment used, including supplier(s).	46, 60, 74
Yes	When (e.g. time of day).	46, 60, 74
Yes	Where (e.g. home cage, laboratory, water maze).	46, 60, 73
Yes	Why (e.g. rationale for choice of specific anesthetic, route of administration, drug dose used).	46, 60, 73
	Experimental animals	
Yes	Provide details of the animals used, including species, strain, sex, developmental stage (e.g. mean or median age plus age range) and weight (e.g. mean or median weight plus weight range).	45, 60, 73
Yes	Provide further relevant information such as the source of animals, international strain nomenclature, genetic modification status (e.g. knock-out or transgenic), genotype, health/immune status, drug or test naïve, previous procedures, etc.	45, 60, 73

	Housing and husbandry	
Yes	Housing (type of facility e.g. specific pathogen free [SPF]; type of cage or housing; bedding material; number of cage companions; tank shape and material etc. for fish).	45, 60, 73
Yes	Husbandry conditions (e.g. breeding program, light/dark cycle, temperature, quality of water etc for fish, type of food, access to food and water, environmental enrichment).	45, 60, 73
NA	Welfare-related assessments and interventions that were carried out prior to, during, or after the experiment.	
	Sample size	
Yes	Specify the total number of animals used in each experiment, and the number of animals in each experimental group.	45, 60, 73
NA	Explain how the number of animals was arrived at. Provide details of any sample size calculation used.	
NA	Indicate the number of independent replications of each experiment, if relevant.	
	Allocating animals to experimental groups	
NA	Indicate the number of independent replications of each experiment, if relevant.	
NA	Describe the order in which the animals in the different experimental groups were treated and assessed.	
	Experimental outcomes	
Yes	Clearly define the primary and secondary experimental outcomes assessed (e.g. cell death, molecular markers, behavioral changes).	45-47, 62-67, 73-76
	Statistical methods	
Yes	Provide details of the statistical methods used for each analysis.	44, 46, 61, 73
Yes	Specify the unit of analysis for each dataset (e.g. single animal, group of animals, single neuron).	45, 46, 62, 73
NA	Describe any methods used to assess whether the data met the assumptions of the statistical approach.	
	Results and discussion	
	Basal data	
Yes	For each experimental group, report relevant characteristics and health status of animals (e.g. weight, microbiological status, and drug or test naïve) prior to treatment or testing (this information can often be tabulated).	48
	Numbers analyzed	
Yes	Report the number of animals in each group included in each analysis. Report absolute numbers (e.g. 10/20, not 50%).	45, 62, 73
Yes	If any animals or data were not included in the analysis, explain why.	48
	Outcomes and estimation	
Yes	Report the results for each analysis carried out, with a measure of precision (e.g. standard error or confidence interval).	47-54, 64-69, 76-82
	Adverse events	
NO	Give details of all important adverse events in each experimental group.	
NA	Describe any modifications to the experimental protocols made to reduce adverse events.	
	Interpretation/scientific implications	

Yes	Interpret the results, taking into account the study objectives and hypotheses, current theory and other relevant studies in the literature.	54-57, 68-71, 82-84
Yes	Comment on the study limitations including any potential sources of bias, any limitations of the animal model, and the imprecision associated with the results.	54-57, 68-71, 82-84
NA	Describe any implications of your experimental methods or findings for the replacement, refinement or reduction (the 3Rs) of the use of animals in research.	
	Generalizability/translation	
Yes	Comment on whether, and how, the findings of this study are likely to translate to other species or systems, including any relevance to human biology.	54-57, 68-71, 82-84
	Funding	
NA	List all funding sources (including grant number) and the role of the funder(s) in the study.	

Based on The ARRIVE guidelines: Animal Research: Reporting of In Vivo Experiments.

PhD Student signature

TRAINING CERTIFICATES

AXENCIA GALEGA DA CALIDADE ALIMENTARIA

Avda. Do Camiño Francés, 10, Baixo
15703 Santiago de Compostela
A Coruña

Xacobeo 21·22

MÓDULOS FUNDAMENTAIS OU TRONCAIS E ESPECÍFICOS CORRESPONDENTES Á FUNCIÓN "a" COIDADO DOS ANIMAIS – ORDE ECC/566/2015, DE 20 DE MARZO

MÓDULOS FUNDAMENTAIS OU TRONCAIS

1.- Lexislación nacional (1 hora).

2.- Ética, benestar animal e as "tres erres", nivel 1 (2 horas).

3.- Bioloxía básica e adecuada, nivel 1 (3 horas).

4.- Coidado, saúde e manexo dos animais, nivel 1 (5 horas).

5.- Recoñecemento da dor, o sufrimento e a angustia (3 horas).

6.- Métodos incruentos de sacrificio, nivel 1 (2 horas)

MÓDULOS ESPECÍFICOS DA FUNCIÓN "a"

1.-Bioloxía básica e adecuada, nivel 2 (3 horas)

.....

MÓDULOS FUNDAMENTALES O TRONCALES Y ESPECÍFICOS CORRESPONDIENTES A LA FUNCIÓN "a" CUIDADO DE LOS ANIMALES – ORDEN ECC/566/2015, DE 20 DE MARZO

MÓDULOS FUNDAMENTALES O TRONCALES

1.- Legislación nacional (1 hora).

2.- Ética, bienestar animal y las "tres erres", nivel 1 (2 horas).

3.- Biología básica y adecuada, nivel 1 (3 horas).

4.- Cuidado, salud y manejo de los animales, nivel 1 (5 horas).

5.- Reconocimiento del dolor, el sufrimiento y la angustia (3 horas).

6.- Métodos incruentos de sacrificio, nivel 1 (2 horas)

MÓDULOS ESPECÍFICOS DE LA FUNCIÓN "a"

1.-Biología básica y adecuada, nivel 2 (3 horas)

AXENCIA GALEGA DA CALIDADE ALIMENTARIA

Avda. Do Camiño Francés, 10, Baixo
15703 Santiago de Compostela
A Coruña

Xacobeo 21·22

Certificado de capacitación en materia de protección de animais utilizados, criados ou subministrados con fins de experimentación e outros fins científicos, incluíndo a docencia conforme coa Orde ECC/566/2015 de 20 de marzo.

Certificado de capacitación en materia de protección de animales utilizados, criados o suministrados con fines de experimentación y otros fines científicos, incluyendo la docencia conforme con la Orden ECC/566/2015 de 20 de marzo.

1. IDENTIFICACIÓN / *IDENTIFICACIÓN*		
1.1. Apelidos / *Apellidos* **Fraga Codesido**		
1.2. Nome / *Nombre* **Jessica**		DNI / *DNI* **45906227K**
1.3. Función / *Función* **"a"**	1.4. Grupo ou grupos de especies* / *Grupo o grupos de especies** **1**	1.5. Data inicial de vixencia** / *Fecha inicial de vigencia*** **02/09/2022**

2. Nº DO CERTIFICADO / *Nº DEL CERTIFICADO*
a362

3.ORGANISMO QUE EXPIDE O CERTIFICADO / *ORGANISMO QUE EXPIDE EL CERTIFICADO*		
3.1. Nome e enderezo do organismo que expide o certificado / *Nombre y dirección del organismo que expide el certificado* **AXENCIA GALEGA DA CALIDADE ALIMENTARIA** **CONSELLERÍA DO MEDIO RURAL – XUNTA DE GALICIA** Rúa do Camiño Francés, 10 baixo 15781 Santiago de Compostela A Coruña (España)		
3.2.Teléfono / *Teléfono* 981 546 657	3.3. Fax / *Fax* 981 546 651	3.4. Correo electrónico / *Correo electrónico* formacion.cmrm@xunta.es
3.5. Data / *Fecha* **Ver sinatura / *Ver firma***	3.6. Lugar / *Lugar* **Santiago de Compostela**	
3.7. Nome e sinatura / *Nombre y firma* **Santiago de Compostela,** **O director da Axencia Galega da Calidade Alimentaria** **Por delegación de sinatura (Resolución do 15/02/2022)** **O xefe da Área de Formación, Innovación e Investigación Agraria** **Manuel López Luaces**		

* Anexo II da Orde ECC/566/2015, do 20 de marzo: 1 (roedores), 2 (lagomorfos), 3 (carnívoros), 4 (équidos, ruminantes e porcino), 5 (primates), 6 (aves), 7 (réptiles), 8 (peixes e anfibios), 9 (cefalópodos), 10 (animais silvestres), 11 (outras especies).
* Anexo II de la Orden ECC/566/2015, de 20 de marzo: 1 (roedores), 2 (lagomorfos), 3 (carnívoros), 4 (équidos, rumiantes y porcino), 5 (primates), 6 (aves), 7 (reptiles), 8 (peces y anfibios), 9 (cefalópodos), 10 (animales silvestres), 11 (otras especies).
** A validez deste certificado será de oito anos contados a partir da data inicial de vixencia. O mantemento da capacitación deberá solicitarse durante os oito meses anteriores á finalización do prazo de vixencia, preferiblemente entre os oito e os tres meses anteriores á finalización do mesmo. /
** *La validez de este certificado será de ocho años contados a partir de la fecha inicial de vigencia. El mantenimiento de la capacitación deberá solicitarse durante los ocho meses anteriores a la finalización del plazo de vigencia, preferiblemente entre los ocho y los tres meses anteriores a la finalización del mismo.*

AXENCIA GALEGA DA CALIDADE ALIMENTARIA

Avda. Do Camiño Francés, 10, Baixo
15703 Santiago de Compostela
A Coruña

Xacobeo 21·22

MÓDULOS FUNDAMENTAIS OU TRONCAIS E ESPECÍFICOS CORRESPONDENTES Á FUNCIÓN "b" EUTANASIA DOS ANIMAIS – ORDE ECC/566/2015, DE 20 DE MARZO

MÓDULOS FUNDAMENTAIS OU TRONCAIS

1.- Lexislación nacional (1 hora).

2.- Ética, benestar animal e as "tres erres", nivel 1 (2 horas).

3.- Bioloxía básica e adecuada, nivel 1 (3 horas).

4.- Coidado, saúde e manexo dos animais, nivel 1 (5 horas).

5.- Recoñecemento da dor, o sufrimento e a angustia (3 horas).

6.- Métodos incruentos de sacrificio, nivel 1 (2 horas)

MÓDULOS ESPECÍFICOS DA FUNCIÓN "b"

1.- Bioloxía básica e adecuada, nivel 2 (3 horas)

2.- Métodos incruentos de sacrificio, nivel 2 (3 horas)

.....

MÓDULOS FUNDAMENTALES O TRONCALES Y ESPECÍFICOS CORRESPONDIENTES A LA FUNCIÓN "b" EUTANASIA DE LOS ANIMALES – ORDEN ECC/566/2015, DE 20 DE MARZO

MÓDULOS FUNDAMENTALES O TRONCALES

1.- Legislación nacional (1 hora).

2.- Ética, bienestar animal y las "tres erres", nivel 1 (2 horas).

3.- Biología básica y adecuada, nivel 1 (3 horas).

4.- Cuidado, salud y manejo de los animales, nivel 1 (5 horas).

5.- Reconocimiento del dolor, el sufrimiento y la angustia (3 horas).

6.- Métodos incruentos de sacrificio, nivel 1 (2 horas)

MÓDULOS ESPECÍFICOS DE LA FUNCIÓN "b"

1.- Biología básica y adecuada, nivel 2 (3 horas)

2.- Métodos incruentos de sacrificio, nivel 2 (3 horas)

AXENCIA GALEGA DA CALIDADE ALIMENTARIA

Avda. Do Camiño Francés, 10, Baixo
15703 Santiago de Compostela
A Coruña

Xacobeo 21·22

Certificado de capacitación en materia de protección de animais utilizados, criados ou subministrados con fins de experimentación e outros fins científicos, incluíndo a docencia conforme coa Orde ECC/566/2015 de 20 de marzo.

Certificado de capacitación en materia de protección de animales utilizados, criados o suministrados con fines de experimentación y otros fines científicos, incluyendo la docencia conforme con la Orden ECC/566/2015 de 20 de marzo.

1. IDENTIFICACIÓN / *IDENTIFICACIÓN*		
1.1. Apelidos / *Apellidos* **Fraga Codesido**		
1.2. Nome / *Nombre* **Jessica**		DNI / *DNI* **45906227K**
1.3. Función / *Función* **"b"**	1.4. Grupo ou grupos de especies* / *Grupo o grupos de especies** **1**	1.5. Data inicial de vixencia** / *Fecha inicial de vigencia*** **02/09/2022**

2. Nº DO CERTIFICADO / *Nº DEL CERTIFICADO*
b664

3.ORGANISMO QUE EXPIDE O CERTIFICADO / *ORGANISMO QUE EXPIDE EL CERTIFICADO*		
3.1. Nome e enderezo do organismo que expide o certificado / *Nombre y dirección del organismo que expide el certificado* **AXENCIA GALEGA DA CALIDADE ALIMENTARIA** **CONSELLERÍA DO MEDIO RURAL – XUNTA DE GALICIA** Rúa do Camiño Francés, 10 baixo 15781 Santiago de Compostela A Coruña (España)		
3.2.Teléfono / *Teléfono* 981 546 657	3.3. Fax / *Fax* 981 546 651	3.4. Correo electrónico / *Correo electrónico* formacion.cmrm@xunta.es
3.5. Data / *Fecha* **Ver sinatura / *Ver firma***	3.6. Lugar / *Lugar* **Santiago de Compostela**	
3.7. Nome e sinatura / *Nombre y firma* **Santiago de Compostela,** **O director da Axencia Galega da Calidade Alimentaria** **Por delegación de sinatura (Resolución do 15/02/2022)** **O xefe da Área de Formación, Innovación e Investigación Agraria** **Manuel López Luaces**		

* Anexo II da Orde ECC/566/2015, do 20 de marzo: 1 (roedores), 2 (lagomorfos), 3 (carnívoros), 4 (équidos, ruminantes e porcino), 5 (primates), 6 (aves), 7 (réptiles), 8 (peixes e anfibios), 9 (cefalópodos), 10 (animais silvestres), 11 (outras especies).
* Anexo II de la Orden ECC/566/2015, de 20 de marzo: 1 (roedores), 2 (lagomorfos), 3 (carnívoros), 4 (équidos, rumiantes y porcino), 5 (primates), 6 (aves), 7 (reptiles), 8 (peces y anfibios), 9 (cefalópodos), 10 (animales silvestres), 11 (otras especies).
** A validez deste certificado será de oito anos contados a partir da data inicial de vixencia. O mantemento da capacitación deberá solicitarse durante os oito meses anteriores á finalización do prazo de vixencia, preferiblemente entre os oito e os tres meses anteriores á finalización do mesmo. /
** *La validez de este certificado será de ocho años contados a partir de la fecha inicial de vigencia. El mantenimiento de la capacitación deberá solicitarse durante los ocho meses anteriores a la finalización del plazo de vigencia, preferiblemente entre los ocho y los tres meses anteriores a la finalización del mismo.*

AXENCIA GALEGA DA CALIDADE ALIMENTARIA

Avda. Do Camiño Francés, 10, Baixo
15703 Santiago de Compostela
A Coruña

MÓDULOS FUNDAMENTAIS OU TRONCAIS E ESPECÍFICOS CORRESPONDENTES Á FUNCIÓN "c" REALIZACIÓN DOS PROCEDEMENTOS – ORDE ECC/566/2015, DE 20 DE MARZO

MÓDULOS FUNDAMENTAIS OU TRONCAIS

1.- Lexislación nacional (1 hora).

2.- Ética, benestar animal e as "tres erres", nivel 1 (2 horas).

3.- Bioloxía básica e adecuada, nivel 1 (3 horas).

4.- Coidado, saúde e manexo dos animais, nivel 1 (5 horas).

5.- Recoñecemento da dor, o sufrimento e a angustia (3 horas).

6.- Métodos incruentos de sacrificio, nivel 1 (2 horas)

MÓDULOS ESPECÍFICOS DA FUNCIÓN "c"

1.- Bioloxía básica e adecuada, nivel 2 (3 horas)

2.- Procedementos minimamente invasores sen anestesia, nivel 1 (5 horas)

3.- Procedementos minimamente invasores sen anestesia, nivel 2 (10 horas)

4.- Anestesia para procedementos menores (5 horas)

5.- Anestesia avanzada para intervencións cirúrxicas ou procedementos prolongados (8 horas)

6.- Principios de cirurxía (5 horas)

.....

MÓDULOS FUNDAMENTALES O TRONCALES Y ESPECÍFICOS CORRESPONDIENTES A LA FUNCIÓN "c" REALIZACIÓN DE LOS PROCEDIMIENTOS – ORDEN ECC/566/2015, DE 20 DE MARZO

MÓDULOS FUNDAMENTALES O TRONCALES

1.- Legislación nacional (1 hora).

2.- Ética, bienestar animal y las "tres erres", nivel 1 (2 horas).

3.- Biología básica y adecuada, nivel 1 (3 horas).

4.- Cuidado, salud y manejo de los animales, nivel 1 (5 horas).

5.- Reconocimiento del dolor, el sufrimiento y la angustia (3 horas).

6.- Métodos incruentos de sacrificio, nivel 1 (2 horas)

MÓDULOS ESPECÍFICOS DE LA FUNCIÓN "c"

1.- Biología básica y adecuada, nivel 2 (3 horas)

2.- Procedimientos mínimamente invasivos sin anestesia, nivel 1 (5 horas)

3.- Procedimientos mínimamente invasivos sin anestesia, nivel 2 (10 horas)

4.- Anestesia para procedimientos menores (5 horas)

5.- Anestesia avanzada para intervenciones quirúrgicas o procedimientos prolongados (8 horas)

6.- Principios de cirugía (5 horas)

AXENCIA GALEGA DA CALIDADE ALIMENTARIA

Avda. Do Camiño Francés, 10, Baixo
15703 Santiago de Compostela
A Coruña

Xacobeo 21·22

Certificado de capacitación en materia de protección de animais utilizados, criados ou subministrados con fins de experimentación e outros fins científicos, incluíndo a docencia conforme coa Orde ECC/566/2015 de 20 de marzo.

Certificado de capacitación en materia de protección de animales utilizados, criados o suministrados con fines de experimentación y otros fines científicos, incluyendo la docencia conforme con la Orden ECC/566/2015 de 20 de marzo.

1. IDENTIFICACIÓN / *IDENTIFICACIÓN*

1.1. Apelidos / *Apellidos*

Fraga Codesido

1.2. Nome / *Nombre*	DNI / *DNI*
Jessica	**45906227K**

1.3. Función / *Función*	1.4. Grupo ou grupos de especies* / *Grupo o grupos de especies**	1.5. Data inicial de vixencia** / *Fecha inicial de vigencia***
"c"	**1**	**02/09/2022**

2. Nº DO CERTIFICADO / *Nº DEL CERTIFICADO*

c708

3.ORGANISMO QUE EXPIDE O CERTIFICADO / *ORGANISMO QUE EXPIDE EL CERTIFICADO*

3.1. Nome e enderezo do organismo que expide o certificado / *Nombre y dirección del organismo que expide el certificado*

AXENCIA GALEGA DA CALIDADE ALIMENTARIA
CONSELLERÍA DO MEDIO RURAL – XUNTA DE GALICIA
Rúa do Camiño Francés, 10 baixo
15781 Santiago de Compostela
A Coruña (España)

3.2. Teléfono / *Teléfono*	3.3. Fax / *Fax*	3.4. Correo electrónico / *Correo electrónico*
981 546 657	981 546 651	formacion.cmrm@xunta.es

3.5. Data / *Fecha*	3.6. Lugar / *Lugar*
Ver sinatura / *ver firma*	**Santiago de Compostela**

3.7. Nome e sinatura / *Nombre y firma*

Santiago de Compostela,

O director da Axencia Galega da Calidade Alimentaria

Por delegación de sinatura (Resolución do 15/02/2022)
O xefe da Área de Formación, Innovación e Investigación Agraria

Manuel López Luaces

* Anexo II da Orde ECC/566/2015, do 20 de marzo: 1 (roedores), 2 (lagomorfos), 3 (carnívoros), 4 (équidos, ruminantes e porcino), 5 (primates), 6 (aves), 7 (réptiles), 8 (peixes e anfibios), 9 (cefalópodos), 10 (animais silvestres), 11 (outras especies).
* Anexo II de la Orden ECC/566/2015, de 20 de marzo: 1 (roedores), 2 (lagomorfos), 3 (carnívoros), 4 (équidos, rumiantes y porcino), 5 (primates), 6 (aves), 7 (reptiles), 8 (peces y anfibios), 9 (cefalópodos), 10 (animales silvestres), 11 (otras especies).
** A validez deste certificado será de oito anos contados a partir da data inicial de vixencia. O mantemento da capacitación deberá solicitarse durante os oito meses anteriores á finalización do prazo de vixencia, preferiblemente entre os oito e os tres meses anteriores á finalización do mesmo. /
*** La validez de este certificado será de ocho años contados a partir de la fecha inicial de vigencia. El mantenimiento de la capacitación deberá solicitarse durante los ocho meses anteriores a la finalización del plazo de vigencia, preferiblemente entre los ocho y los tres meses anteriores a la finalización del mismo.*

Dña. Alejandra Martínez Maquieira

CERTIFICA

QUE DÑA. JESSICA FRAGA CODESIDO
DNI: 45906227K
Titulación Académica: Graduada en Óptica y Optometría

Ha realizado el **CURSO DE FORMACIÓN PARA SUPERVISORES DE INSTALACIONES RADIACTIVAS**.

Campo de aplicación: **MEDICINA NUCLEAR**

Impartido en Santiago de Compostela del 22 de marzo al 01 de abril de 2022 y homologado por acuerdo del Consejo de Seguridad Nuclear con fecha 30 de octubre de 2003, en virtud de lo establecido en el artículo 2.g. de la Ley 15/1980 de 22 de abril y en atención a la delegación conferida mediante acuerdo del Pleno del CSN de fecha 18 de marzo de 1998.

Habiendo superado el correspondiente examen de formación propuesto por el Consejo de Seguridad Nuclear con fecha 01 de abril de 2022.

Lo que hace constar para los efectos oportunos en

Santiago de Compostela,

Alejandra Martínez Maquieira

Firmado digitalmente por Alejandra Martínez Maquieira
Nombre de reconocimiento (DN): cn=Alejandra Martínez Maquieira, o=Universidade de Santiago de Compostela, ou=Servizo de Protección Radiolóxica, email=alejandra.martinez@usc.es, c=ES
Fecha: 2022.04.11 10:55:56 +02'00'

La Directora del Curso

AUTHORIZATION NUMBER OF THE ANIMAL EXPERIMENTATION PROJECTS

XUNTA DE GALICIA
CONSELLERÍA DO MEDIO RURAL

Xefatura Territorial
Sº de Gandaría
Edificio administrativo Monelos, 4º andar
Rúa Vicente Ferrer, Nº 2
15008 A Coruña
Tfno.: 981 184 565
Correo electrónico: servizo.gandaria.a.coruna@xunta.gal

galicia

RESOLUCIÓN DE AUTORIZACIÓN DE PROXECTO DE EXPERIMENTACIÓN ANIMAL

Expediente núm.: 15012/2021/001
Persoa solicitante: Anxo Vidal Figueroa
Forma de inicio: solicitude da persoa interesada

Data de inicio do expediente: 28.2.2021
Procedemento: resolución de autorización

ANTECEDENTES

A persoa solicitante presentou con data 28.2.2021 unha solicitude para a realización do proxecto de experimentación animal (entrada no Rexistro Electrónico da Xunta de Galicia 2021/430700), cuxos datos se detallan a continuación:

Denominación do proxecto: *Estudo da farmacocinética intravítrea de anticorpos marcados con circonio-89 mediante inxección intravítrea en ratas*

Nome do centro usuario: Centro de Biomedicina Experimental (CEBEGA) da Universidade de Santiago de Compostela
Persoa responsable do proxecto: Anxo Fernández Ferreiro

Establecemento onde se realizarán os procedementos do proxecto (ou lugar xeográfico no caso de traballos de campo): Centro de Biomedicina Experimental (CEBEGA)

Clasificación do proxecto : Tipo I ☐ Tipo II ☒ Tipo III ☐

CONSIDERACIÓNS LEGAIS E TÉCNICAS

1 O Real decreto 53/2013, de 1 de febreiro (BOE 34, do 8 de febreiro), polo que se establecen as normas básicas aplicables para a protección dos animais utilizados en experimentación e outros fins científicos, incluíndo a docencia, establece no seu artigo 33 as condicións de autorizacións dos proxectos con animais de experimentación.

2 O artigo 88 da Lei 39/2015, de 1 de outubro, do procedemento administrativo común das administracións públicas (BOE 236, do 2 de outubro de 2015) establece que a resolución que poña fin o procedemento decidirá todas as cuestións expostas polos interesados e aquelas outras derivadas deste.

XUNTA DE GALICIA
CONSELLERÍA DO MEDIO RURAL

Xefatura Territorial
Sº de Gandaría
Edificio administrativo Monelos, 4º andar
Rúa Vicente Ferrer, Nº 2
15008 A Coruña
Tfno.: 981 184 565
Correo electrónico: servizo.gandaria.a.coruna@xunta.gal

galicia

3 O Servizo de Gandaría da Coruña revisou a documentación achegada na solicitude e o resultado favorable da avaliación do proxecto realizada polo órgano habilitado, a Sección de Experimentación Animal do Comité de Bioética da Universidade de Santiago de Compostela.

Esta xefatura territorial é competente para ditar unha resolución, de conformidade co Decreto 149/2018, do 5 de decembro, polo que se establece a estrutura orgánica da Consellería do Medio Rural e se modifica parcialmente o Decreto 177/2016, do 15 de decembro, polo que se fixa a estrutura orgánica da Vicepresidencia e das consellerías da Xunta de Galicia (DOG 235, do 11 de novembro).

De acordo con todo o indicado, RESOLVO:

1 Autorizar o proxecto solicitado.

2 O proxecto non precisa someterse a unha avaliación retrospectiva.

3 A autorización deste proxecto terá unha duración de tres anos e unha vez transcorrido este tempo deberá ser renovada.

A citada autorización é unicamente válida nas condicións que figuran no expediente. Ante calquera cambio significativo no proxecto que poida ter efectos negativos sobre o benestar dos animais, deberá solicitar a confirmación da autorización ao Servizo Provincial de Gandaría.

Esta autorización poderá ser suspendida no caso de que o proxecto non se leve a cabo de acordo coas condicións de autorización e retirala, previo expediente tramitado ao que se lle dará audiencia.

Contra a presente resolución, que non pon fin á vía administrativa, poderá interpoñer un recurso de alzada ante o conselleiro de Medio Rural. O prazo comezará a contar dende o día seguinte ao da recepción desta resolución. Todo isto, segundo o disposto nos artigos 121 e 122 da citada Lei 39/2015.

Mediante este escrito notifícaselle a Anxo Vidal Figueroa esta resolución segundo o esixido no artigo 40.1 da antedita Lei 39/2015.

Xacobeo 2021

XUNTA DE GALICIA | CONSELLERÍA DO MEDIO RURAL

Xacobeo 21·22

RESOLUCIÓN DE AUTORIZACIÓN DE PROXECTO DE EXPERIMENTACIÓN ANIMAL

Expediente núm.: 15012/2022/011
Data de inicio do expediente: 29.3.2022
Persoa solicitante: Anxo Vidal Figueroa
Procedemento: resolución de autorización
Forma de inicio: solicitude da persoa interesada

ANTECEDENTES

A persoa solicitante, como representante do Centro de Biomedicina Experimental CEBEGA, presentou con data 29.3.2022 unha solicitude para a realización do proxecto de experimentación animal (entrada no Rexistro electrónico da Xunta de Galicia 2022/854934), cuxos datos se detallan a continuación:

Denominación do proxecto: Estudos de imaxe molecular e estrutural en rata *(Rattus norvegicus)* e rato *(Mus musculus)* con administración de diferentes contrastes
Nome do centro usuario: Centro de Biomedicina Experimental CEBEGA
Persoa responsable do proxecto: Pablo Aguiar Fernández
Establecemento onde se realizarán os procedementos do proxecto (ou lugar xeográfico no caso de traballos de campo): Centro de Biomedicina Experimental da USC (CEBEGA)

Clasificación do proxecto: Tipo I [ ] Tipo II [X] Tipo III [ ]

CONSIDERACIÓNS LEGAIS E TÉCNICAS

1 O Real decreto 53/2013, de 1 de febreiro (BOE 34, do 8 de febreiro), polo que se establecen as normas básicas aplicables para a protección dos animais utilizados en experimentación e outros fins científicos, incluíndo a docencia, establece no seu artigo 33 as condicións de autorizacións dos proxectos con animais de experimentación.

2 O artigo 88 da Lei 39/2015, de 1 de outubro, do procedemento administrativo común das administracións públicas (BOE 236, do 2 de outubro de 2015) establece que a resolución que poña fin o procedemento decidirá todas as cuestións expostas

CONSELLERÍA DO MEDIO RURAL
XEFATURA TERRITORIAL
SERVIZO DE GANDARÍA
Edificio Administrativo Monelos
R/ Vicente Ferrer, 2, 4º andar
15071 A Coruña
T: 981 184 565
servizo.gandaria.a.coruna@xunta.gal
mediorural.xunta.gal

polos interesados e aquelas outras derivadas deste.

3 O Servizo de Gandaría da Coruña revisou a documentación achegada na solicitude e o resultado favorable da avaliación do proxecto realizada polo órgano habilitado, o Comité de Ética de Experimentación Animal da Universidade de Santiago de Compostela.

Esta xefatura territorial é competente para ditar unha resolución, de conformidade co Decreto 149/2018, do 5 de decembro, polo que se establece a estrutura orgánica da Consellería do Medio Rural e se modifica parcialmente o Decreto 177/2016, do 15 de decembro, polo que se fixa a estrutura orgánica da Vicepresidencia e das consellerías da Xunta de Galicia (DOG 235, do 11 de novembro).

De acordo con todo o indicado, RESOLVO:

1 Autorizar o proxecto solicitado.

2 O proxecto non precisa someterse a unha avaliación retrospectiva.

3 A autorización deste proxecto terá unha duración de cinco anos e unha vez transcorrido este tempo, esta autorización deberá ser renovada.

A citada autorización é unicamente válida nas condicións que figuran no expediente. Ante calquera cambio significativo no proxecto que poida ter efectos negativos sobre o benestar dos animais, deberá solicitar a confirmación da autorización ao Servizo Provincial de Gandaría.

Esta autorización poderá ser suspendida no caso de que o proxecto non se leve a cabo de acordo coas condicións de autorización e retirala, previo expediente tramitado ao que se lle dará audiencia.

Contra a presente resolución, que non pon fin á vía administrativa, poderá interpoñer un recurso de alzada ante o conselleiro de Medio Rural. O prazo comezará a contar dende o día seguinte ao da recepción desta resolución. Todo isto, segundo o disposto nos artigos 121 e 122 da citada Lei 39/2015.

Mediante este escrito notifícaselle a Anxo Vidal Figueroa esta resolución segundo o esixido no artigo 40.1 da antedita Lei 39/2015.

A Coruña, 1 de abril de 2022
O xefe territorial
Jose Manuel Santos Maneiro

XUNTA DE GALICIA | CONSELLERÍA DO MEDIO RURAL

Xacobeo 21·22

RESOLUCIÓN DE AUTORIZACIÓN DE PROXECTO DE EXPERIMENTACIÓN ANIMAL

Expediente núm.: 15012/2022/013
Data de inicio do expediente: 9.9.2022
Persoa solicitante: Anxo Vidal Figueroa
Procedemento: resolución de autorización
Forma de inicio: solicitude da persoa interesada

ANTECEDENTES

A persoa solicitante, como representante do Centro de Biomedicina Experimental CEBEGA, presentou con data 9.9.2022 unha solicitude para a realización do proxecto de experimentación animal (entrada no Rexistro Electrónico da Xunta de Galicia 2022/2235350), cuxos datos se detallan a continuación:

Denominación do proxecto: Estudo de indución e tratamento da colite
Nome do centro usuario: Centro de Biomedicina Experimental CEBEGA
Persoa responsable do proxecto: Pablo Aguiar Fernández
Establecemento onde se realizarán os procedementos do proxecto (ou lugar xeográfico no caso de traballos de campo): Centro de Biomedicina Experimental da USC (CEBEGA) (ES1507800292901)

Clasificación do proxecto: Tipo I [ ] Tipo II [X] Tipo III [ ]

CONSIDERACIÓNS LEGAIS E TÉCNICAS

1 O Real decreto 53/2013, de 1 de febreiro (BOE 34, do 8 de febreiro), polo que se establecen as normas básicas aplicables para a protección dos animais utilizados en experimentación e outros fins científicos, incluíndo a docencia, establece no seu artigo 33 as condicións de autorizacións dos proxectos con animais de experimentación.

2 O artigo 88 da Lei 39/2015, de 1 de outubro, do procedemento administrativo común das administracións públicas (BOE 236, do 2 de outubro de 2015) establece que a resolución que poña fin o procedemento decidirá todas as cuestións expostas polos interesados e aquelas outras derivadas deste.

CONSELLERÍA DO MEDIO RURAL
XEFATURA TERRITORIAL
SERVIZO DE GANDARÍA
Edificio Administrativo Monelos
R/ Vicente Ferrer, 2, 4º andar
15071 A Coruña
T: 981 184 565
servizo.gandaria.a.coruna@xunta.gal
mediorural.xunta.gal

3 O Servizo de Gandaría da Coruña revisou a documentación achegada na solicitude e o resultado favorable da avaliación do proxecto realizada polo órgano habilitado, o Comité de Bioética de Experimentación Animal da Universidade de Santiago de Compostela.

Esta xefatura territorial é competente para ditar unha resolución, de conformidade co Decreto 149/2018, do 5 de decembro, polo que se establece a estrutura orgánica da Consellería do Medio Rural e se modifica parcialmente o Decreto 177/2016, do 15 de decembro, polo que se fixa a estrutura orgánica da Vicepresidencia e das consellerías da Xunta de Galicia (DOG 235, do 11 de novembro).

De acordo con todo o indicado, RESOLVO:

1 Autorizar o proxecto solicitado.

2 O proxecto non precisa someterse a unha avaliación retrospectiva.

3 A autorización deste proxecto terá unha duración de cinco anos e unha vez transcorrido este tempo, esta autorización deberá ser renovada.

A citada autorización é unicamente válida nas condicións que figuran no expediente. Ante calquera cambio significativo no proxecto que poida ter efectos negativos sobre o benestar dos animais, deberá solicitar a confirmación da autorización ao Servizo Provincial de Gandaría.

Esta autorización poderá ser suspendida no caso de que o proxecto non se leve a cabo de acordo coas condicións de autorización e retirala, previo expediente tramitado ao que se lle dará audiencia.

Contra a presente resolución, que non pon fin á vía administrativa, poderá interpoñer un recurso de alzada ante o conselleiro de Medio Rural. O prazo comezará a contar dende o día seguinte ao da recepción desta resolución. Todo isto, segundo o disposto nos artigos 121 e 122 da citada Lei 39/2015.

Mediante este escrito notifícaselle a Anxo Vidal Figueroa esta resolución segundo o esixido no artigo 40.1 da antedita Lei 39/2015.

A Coruña, 20 de setembro de 2022
O xefe territorial
Jose Manuel Santos Maneiro

Immune-mediated inflammatory diseases are chronic disorders involving abnormal activation of the immune system, leading to persistent inflammation and tissue damage. They share mechanisms such as overexpression of pro-inflammatory cytokines. Anti-TNF-a agents like adalimumab are effective, but up to 40% of patients do not respond. This thesis developed a PET-based methodology using [89Zr]Zr-DFOadalimumab to analyze biodistribution and pharmacokinetics in murine models of inflammatory bowel disease, uveitis, and rheumatoid arthritis, administered intravenously, subcutaneously, and intravitreally. This work opens new possibilities for both diagnosis and individualized therapeutic monitoring in inflammatory diseases (theragnosis).